UNIVERSITÀ DEGLI STUDI DI PADOVA

DIPARTIMENTO DI INGEGNERIA INDUSTRIALE
CORSO DI LAUREA MAGISTRALE IN INGEGNERIA CHIMICA E DEI PROCESSI INDUSTRIALI

Tesi di Laurea Magistrale in
Ingegneria Chimica e dei Processi Industriali

Mechanistic analysis of the dynamic strength of wet granular materials

Relatore: Prof. Andrea Claudio Santomaso
Correlatore: Prof. Chuan-Yu Wu

Laureando: Marco De Stefani

ANNO ACCADEMICO 2018 – 2019

Abstract

The dynamic strength of a wet granular material is one of the most important parameters for determining the behaviour of the granules during an agglomeration process. Its value depends on the properties of the powder and of the binder, such as the particle size and the liquid viscosity. In this study four different powders were characterised through the particle size and shape evaluation, and mixed with two silicone oils with different viscosities. A standardised mixing procedure was designed and experimentally validated in order to obtain highly homogeneous wet granular materials. A large number of pellets were prepared and tested by compressing them uniaxially and diametrically with the Advanced Uniaxial Powder Tester and the Instron machine, respectively, measuring the peak stress that the samples can sustain before failing. A new parameter, the consolidation stress applied to the samples, was introduced as a new factor in the determination of the peak stress distribution. The results were elaborated graphically, registering the dependency of the peak stress on the particle size and shape, the binder viscosity, the deformation speed and the consolidation stresses chosen. It has been possible to design a model for the uniaxial compression tests, able to predict the value of the peak stress as a function of two dimensionless numbers: the capillary number, which is a function of particle size, binder viscosity and deformation speed, and the dimensionless consolidation stress, which is a function of consolidation stress and particle size. The model proved to be effective at predicting the dynamic strength, but could also be used to predict the flow function of the wet granular material with high precision. It was not possible to derive a model for the diametrical compression, but the failure behaviour was captured at different conditions and compared with two other parameters, the fracture energy and the dimensionless toughness. Eventually, a DEM simulation was designed to represent the uniaxial compression methodology. The samples were simulated with two reduction scales, and the results proved to be encouraging for a further numerical investigation.

To my family and Monica,
For the constant help and support.

Index

Introduction

Wet granulation is a common industrial process for the production of granular materials, and is widely used in the food and pharmaceutical industries, as well as in other chemical processes. It is typically used agglomerate fine particles into larger granules, up to a size that depends on their subsequent applications. The granules are formed by adding a liquid binder to a powder bed in motion, in which the liquid drops get distributed forming the cores of the future wet granules. The choice of the binder is crucial in the determination of the future granule properties, while health and safety considerations have to be taken into account, too. The granules potential to coalesce and consolidate depends on their capability of withstand the impacts with other granules, which is a function of the dynamic strength of the wet granular material.

This parameter is particularly difficult to measure with on-field tests on the granulation process, and the existing methods are complex and expensive. Therefore, during the last 20 years it has drawn the attention of the scientific community, looking for possible models able to predict the value of the dynamic strength on the basis of the powders and binders' properties. The experimental investigation focused on the testing of pellets of wet granular materials, being deformed in conditions similar to the ones commonly used during agglomeration processes. Parameters such as particle size, binder viscosity and deformation velocity have been considered, providing several models able to predict, in specific operative conditions, the value of the dynamic strength of the materials. Nonetheless, more parameters could have relevant effects on the wet granular properties, while the interactions between the materials' strength and its flowability have not been investigated yet. Furthermore, the powerful tools of the numerical simulations, such as the Discrete Element Method, are nowadays able to simulate the behaviour of thousands of independent particles, extending the available knowledge on the complexity of the wet granular materials behaviour.

On these considerations, this project was designed to further extend the understanding of the wet granular materials by interfacing an in-depth experimental investigation with a comprehensive numerical simulation. Specific focus will be put on the samples' preparation and testing procedures, aiming at providing new standardised and efficient methodologies that improve the quality of the results. The two main testing methodologies used in previous studies, uniaxial and diametrical compression testing, will be enhanced by implementing the use of the Advanced Uniaxial Powder Tester and the Instron machines, to overcome the inaccuracies of the old testing methods. As all the previous studies focused on the same common, regular powders, new materials will be tested with the aim of extending the available literature on the topic and provide new elements of comparison with future studies. The effect of powder consolidation, never considered in previous studies, will been introduced and fully investigated, with specific focus the interaction between its effect on the material flowability and on the dynamic strength.

Based on these considerations, the following objectives have been defined:

- ✓ To overcome the inconsistencies in the sample preparation and testing phases and develop a new, standard methodology for uniaxial and diametrical compression tests;
- ✓ To explore the correlation between granule strength and pellet deformation and propose a new model for both uniaxial and diametrical compression;
- ✓ To develop a DEM model able to describe the uniaxial testing procedure, providing reliable results at different operating conditions.

The dissertation will develop following a logical structure. In Chapter 1 an introduction of the theoretical background of the analysis will be presented, mentioning the most important previous works. Chapter 2 will introduce all the experimental methodologies and equipment that were used during the project: each technique will be introduced from a theoretical and practical point of view, justifying its choice and supporting useful details to better understand its steps. Furthermore, the requirements of the experimental analysis will be defined, with special focus on the uniaxial and diametrical compression procedures. In Chapter 3 all the experimental results will be presented and classified, highlighting the most interesting values and checking their correlation with the literature data. The chapter develops into four main sections: materials characterisation, mixing methodology validation, uniaxial testing results and analysis, diametrical testing results and analysis. The observations on the results are then collected and structured for the modelling phase, described in Chapter 4. In this chapter the uniaxial and diametrical datasets are analysed in dimensionless form, looking for correlations similar to the ones presented in §1.3. Each proposed model will be theoretically justified and validated through a fitting procedure. Then, in Chapter 5 the DEM simulation will be introduced, providing details on its design and comparing the results with the experimental datasets.

Chapter 1

Background and objectives

Particulate materials are defined as systems made of large numbers of macroscopic particles, whose rheological properties are determined both by the physical nature of the material and by the unique characteristics of the single units. These materials are commonly present in the environment: sands, wheats, rocks and even soil can be considered and treated as coordinated systems of particles with sizes in the order of μm, mm or even cm, that show an unique behaviour between liquid and solid systems [1, 2].

Particulate materials find applications in many industrial fields too, both as main or as by-products. Food and pharmaceutical industries in particular revolve around the processing of powders and particles, requiring an extremely high grade of quality and homogeneity throughout the whole manufacturing phase due to health and safety issues. At the same time, the processing of such irregular and tricky materials has to face many difficulties related to their unique nature. Transporting large volumes of powders requires, indeed, techniques that are significantly different from the handling technologies of any liquid or gaseous product, and that have to be able to deal with dust formation, material impurities and powder clogging. Moreover, any process equipment has to be run with close attention to any parameter that could cause disturbances to the complex equilibrium of the particles: unmonitored temperature and humidity values, for example, can easily induce clustering processes that degrade product properties or damage the equipment itself.

1.1 Granulation process

In order to deal with these issues, wet granulation is extensively carried out in many of the industries handling powders. In wet granulation processes particles are agglomerated together by distributing a liquid binder in the bulk powder, through the agitating action of a tumbling drum, a high shear mixer or any similar device. The resulting granules properties widely depend on the liquid's nature and on the liquid-solid interactions, which determine the strength of the forces holding together the solid particles, and on the liquid amount and distribution, which influence size and number of the granules.

Stronger granules are thus able to withstand rougher handling conditions, while their different bulk density and flowability could ease the storage and transportation phases as well as reduce the required storage volumes. Furthermore, granulation minimises dustiness in the final product, therefore reducing health hazards and explosion risks related to the dispersion of fine particles in closed environments.

Given the huge impact of granulation processes on the powder industry, many studies focused on the mechanisms taking part in the formation of the granules and on how to properly influence their properties. The main issues were related to the prediction of final products properties in the case of variations in the formulation and/or in the operating conditions, which required long and expensive testing phases [3]. To overcome the lack of predictive models, researches [4] focused on the three phases of granulation processes: nucleation and binder distribution, consolidation and growth, attrition and breakage, shown in Figure 1.1:

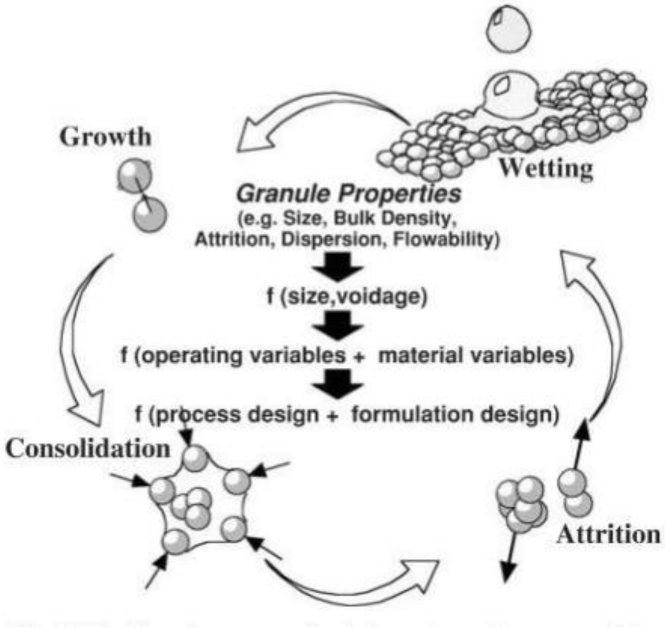

Figure 1.1: *Representation of the various phases of granulation processes, including wetting and nucleation, growth and consolidation, attrition and breakage. (Reprinted from* [5]*)*

1.1.1 Nucleation and binder distribution phase

During the nucleation and distribution phase a liquid binder such as water, natural polymers, silicone oils, is distributed on the powder bed as droplets of desired size, and penetrates the bulk of the material creating the initial nuclei. In most applications the liquid is sprayed through a nozzle on the powder bed, which is kept in motion through the agitation action of an impeller or thanks to a rotating tumbler structure. A schematic representation can be seen in Figure $1.2a$ and $1.2b$:

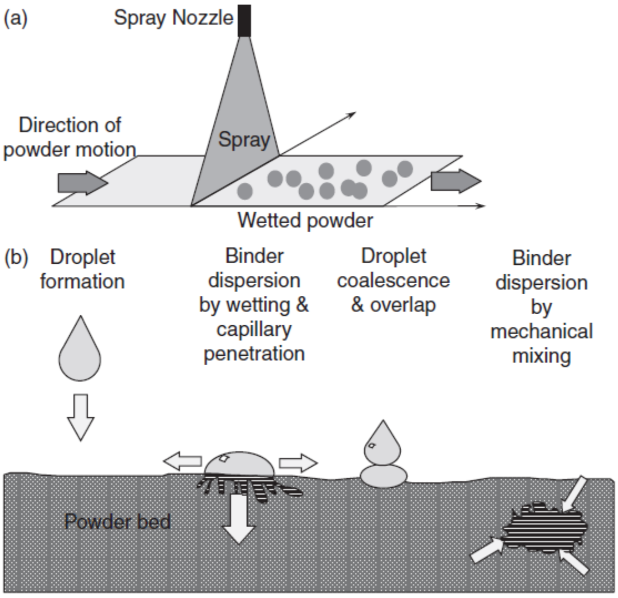

Figure 1.2: *Representation of the wetting and nucleation phase during a granulation process. (a) Schematic view of the spray zone; (b) Schematic view of the nuclei formation. (Reprinted from* [6]*)*

The size and rate of distribution of the liquid droplets are crucial parameters in the product's characteristics, as they can influence the final size distribution of the granules [7]. Furthermore, poor wetting can result in a large amount of not-granulated leftover material that has to be separated and recycled back to the process [8], therefore particular care has to be taken in the evaluation of the optimal operating condition for the binder dispersion.

The wetting kinetics has a major role in the overall process: the speed at which new wet surface is created depends on the rate of generation of drops' projected area, $\dot{A}_{drop}$ and on the rate at which new solid surface passes under the spray zone, $\dot{A}_p$ [9,10]. The ratio of these two area fluxes is the dimensionless spray flux number Ψ_a, which depends on droplets diameter, liquid flow rate, powder surface movement speed and width of the spray zone. For low values of spray flux number, a large amount of new powder surface flows under the nozzle and there is a high possibility that each droplet finds a free area to land, thus creating more liquid nuclei. For high spray flux number, droplets are likely to overlap and reduce the overall number of nuclei, which will also have a broader initial size distribution.

The wetting process is also controlled by thermodynamic parameters such as binder's surface tension and its contact angle with the particles, which determine how easily the liquid can wet the solid material. In particular, the velocity with which the droplet can penetrate the powder bed is a crucial parameter in obtaining a narrower granule size distribution: the quicker the drop sinks in the powder bed, the more unlikely it will be that two or more drops overlap creating a larger nucleus. This phenomenon is characterised by the dimensionless drop penetration time τ_p, a parameter depending both on wetting kinetics and thermodynamics and representing the time required for the penetration compared to the characteristic time of the system [4, 11]. Lower values indicate a narrower size distribution of the forming nuclei.

From the values of dimensionless spray flux number and dimensionless drop penetration time it is possible to represent the phenomena through a regime map, as shown in Figure 1.3:

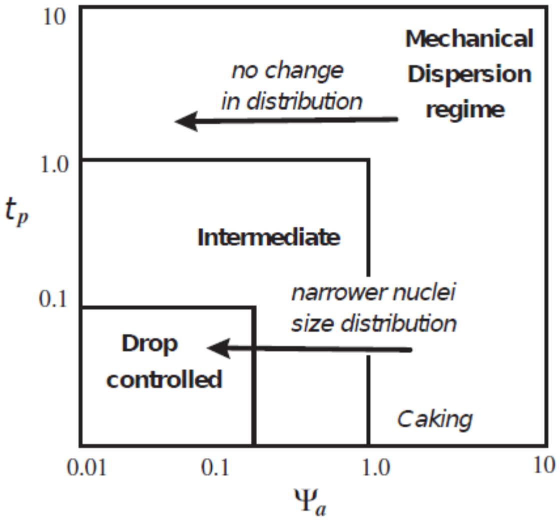

Figure 1.3: *Nucleation regime map. (Reprinted from* [6]*)*

In the drop controlled regime, low spray flux and penetration time grant a narrow nuclei size distribution, which is optimal for obtaining a product with regular PSD. In the mechanical dispersion regime the nuclei size distribution is irregular and depends only on the effect of shear in the nearby of the impeller or chopper zone, which gives a broad product size distribution and thus is not desired for most operations.

1.1.2 Coalescence and consolidation phase

As soon as the droplet has penetrated the powder bed and created the nucleus, the second phase of wet granulation begins. The nuclei compact and consolidate because of impacts with the agitator, with other granules or with the walls of the structure, squeezing out part of the liquid contained between the particles. In order to enable granule growth due to coalescence mechanisms, the kinetic energy of the nuclei must be dissipated during the creation of a granule bond able to resist the external impact forces [2, 7]. The parameter determining whether coalescence will occur is the Stokes deformation number St_{def}, relating the kinetic energy of collision to the energy dissipated during granule deformation [4, 11, 12]:

$$St_{def} = \frac{\rho U^2}{2Y} \tag{1.1}$$

where ρ is the granule density (kg/m^3), U is the average relative granule collision velocity and Y is the granule dynamic yield strength. Iveson *et al.* [13] further analysed the relationship between pore saturation and Stokes deformation number proposed by Iveson and Litster [14], developing the growth regime map shown in Figure 1.4.

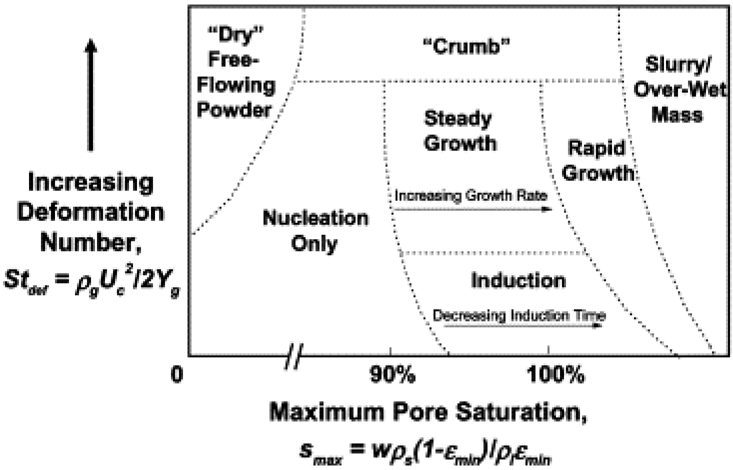

Figure 1.4: *Granule growth regime map. (Reprinted from* [13]*)*

The behaviour depends, for systems at high pore saturation, on the strength of the granule during its deformation: a weak granule has high St_{def} and tends to form an over-wet mass not suitable for coalescence mechanisms, while a strong system shows an induction time behaviour that slows the growth process [15, 16, 17, 18].

1.1.3 Breakage and attrition phase

The third phase of the granulation process consists in two phenomena, depending on the granule condition. Granules can undergo attrition and fracture mechanisms during both granulation (breakage) and drying processes (attrition), due to collisions with other granules or with the equipment. These phenomena lead to a reduction in the average size of particles and to the production of fines, which may be an issue for further processes. The mechanism mainly depends on the mechanical properties of the dry granule, fracture toughness and elastic modulus.

On the other hand, wet granules may break in smaller pieces inside the granulator due to the continuous collisions and impacts with the process equipment: the model proposed by Tardos et al. [12] suggests that this phenomenon, which appears simultaneously with the coalescence and growth phase, occurs only for values of St_{def} smaller than approximately 0.2. For larger values the granule strength is so low that the impact will largely deform the granules, leading to their breakage and preventing consolidation mechanisms. Therefore, the evaluation of the Stokes deformation number, and thus of granule strength, allows to predict the behaviour of wet powders inside a granulation machine without the need for expensive on-field testing [14].

1.2 Theory of granule strength

From the theoretical analysis of the liquid binding between solid particles, three main components have been found to take part in determining the strength of the bond: inter-particle friction, capillary and surface tension forces, and viscous forces [4, 9, 11].

Inter-particle friction can be generally described by the Coulomb relation:

$$\tau_f = \mu_f \sigma_n + c_h \tag{1.2}$$

where τ_f is defined as the shear stress at failure, μ_f is the coefficient of internal friction, σ_n is the loading normal stress and c_h is the shear stress in case of no normal loading, defined as cohesivity. Even though various improvements have been proposed, the model is still suitable for the study of wet granulation, as it takes into account the dissipative and slight strain-rate dependency nature of the granules in normal operating conditions [19].

Capillary forces have been the topic of a wide range of experimental and theoretical studies [2, 21] aiming at finding suitable models able to approximate the Laplace-Young equation:

$$\Delta P_{cap} = \frac{2\gamma}{r} = \gamma_{LV}\left(\frac{1}{r_1} - \frac{1}{r_2}\right) = \gamma_{LV}\left(\frac{\ddot{y}}{(1+\dot{y}^2)^{3/2}} - \frac{1}{[y(1+\dot{y}^2)]^{1/2}}\right) \tag{1.3}$$

where ΔP_{cap} is the capillary suction pressure across the liquid-vapour interface, $\gamma$is the liquid surface tension, r is the curvature of the bridge surface, which can be calculated from the two radii of curvature of the liquid surface, r_1 and r_2. The radii can be calculated for every point along the bridge profile y through its derivatives, $\dot{y}$ and $\ddot{y}$. Figure 1.5 shows an exemplification of the liquid bridge geometry:

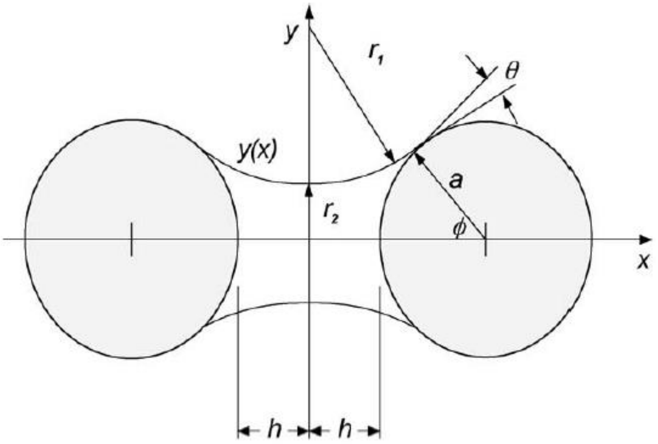

Figure 1.5: *Representation of the liquid bridge geometry. (Reprinted from* [19])

Parallel work by Rumpf [22] developed a model for predicting the granule tensile strength σ_p taking into account more dimensional parameters:

$$\sigma_p = 6 \cdot S\left(\frac{1-\varepsilon_{gr}}{\varepsilon_{gr}} \cdot \frac{\gamma cos\theta}{d_p}\right) \tag{1.4}$$

where S is the liquid pore saturation, ε_{gr} is the granule porosity, γ is liquid surface tension, θ is the liquid-solid contact angle and d_p is the particle diameter. A binder with low surface tension decreases the granule strength due to Equation 1.3, while the presence of smaller particles increase σ_p, due to the larger volume of inter-particle contacts.

Viscous forces are generated by the dynamic compression or stretching of the liquid bridge between two solid particles, as occurs during granulation processes. The work of Van den Dries [23] lead to the evaluation of suitable models, then integrated by Liu [24] with the existing theory about capillary forces for a more comprehensive description of the phenomena:

$$\sigma_p = AR^{-4.3}S\left[6\frac{1-\varepsilon_{gr}}{\varepsilon_{gr}} \cdot \frac{\gamma cos\theta}{d_p} + \frac{9}{8}\frac{(1-\varepsilon_{gr})^2}{{\varepsilon_{gr}}^2}\frac{9\pi\mu v_p}{16d_p}\right] \tag{1.5}$$

where AR is the aspect ratio of the primary particles, μ is the binder viscosity and v_p is the relative velocity of the moving particle after an impact has occurred.

These results highlight how the parameters involved in the determination of granule strength have complex interactions between each other, and that an extended framework of experimental data is required to fully understand the behaviour of wet granular materials and the correlations between previous models.

1.3 Experimental analysis of granule strength

The role of granule strength is fundamental in determining their growth behaviour during the granulation process and the final size distribution of the product, therefore acting as a regulating parameter in the feasibility analysis of the process. A weak, deformable granule tends to break easily during collisions preventing any growth mechanism, while a too strong granule requires an induction period during which liquid binder is squeezed into the granule thanks to consolidation mechanisms. As can be seen in Figure 1.2 a halfway strength, corresponding to values of $St_{def} \cong 0.1$, is suitable for the steady growth of granules. At these operating conditions two colliding granules show a large contact surface, which is suitable for the formation of a strong bonding able to resist the breakage phenomena described in §1.1.3 [11].

Knowing granule strength and impact velocities in the granulator thus seems to be sufficient to successfully predict the granule growth behaviour in any granulation process, even though assessing the effects of various parameters onto St_{def} has required years of research. Most of the initial studies focused on the effect of slow deformation of granular materials with low viscosity binders, for which the dynamic mechanism of granulation is overlooked [25]. Further works by Iveson and Litster were able to evaluate the liquid bridge's strength between two moving particles [26] while the increased computational capability allowed to properly simulate the impact coalescence through DEM models, considering viscous and inter-particle energy dissipation effects [27].

With the broad and comprehensive work of Iveson *et al*,. more and more parameters and operating conditions were taken in account for the testing. The effect of binder viscosity was widely analysed [25, 28, 29], highlighting its major effect on granule strength: a high viscosity binder decreases the rate of consolidation, as it increases the resistance of the granule to any kind of deformation, while a low viscosity binder improves the lubrication between granules, thus increasing the rate of consolidation [3]. The effect of high strain rate was analysed in various works taking into account its interactions with other parameters, such as binder viscosity, surface tension, contact angle, strain rate, particle size and shape [19, 30, 31, 32].

Most of the tests were carried out mixing powders and liquid binder by hand, and preparing cylindrical pellets of fixed size and aspect ratio. Spherical glass ballottini, silica powders and lactose were the materials chosen for the testing, while silicone oils with viscosities going from $0.01\ Pa \cdot s$ to $60\ Pa \cdot s$ [19], and up to $2400\ Pa \cdot s$ [31] were used as binders. Such pellets were then compressed with high-speed dynamic load frames (Instron DynaMight^{TM}, Instron ElectroPlus E1000) at various velocities [19, 30, 31], in order to obtain a wide range of values able to describe different agitation regimes inside the granulator. Compression tests were carried out both axially [19, 30, 31] and diametrically [32], looking for correlations between the strength of the samples and the operating conditions.

The obtained results shown how the granule's peak stress, which is the maximum stress that the granular material can sustain while being deformed, changes depending on all the operating values with a profile described by:

$$Str^* = 5.3 + 280 \cdot Ca^{0.58} \tag{1.6}$$

$$with \quad Str^* = \frac{\sigma_c d_p}{\gamma cos\theta} \quad and \quad Ca = \frac{\dot{\varepsilon}\mu d_p}{\gamma cos\theta}$$

where Str^* is the dimensionless strength, defined as the ratio of peak flow stress to capillary forces, Ca is the capillary number, defined as the ratio of viscous to capillary forces. σ_c is the peak flow stress (kPa), d_p is the particle surface mean size (m), γ is the liquid surface tension (N/m), θ is the contact angle between binder and solid particle, $\dot{\varepsilon}$ is the strain rate (s^{-1}) seen as the ratio between deformation speed and the size of the granule, and μ is the binder's viscosity ($Pa \cdot s$). Figure 1.6 and 1.7 shows the experimental results obtained by Iveson *et al.* [19] and Sweat *et al.* [31] compared to Equation 1.6, for a wide range of operating conditions:

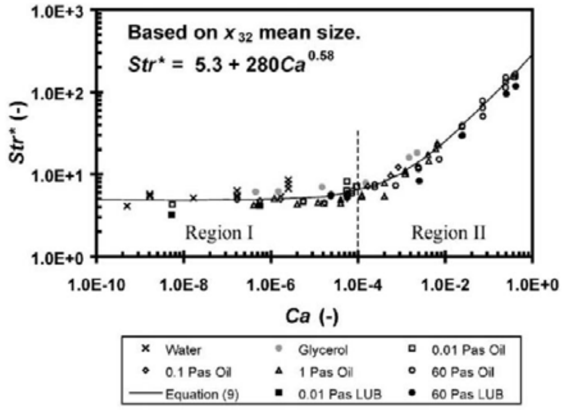

Figure 1.6: *Theoretical and experimental values for dimensionless peak flow stress Str* versus capillary number Ca. (Reprinted from* [19]*)*

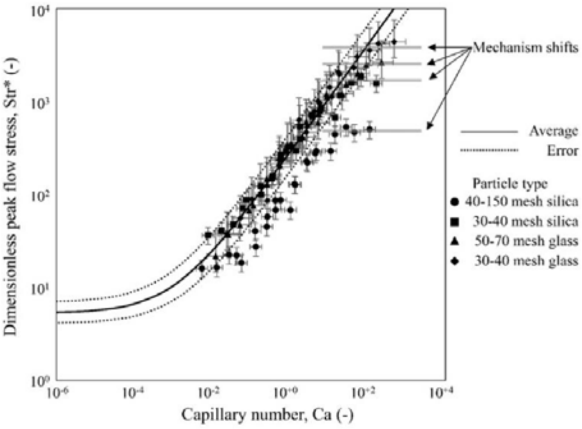

Figure 1.7: *Theoretical and experimental values for dimensionless peak flow stress Str* versus capillary number Ca with high viscosity binders. (Reprinted from* [31]*)*

From the graphical representation it is clear how two main regions can be individuated depending on capillary number's values: at low Ca viscous effects are not relevant and the dimensionless peak flow stress has almost a constant value, determined by Equation 1.6. But for values of capillary number higher than 10^{-4} the contribution of viscous effects becomes considerable in determining the granule's strength, and this behaviour is accordingly described by Equation x, as the right-hand term becomes relevant in the final value of Str^*. This result was particularly significant as it highlighted the fact that granule strength measured in pseudo-static conditions, such as low strain rates, may not be representative of its behaviour in many commercial high-speed granulators, in which the applied strain rates are by far larger.

Further studies by Smith [8] extended the understanding of the granules' behaviour introducing the effect of primary particles aspect ratio AR, to take into account the particle shape effect first considered by Iveson *et al.* [30]. The validated empirical model is shown in Equation 1.7:

$$Str^* = AR^{-4.3}(7 + 221 \cdot Ca^{0.58}) \tag{1.7}$$

This empirical model is able to predict, with good accuracy, the strength of a given granular material in the wide range of operating conditions considered by the previous researches. Table 1.1 presents a recap of the effects of each parameter on granule behaviour, as evaluated by previous studies.

Table 1.1: *Granule strength dependency from the main operating parameters in granulation processes.*

Parameter	Effect on granule behaviour
Binder surface tension γ	An increase in surface tension decreases granule consolidation rate due to the increase in capillary, viscous and frictional forces, giving a stronger granule [29]
Binder viscosity μ	An increase in binder viscosity causes an increase in viscous forces and thus in granule strength [18, 19, 29, 30, 31, 32, 33]
Binder content	Increasing its content has complex effects, as it reduces inter-particle friction while increasing viscous forces. The behaviour depends on their relative values [18, 29]
Particle size	An increase in particle size reduces the number of contacts between particles, and thus inter-particle friction. Furthermore, the liquid bridge curvature decreases due to an increase in particle diameter, causing a reduction in capillary forces. Viscous forces decrease, too, all leading to an overall decrease of granule strength. [18, 34]
Aspect ratio	An increase in aspect ratio (thus, a more spherical particle) reduces the granule strength, due to the combined effect of inter-particle attrition and interlocking [30]

1.4 Project objectives

The wide and comprehensive researches of the previous years deeply analysed the role of the main parameters influencing the behaviour of wet granular materials undergoing deformation stresses. Nevertheless, the methodologies used for sample preparation and testing were inconsistent among these studies and did not take into account many factors, mainly being the quality of the liquid-solid mixing, the control of the stresses applied during the pellet preparation phase and the geometrical consistency of different samples.

Moreover, the effect that a pre-existing compression could have on the strength of a granule during granulation processes has never been analysed, as well as its correlation with the flowability of the material. Furthermore, a limited amount of materials were analysed, and many of the chosen ones (glass beads, copper powder, silica sand) had low interest for the food and pharmaceutical industries.

Given the existence of these gaps in the literature, this research project aimed at achieving the following objectives:

- ✓ To overcome the inconsistencies in the sample preparation and testing phases and develop a new, standard methodology for uniaxial and diametrical compression tests;
- ✓ To explore the correlation between granule strength and pellet compression and propose a new model for both uniaxial and diametrical compression;
- ✓ To develop a DEM model able to describe the uniaxial testing procedure, providing reliable results at different operating conditions.

Chapter 2

Materials and methods

The chapter is divided into two main sections: a description of the main materials tested during the experimental investigation, and an overview of the methods and the equipment used for the results evaluation. The objective is to present with a clear and plain structure the different choices regarding the equipment and the material usage, as well as setting an operative methodology for future studies.

2.1 Materials

The selection of the materials chosen for the project was based on a series of different considerations, based on factors such as their availability or their recurrence in previous works. This section illustrates their characteristics and properties.

2.1.1 Powders

In most of the previous works [8, 13, 14, 18, 19, 30 − 33] the materials analysed were glass ballottini and lactose powders, due to their low cost and wide availability. Glass ballottini is a spherical powder, usually made of glassy materials, particularly useful for experimental studies because of its ease of characterisation and its regular structure. These properties make it suitable for any application in which an ideal, steady behaviour has to be tested. Lactose is a disaccharide commonly contained in any dairy product, and in its powder structure is used as a carrier and stabiliser of aromas in many food products or as an additive to pharmaceutical tablets and capsules. Its irregular particle shape made it especially interesting for studying the effect of this parameters on the strength of wet granular materials [8, 30].

One of the objectives of the study was to extend the knowledge of granule strength to new materials that have not been tested by previous works, providing new data for the empirical models. At the same time, the modelling of systems of irregular particles requires a high computational effort that is unfeasible with the length of this study, so the choice fell on two pseudo-spherical particles: MCC Celphere^{TM} and PMMA Elvacite® 3001. MCC Celphere^{TM} is a specific typology of micro-crystalline cellulose supplied by Forum Products Ltd (Crown House, 2-8 Gloucester Road, Redhill, Surrey, RH1 1FH, UK) and characterised by a high sphericity and aspect ratio. Micro-crystalline cellulose is a carbohydrate obtained through depolymerisation processes of cellulose, and is widely used in pharmaceutical applications as a binder/diluent in capsules and tablets. The material is obtained through a sphenorization process of powder grade MCC, and is generally used as a seed core for controlled release and taste masked pellets, as well as a seed core for drug layering and film coating. Three typologies were used throughout the experimental analysis, in order to investigate the behaviour of MCC at different particle size: Cp-102, Cp-203 and Cp-305.

The second material chosen for the testing was a poly-methyl-methacrylate (PMMA) powder with commercial name Elvacite® 3001, supplied by Tennants Distribution Ltd (Ryders Green Road, West Bromwich, West Midlands, B70 0AN, UK). Elvacite® 3001 was selected both because of its spherical particle shape and because no previous work ever focused on its behaviour in granulation processes. Thus, even not being a material commonly granulated, there is large interest in extending the current knowledge of this powder behaviour.

Further characterisation of the particle size and shape of MCC Celphere™ and Elvacite® 3001, as well as their particle size distribution, can be found in §3.1.

2.1.2 Liquids

Different liquid binders were chosen in order to grant a broad range of different behaviours, and to give results comparable with previous works. A 500 centiStokes and a 30000 centiStokes silicone oils were used for most tests. See §2.2.4 for further details on the preparation technique. Water, initially considered to evaluate the strength of wet granular samples at very low capillary numbers, was discarded as it gave issues during the sample preparation phase. The powder-water samples indeed required over 40% w/w of binder to be freestanding (compared to the 6% of the powder-oil ones), thus it was decided not to introduce the binder content as a further degree of freedom and focus on the other parameters.

Data regarding surface tension, dynamic viscosity and density were not measured but collected from previous literature works [8, 19] or from information given by the supplier. Surface tension of silicone oils was assumed to be constant at different densities, as suggested by previous works [8, 32]. Table 2.1 collects a summary of the data.

Table 2.1: *Summary of binders' properties.*

Liquid	Density $[g/ml]$	Viscosity $[Pa \cdot s]$	Surface Tension $[N/m]$
500 cSt Silicone Oil	0.970	0.485	0.261
30000 cSt Silicone Oil	0.975	29.25	0.261

2.2 Methods and Equipment

Various methods and equipment have been used throughout the experimental analysis, aiming at defining a standardised testing methodology able to supply quick and consistent results for many different materials. The procedure used is broadly satisfactory as regards the samples preparation and the uniaxial compression phases, while the diametrical compression tests gave some difficulties during the interphase between preparation and testing. The following sections describe the methodologies and the equipment for each test.

2.2.1 Particle size analysis

The effect of particle size on granule strength has already been introduced in §1.3 as one of the main parameters in the determination of both dimensionless strength and capillary number. Therefore, an extensive knowledge of the size and distribution of the powders employed is mandatory to supply the optimal values and improve the model's reliability.

Any poly-disperse system is indeed described by a distribution of particle sizes, which broadness determines the behaviour and characteristics of the material. The description of the system is based on the choice of an equivalent diameter, a parameter defined as the diameter of a sphere that has the same value of a given property as the particles of interest [35]. The choice of the property to consider depends on factors such as the method used or the available equipment, as often different instruments measure different equivalent diameters. For the particle characterisation the equivalent diameter based on projected area, d_A, was evaluated through the use of a QicPic SYMPATEC® machine.

QicPic is an image analysis technique which uses a pulsed light source to "freeze" the particles, while a high-speed, high-resolution camera captures their projections [36, 37]. The camera frequency goes up to 500 frames per second: this allows a quick and precise representation of the particle size distribution of a powder, with a wide measuring range going from 0.55 micrometres to 34 millimetres. The machine thus measures the projected area of the particles and, through its processing software, evaluates their d_A and other shape descriptors.

A picture of the QicPic SYMPATEC® used, equipped with a Gradis/L gravity dispenser and a Vibri/L dosing unit, can be seen in Figure $2.1.a$. Figure $2.1.b$ and $2.1.c$ show a schematic and a picture of the measuring section, respectively:

Figure 2.1.a: *QicPic SYMPATEC® machine. (Taken from* [38]*)*

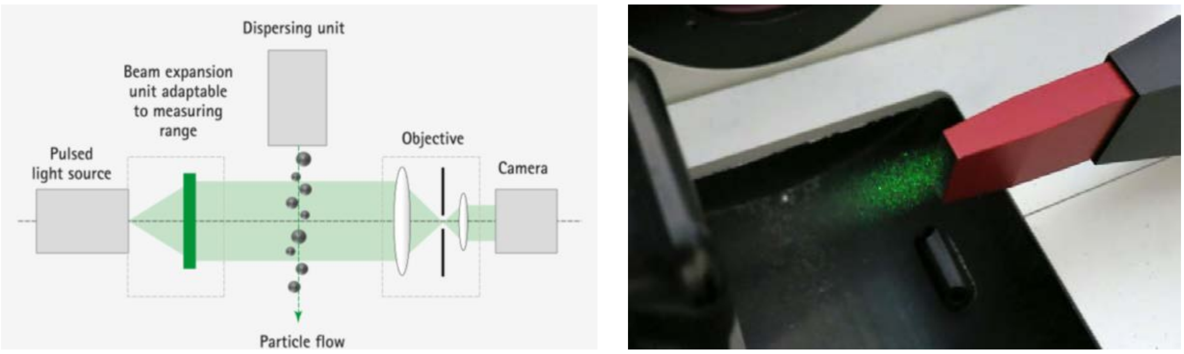

Figure 2.1.b, 2.1.c: *Schematic and picture of the particle size measurement section in the QicPic SYMPATEC®. (taken from* [38]*)*

In the case in exam particles size distribution (PSD), average diameter and aspect ratio were the data of interest, as their influence on granule strength has already been demonstrated [8, 9]. Whereas the PSD was particularly broad, a sieving step would have been required to avoid to introduce a further degree of freedom in the granule strength analysis [39]. The results of the QicPic testing can be found in §3.1.2 and §3.1.3.

2.2.2 Optical analysis

An initial analysis of the particle shape was carried out using an Olympus DSX500 optical microscope, produced by Olympus (KeyMed House, Stock Road, Southend-on-Sea, Essex SS2 5QH, U.K), to better understand how the single particle characteristics may influence the macroscopic powder behaviour. The images were captured both for MCC Cp-305 and for PMMA, which have an average particle size large enough to give meaningful information when observed with an optical microscope. The pictures can be found in §3.1.4.

To further improve the knowledge of the tested materials, a scanning electron microscope (SEM) was used to produce detailed images of the single particles. During this procedure a focused beam of electrons scans the surface of the particle, interacting with the material's atoms: the emission of secondary electrons, detected with an Everhart-Thornley detector, are elaborated in order to obtain an image of the particle. With this technique resolutions up to 1 nanometer can be reached: it is thus possible to obtain a highly detailed representation of the particles in exam, whose size ranges between 10 and 10^3 micrometers.

The microscope used for the measurements was a Jeol JSM-7100 F (Jeol Uk Ltd., Silver Court Watchmead, Welwyn Garden City AL7 1LT), with a guaranteed resolution of 1.2 nanometers and a magnification up to 1,000,000 times. The three powders analysed, MCC Cp-102, Cp-305 and PMMA Elvacite® 3001, were deposited on the sample structure and coated with a 4 nanometers layer of gold, using a Jeol Sample Coater (produced by the same company). The coating is required as the materials in exam have a non-conductive nature, which inhibits the emission of secondary electrons and thus prevents the image elaboration. A few nanometers layer of a conductive metal is generally considered not thick enough to hide the surface morphology, but able to provide a conductive coating to dissipate charging effects, prevent any resultant heat build up and minimise particle damage due to the electron beam.

The coated sample was then positioned in the sample chamber of the SEM and brought into vacuum conditions. Choosing an accelerating voltage of 5 kV, three sets of images were captured for each powder, with a magnification of $50, 100$ and 250 times. The images and their elaboration can be found in §3.1.5.

2.2.3 Contact angle

The models shown in Equation 1.6 and 1.7 correlate the strength of the granular material with both solid and liquid properties. But, if information on particle average diameter d_p and liquid surface tension γ can be easily evaluated or given by the supplier, the solid-liquid contact angle has to be determined for each couple of materials. Furthermore, most of the existing studies focused on the contact angles of couples of more common of materials, such as glass ballotini and water or silicone oil [40], while no work was found out for MCC and PMMA powders.

Thus, as there was no data available for the powder-binder combinations chosen for this study, it was necessary to experimentally evaluate the contact angle of silicone oil with both MCC and PMMA. The experiments were carried out using a FTA1000 B-Class Drop Shape Analyser produced by First Ten Angstroms Inc., 465 Dinwiddie Street, Portsmouth, VA, shown in Figure $2.2.a$. The testing container was filled with silicone oil and positioned in front of the instrument lens, focusing on the air-liquid surface. Then, a single solid particle was gently deposited on the interface, and its interaction with the liquid was observed through the instrument software. The contact angle could then be evaluated from the pictures as shown in Figure $2.2.b$, using the DropSnake plug-in of ImageJ as described in previous works [41].

Figure 2.2.a, ***2.2.b***: *FTA 1000 B-class Drop Shape Analyser by FTA, used for contact angle measurements, and detail on how to evaluate the contact angle.*

Given the similar thermodynamic nature of the two silicone oils, the experiments were carried out just for the low viscosity one, assuming that the contact angles would be the same also for the high viscosity oil. For MCC Celphere™, Cp-305 was selected for the testing due to its larger average size, which would make the image elaboration simpler to carry out. For Elvacite 3001®, larger particles were selected for the same reason.

For both materials the particles sank in the silicone oil: this behaviour corresponds to a complete wettability of the particle by the liquid, meaning that the contact angle between the solid-liquid system is close to zero. This value is consistent with previous works [40], which allow to classify silicone oils as low surface energy liquids. The analysis of the experimental images can be found in §3.1.6, as well as their correlation with the corresponding particle shape.

2.2.4 Wet granular material preparation

The samples were prepared using an average value of 6% w/w of liquid binder. This value, slightly lower than the one used in the works of Iveson, Smith and Sweat [8,19,30,31], was chosen to ease the uniaxial testing phase: higher binder contents indeed caused more particles to stick to the equipment surface, which lead to having not free-standing samples. Nevertheless, as shown by the experimental evaluation, the data can be considered consistent with the ones obtained by previous studies.

Furthermore, in all the previous published works [8,19,30,31], little to no attention was put in the methodology of preparation of the wet granular samples. The binder was simply added into a bag containing the powders and hand mixed until the mixture looked homogeneous at a visual inspection. This could have led to high inconsistency between samples taken from different batches, as various binder lumps could have been present without being noticed. Furthermore, segregation effects could have caused a separation between binder-rich agglomerates and dry material due to their different densities, so that samples taken at different times could show different binder contents and, thus, different granule strength.

A new preparation methodology was investigated in order to fix a simple, effective and repeatable technique, able to improve the consistency of the samples properties and the quality of the mixing. A Turbula® shaker mixer, as the one shown in Figure 2.3, was chosen to grant a quick and high-quality mixing.

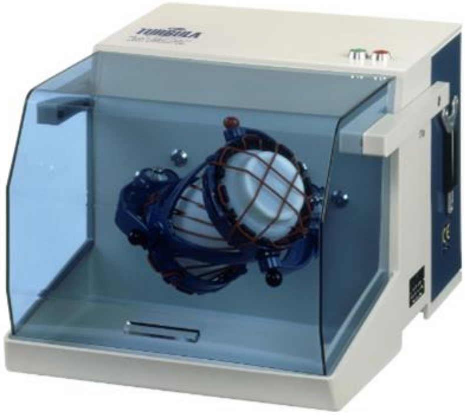

Figure 2.3: *Turbula® shaker mixer with one of the containers used.*

The technical characteristics of the mixer can be found in Table 2.2.

Table 2.2 *Technical data of the Turbula® shaker mixer.*

Parameter	Value
Volume of the container	1 litre
Container filling ratio	50%
Diameter of the container	9 cm
Height of the container	20 cm
Available velocities	$23 - 34 - 49 - 72 - 101$ rpm

The work of Mayer-Laigle *et al.* [42] was taken into account during the choice of the operative speed, but further experimental characterisation was carried out considering the presence of a 6% by mass of liquid binder. The final results lead to the choice of a 20 minutes mixing time module with a 72 rpm mixing velocity for samples prepared with 500 cSt silicone oil, while for samples made with 30000 cSt silicone oil two mixing modules were required to obtain a good dispersion of the binder. See §3.2.1 for the full experimental characterisation. The wet granular materials were then visually inspected to check their homogeneity and verify that no binder lumps were present.

Out of over 15 batches prepared only two shown binder-rich granules, and in both cases the materials used were MCC Cp-102 and the high viscosity silicone oil. This could be due to the

binder addition methodology and to its high viscosity: the liquid could only be poured into the container through its opening, slowly distributing on the upper powders layer and thus promoting the formation of a single, viscous liquid mass. Furthermore, due to its high viscosity, the time it requires to penetrate into the solid mass is almost two order of magnitude larger than the one for the low viscosity binder, further enhancing this issue [43].
In both cases the binder lumps were broken with a metal spatula and dispersed in the powder bulk, and the sample was put in the Turbula® mixer for a further mixing module. The final samples were homogeneous at a visual inspection, and their testing results were consistent with the ones from other batches.

A further factor to take into account is the compaction mechanism due to gravity, which could interest any sample whose testing phase is delayed with respect to the preparation phase. Due to the time schedules of the laboratory equipment it has not always been possible to test all the samples immediately after they were prepared, so the effect of powder compaction on the strength of the granules could not be neglected. To prevent this effect and improve the consistency of the data measured from different batches, before each testing phase the tank containing the wet granular material of interest underwent a short mixing session at 72 rpm for 2 minutes, allowing any pre-existing consolidation stress to relax and preventing the effect of segregation.

Furthermore, particular care was taken in preventing any unrequired contact between the materials and the environment, so that air humidity could not have any relevant interference on the wet granular material behaviour.

2.2.5 Advanced Uniaxial Powder Tester

One of the most important properties in the evaluation of the behaviour of a granular material is its flow function, written as:

$$\sigma_c = f(\sigma_1) \tag{2.1}$$

where σ_1 is the major principal stress (MPS) and σ_c is the unconfined yield stress (UYS). The flow function allows to evaluate the stress required for a sample of granular material to fail (UYS) when a certain preliminary consolidation stress (MPS) is applied. For a given couple of stresses, it can be written that:

$$\sigma_c = \frac{1}{ff}\sigma_1 \tag{2.2}$$

where ff is the flow factor. If the flow function has a linear trend in a given set of consolidation stresses, it could be represented by Equation 2.2. This allows to classify granular materials flowability on the base of their flow factor: given a fixed consolidation stress, a free-flowing material will show a lower unconfined yield stress than a more cohesive one.

Two main testing methodologies are available for the flow function evaluation, uniaxial and shear cell testing. Both begin applying a normal pre-compression stress to a confined cylinder of granular materials, which transfers through all the powder bulk, but the successive phase differs between the two methods. In shear cell testing, which is historically the most used methodology, a shear cell is used to apply a rotation movement to the compressed powder sample and to measure the shear stresses at different consolidation stresses. The values are then represented using *Mohr's stress circles*, from which the UYSs are extrapolated for each consolidation stress and used to evaluate the flow function of the material.

On the other hand, in uniaxial testing no rotational movement is applied to the material: once the material has been compressed, the confining walls are removed and the sample is compressed again, until the failure stress is reached. Figure 2.4 shows a schematic of the procedure:

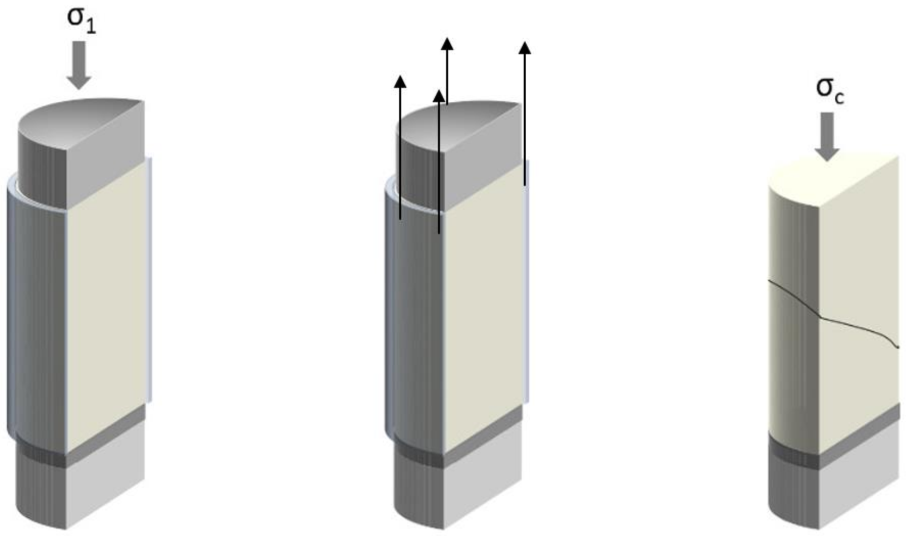

Figure 2.4: *The three steps of uniaxial testing for a general granular material, section view: sample consolidation, wall removal, sample failure. (taken from* [44]*)*

This methodology, by far simpler and more immediate than the biaxial tests, has many limitations regarding the testable materials. Whereas shear cells allow to test even really free-flowing materials, uniaxial testing requires the powder to be free-standing once the external cylinder is removed. Therefore many commonly used powders, such as MCC, are not suitable for uniaxial testing. Furthermore, a specific methodology for removing the external container without deforming the sample had to be designed before the test could be considered viable.

But wet granular materials, as the ones considered in this study, have by far stronger inter-particle forces and thus can be uniaxially tested. The equipment used was the Advanced Uniaxial Powder Tester (AUPT), by Freeman Technology (Tewkesbury Business Park, Miller Court, Severn Dr, Tewkesbury GL20 8DN), which allows to carry out quick and consistent tests varying the operative parameters. The machine is designed to consolidate and compress, through a moving piston, cylindrical samples of powders at different velocities. Figure 2.5 shows a picture of the equipment, with a detail of the sample support and sleeves.

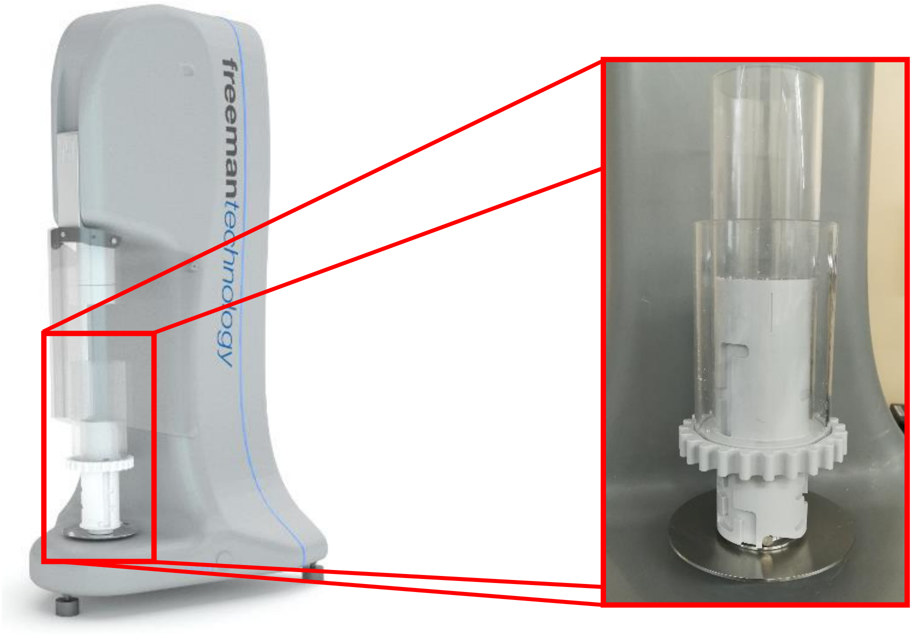

Figure 2.5: *AUPT machine, with a detail of the sample support.*

The testing procedure is rather straightforward and consists of the following steps:

1. Sample preparation: the material was poured inside the sample sleeve, which had three possible heights: 56, 75 and 100 millimeters. Attention should be paid to not apply any compaction stress to the powders, especially if working at low consolidation stresses. Any excess powder was removed with a sharp edge.
2. Sample consolidation: an initial pre-consolidation stress was applied for 30 seconds, equal to 25% of the total consolidation stress. The sleeve support collar was removed to allow double-ended consolidation, and the main consolidation stress was then applied for 30 seconds.

3. Unconfined testing preparation: the sample sleeve was raised and the consolidation stress was removed.
4. Unconfined testing: the piston descended to fail the powder at the set speed, measuring the failure stress and producing a report of the test data.

Throughout the test the software measures the piston position and the stresses applied, showing their values in a graph as the one shown in Figure 2.6.

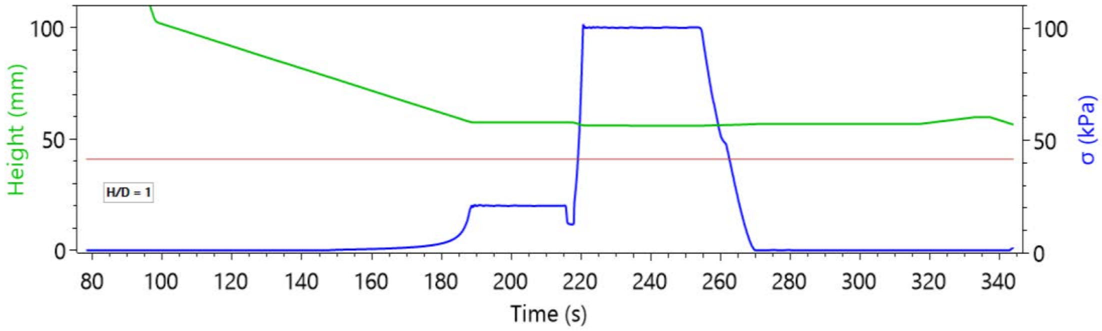

Figure 2.6: *Profiles of piston position and stresses applied to the sample, as reported by the AUPT software.*

The AUPT machine allows to carry out all the uniaxial compression tests that previously required an Instron® machine [8, 19, 30], but largely improving the consistency of the results. Indeed, it is no longer required to move and position the sample between the preparation and the testing phase, as the machine is designed to unify the procedures into simple steps that do not involve, at any point, an operator touching the sample. Furthermore, it allows to properly choose the consolidation stress to apply in the cylinder preparation phase, and to work even at low values that would otherwise cause the sample to deform and fail if prepared with an Instron® machine.

The machine allows to modify all the mechanical test parameters, too: pre-consolidation and consolidation stresses can be chosen in a range from 1 to 100 kPa, with a resolution of 0.3 Pa; pre-consolidation and consolidation times can be modified depending on the test objectives; consolidation and failure speed can be varied in the range from 0.01 to 5 millimetres per second, with a resolution of 0.6 micrometres per second. From this last parameter, knowing the sample height, it is possible to evaluate the strain rate and thus the capillary number for the sample. For a more detailed description of the experimental parameters used, see §3.3. Furthermore, from the collected data it is possible to evaluate the material's flow function as described by Equation 2.1.

Over 100 tests were carried out for both MCC Celphere™ and PMMA Elvacite 3001®, at five different consolidation stresses (20, 40, 60, 80, 100 kPa) and different values of failure speed, to provide a broad set of data suitable for the model fitting. The experimental results can be found in §3.3, while the model fitting procedure is described in §4.1.

2.2.6 Instron® testing

An Instron® 1175 Universal Testing machine was used for the preparation and the diametrical testing of cylindrical samples of the wet granular materials considered. This equipment allows to apply uniaxial loads with values up to 100 kN, registering the profile of plate position and stress applied as a function of testing time. Furthermore, the platen speed can be set through the machine software and increased up to 1 millimetre per second, thus enabling the achievement of a broad range of capillary numbers. Figure 2.7 shows a picture of the machine used for the tests, with a detail on the die used during the sample consolidation phase.

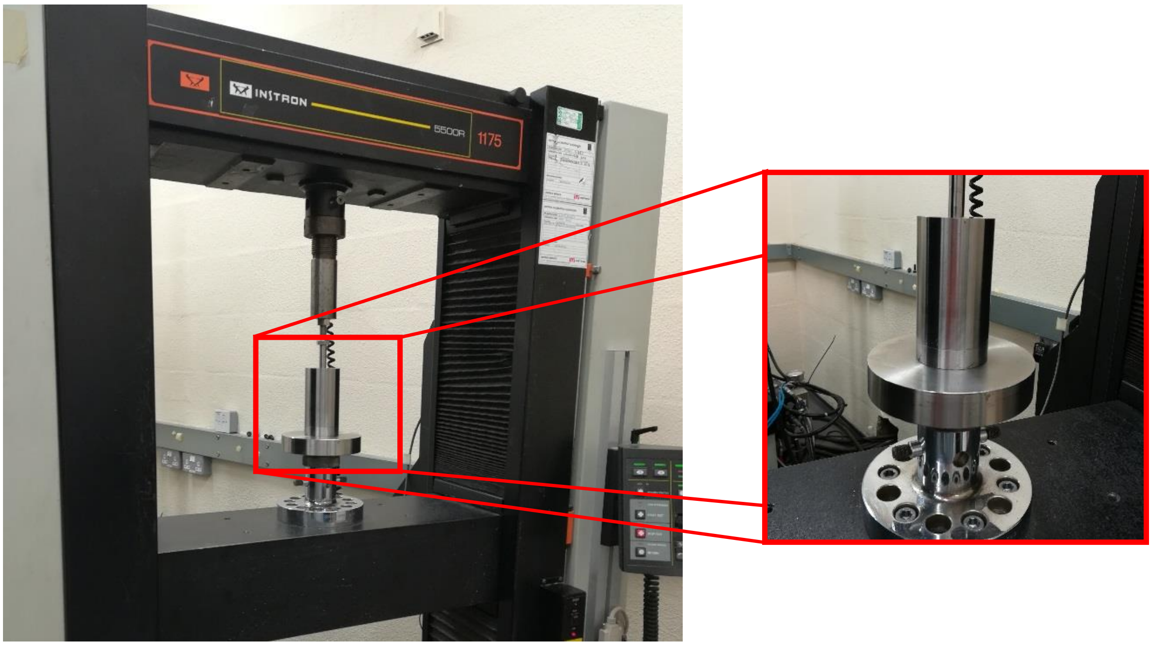

Figure 2.7: *Instron® 1175 Universal Testing machine, with a detail of the platen and of the die used for the sample consolidation.*

The diametrical testing experiments were designed to evaluate the strength of wet granular materials in conditions different from the uniaxial tests, and to investigate how the consolidation stress applied during the sample preparation phase influences the behaviour of the cylindrical pellet. The main objectives are to explore how formulation properties and testing conditions impact on the strength of granular materials, and to provide a model that correlates the consolidation stress applied in the preparation phase to the granule behaviour.

This experimental analysis was carried out using MCC Celphere™ and silicone oil. The PMMA samples indeed tended to deform during the sample positioning, regardless of the consolidation stress applied, thus giving inconsistent results during the testing phase. For this reason, it was preferred to use only the data obtained from the micro-crystalline cellulose samples.

The testing procedures were carried out at $20\ ℃$, and the materials were prepared as described in §2.2.4. The testing procedure consists of the following steps:

1. Sample preparation: a fixed mass of wet granular material was weighted and poured inside a die with internal diameter of $13\ mm$.
2. Sample consolidation: using the Instron® 1175 press, the sample was consolidated at different loads. For this study, consolidation loads of $10, 20$ and $30\ kN$ were chosen, corresponding to stresses of $75, 150$ and $225\ MPa$.
3. Sample extraction and preparation: the cylindrical sample was carefully ejected from the die trying to prevent any deformation, and positioned on the lower platen of the Instron® 1175 press.
4. Sample testing: the sample was compressed at different velocities, in the range from $0.005\ mm/s$ to $1\ mm/s$. The profiles of load versus time and displacement were collected in a CSV file and used for the further analysis.

Over 60 tests were carried out for MCC Cp-102 and CP-305, with both 500 cSt and 30000 cSt silicone oil and at different failure velocities. The testing parameters and results can be found in §3.4, while the model fitting procedure is shown in §4.2.

Chapter 3

Experimental results

This Chapter collects the results obtained from the experiments described in Chapter 2 regarding powders characterisation, mixing procedures and compression tests. A detailed overview of each experimental procedure is accompanying the results, as well as a description of the various difficulties experienced during the testing phases. A further objective of this Chapter is to provide a set of fixed and reliable procedures for both uniaxial and diametrical compression tests, to be used in future works regarding wet granular materials. One of the main issues when comparing the results of different works on the compressibility of wet granular materials is, indeed, that there is little agreement between the different preparation and testing techniques, which results in a particular complexity to cross-reference and interpret the results.

The first Section focuses on the characterisation of micro-crystalline cellulose and poly-methyl methacrylate, collecting the results of the QicPic and the optical analysis. The evaluation of the contact angle can be found there, too. The second Section reports the study carried out on the mixing technique, while in the third and fourth Sections it is possible to find the result of the uniaxial and diametrical compression tests, as well as their elaboration.

3.1 Powder Characterisation

As described in previous studies [18, 19] the main powder parameters influencing the strength of wet granular materials are the particle diameter and the contact angle between solid and liquid. In most recent works [8] the effect of particle shape has emerged as one of the most relevant factors, too. An in-depth knowledge of the powder characteristics is thus required for a comprehensive analysis of the mechanisms describing the functioning of the final wet granular material. Furthermore, the understanding of the macroscopic behaviour of the powder can be improved once its microscopic characteristics are known: recurrent single-particle shape irregularities in a sample can, for example, determine a different bulk behaviour from the one observed in different samples. Therefore, an optical analysis was performed to try to capture any particle characteristics that could better explain the overall powder properties of both MCC and PMMA.

3.1.1 QicPic image analysis

As described in §2.2.1, a QicPic SYMPATEC® machine was used to evaluate the profiles of particle size and aspect ratio of the materials used for this study: MCC Cp-102, Cp-203, Cp-305 and Elvacite® 3001.

A small amount of each powder, equal to $5 \pm 1\ g$, was taken from the storage bags and poured in the hopper of the Vibri/L dosing unit. Before collecting the samples, the storage bags were mixed by hand in order to prevent any irregularity in the particle size distribution due to segregation effects. The effect of gravity could, indeed, cause the smaller particles to flow in the voids between the larger ones, causing an accumulation of fines at the bottom of the storage bags and, thus, different profiles of particle size distribution along the height of the storage container. By mixing the powders, any major segregation effect could be considered neglected.

The machine was then switched on and the powder slowly flew, thanks to the vibrating action of the Vibri/L unit, to the Gradis/L gravity dispenser. The particles fell inside the dispensing unit passing in front of the pulsed light source, as described by Figure 2.1.b, while the equipped camera collected the images of the particles projected area. The software connected with the QicPic SYMPATEC® machine was then used to evaluate the profiles of particle size distribution, aspect ratio and circularity of the materials. The QicPic image analysis technique evaluates the projected areas of the particles falling through the pulsed light, calculating the equivalent diameter of the spheres that have the same projected area as the considered particles. The particle size classes are then defined based on the equivalent diameter distribution, and their frequency is evaluated.

A similar methodology is used for aspect ratio and circularity. The aspect ratio is defined as:

$$AR = d_{min}/d_{max} \tag{3.1}$$

where d_{min} and d_{max} are the smallest and the largest diameters orthogonal to each other that can be drawn on the 2D projected figure of the particle considered. A normalized value of AR close to 1 corresponds to a particle whose dimensions are similar to each other, which reflects a projected area with circular shape. The lower the aspect ratio, the more the particle is elongated in one specific direction.

The circularity is defined as:

$$\varphi_c = \left(\frac{circumference\ of\ circle}{perimeter\ of\ projected\ particle}\right)_{fix\ A_p} = \frac{2(\pi \cdot A_p)^{1/2}}{P_p} \tag{3.2}$$

where A_p is the projected area of the particle and P_p is its perimeter. This shape coefficient compares the perimeter of the projected area, easily evaluated by the QicPic software, to the circumference of the circle that has the same projected area as the particle considered. The closer the circularity is to 1, the more the particle is comparable to a sphere.

A combined understanding of particle size distribution, aspect ratio and circularity allows to properly characterise the powders in exam, and provides the particles parameters required for the prediction of granule strength as described in the work of Smith *et al.* [8]. Furthermore, an initial knowledge of the particles shape coefficients provides a more in-depth awareness on how the single particle properties influence the bulk behaviour of the material.

3.1.2 QicPic particle size analysis

The QicPic results on the particle size distribution were collected and displayed graphically, as shown in Figure 3.1, 3.2, 3.3 amd 3.4, both as cumulative and density distributions. The left y-axis reports the cumulative distribution as percentage values: for a given value of particle size x, the corresponding value y indicates which percentage of the analysed particles has an equivalent diameter lower than the size considered. As the particle size increases, more and more particles will be included in the percentage value and, thus, the cumulative distribution will tend to 100%. This representation is particularly useful to identify statistical parameters such as the diameter value below which 50% of the particles can be found, d_{50}, also defined as the median of the distribution.

The right y-axis instead reports the probability distribution in terms of volume, which provides an effective optical representation of the particle size distribution and allows to easily determine the width and the behaviour of the PSD profile, as well as where the main body of particles locates.

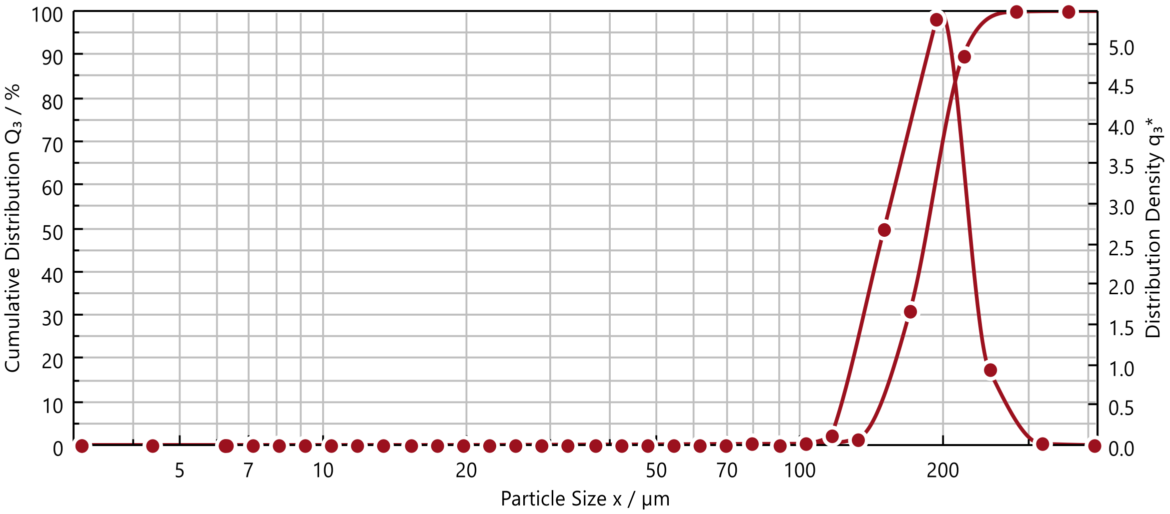

Figure 3.1: *MCC Cp-102 particle size cumulative distribution and distribution density.*

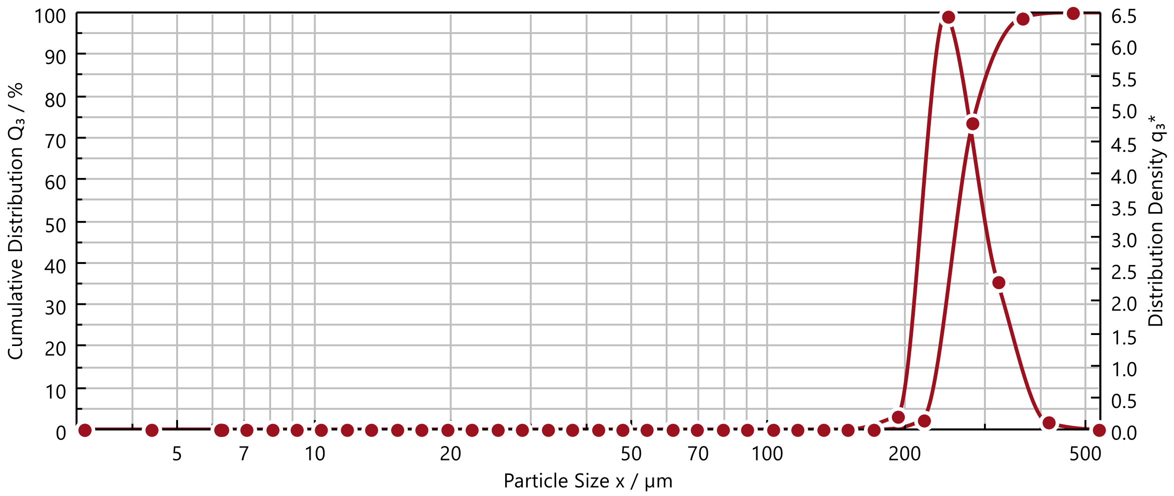

Figure 3.2: *MCC Cp-203 particle size cumulative distribution and distribution density.*

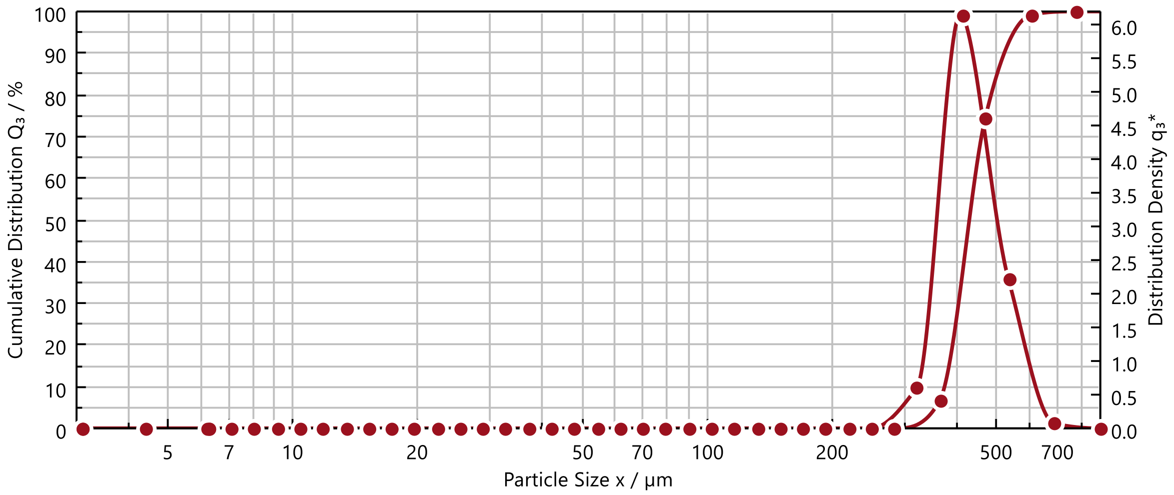

Figure 3.3: *MCC Cp-305 particle size cumulative distribution and distribution density.*

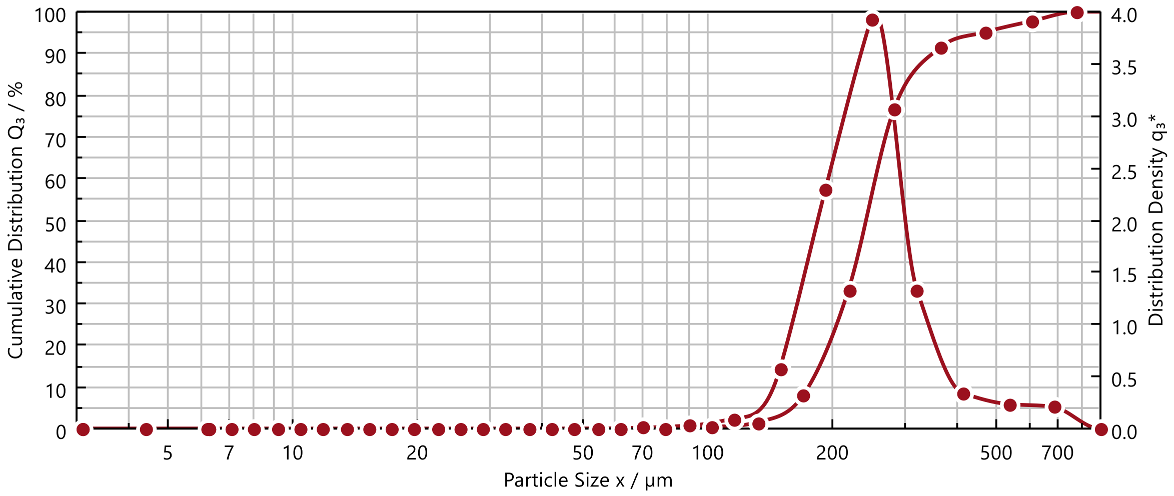

Figure 3.4: *PMMA Elvacite® 3001 particle size cumulative distribution and distribution density.*

The particle size distribution of all the three typologies of micro-crystalline cellulose is particularly narrow and has a single mode, with a sharp peak that increases with the series number of the material. The particle size distribution of PMMA is slightly broader, but the powder still shows a single mode and a defined peak in its profile. Furthermore, all the powders have a "tail" of fines, smaller particles that could be originated from the production methodology or from the attrition and breakage of larger particles during the handling and storage phases. To try to estimate the weight that their presence has on the particle size distribution, further statistical parameters were introduced.

The span of the distribution, defined as φ_D, is a statistical descriptor of the width of the distribution and is defined as:

$$\varphi_D = \frac{d_{90} - d_{10}}{d_{50}} \tag{3.3}$$

where d_{10} is the particle size below which 10% of the particles can be found, and d_{90} is the particle size below which 90% of the particles can be found. A smaller value for the span corresponds to a narrower particle size distribution, and thus allows to evaluate whereas the presence of fines has a relevant effect on the location of the main body of particles.

The values of d_{50}, d_{10}, d_{90} and φ_D can be seen in Table 3.1.

Table 3.1: *Statistical parameters of the particle size distribution obtained with the QicPic machine.*

	d_{10} $[\mu m]$	d_{50} $[\mu m]$	d_{90} $[\mu m]$	φ_D $[-]$
MCC Cp-102	142.82	185.94	222.08	0.426
MCC Cp-203	225.96	261.60	335.69	0.419
MCC Cp-305	369.57	431.67	555.02	0.429
PMMA	174.12	243.59	356.71	0.750

The values of the distribution span are particularly low for all four cases, therefore it was decided to consider the powders as monodispersed and to use d_{50} as average diameter in the evaluation of granule strength carried out in §4.1. The span of the particle size distribution of PMMA is slightly larger, also because of the tail of bigger particles that can be seen in Figure 3.4. The PMMA supplied is, indeed, generally used as an intermediate in the manufacturing of plastic products, therefore there is not a specific requirement for a particularly narrow particle size distribution. On the other hand, MCC is mainly used in pharmaceutical applications which require the particles to have consistent and regular properties, thus a narrower PSD is mandatory for the product to be used. The data regarding the particle size distributions collected by the QicPic machine can be found in Appendix 1.

3.1.3 QicPic particle shape analysis

The image analysis also allowed to obtain the plots of aspect ratio as a function of the particle size, and their profiles are shown in Figure 3.5, 3.6, 3.7 and 3.8. The particle size corresponding to d_{50} is marked with a vertical line, in order to locate the aspect ratio corresponding to the size chosen for the modelling.

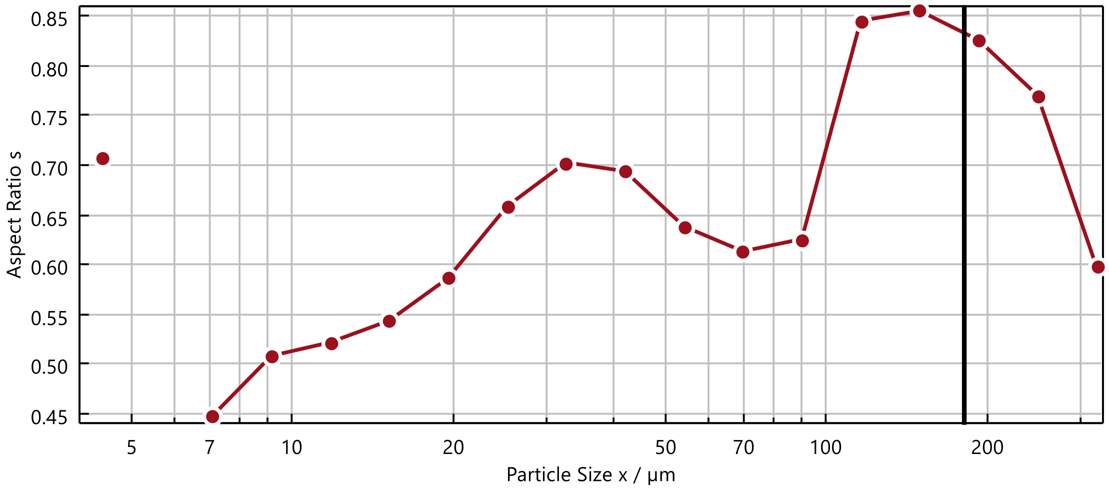

Figure 3.5: *MCC Cp-102 aspect ratio distribution.*

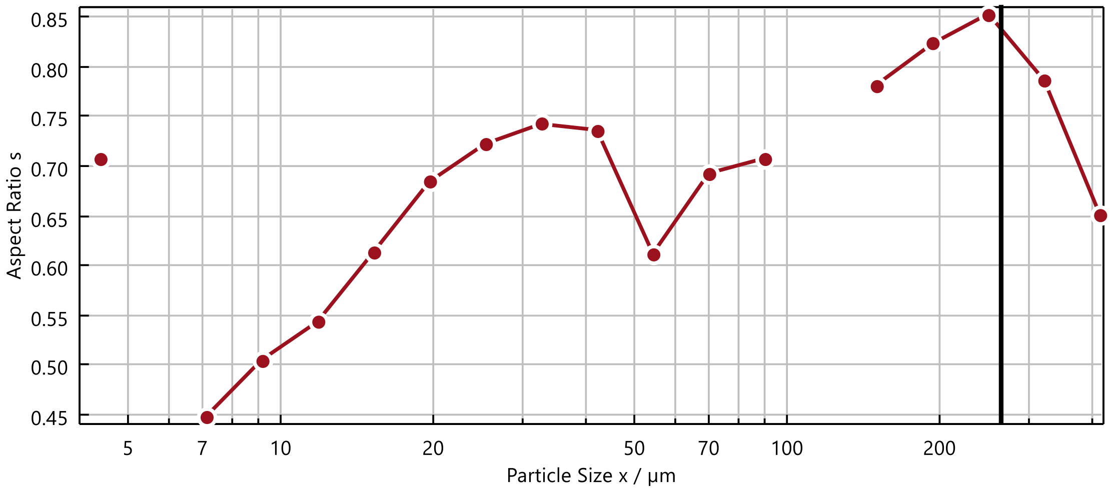

Figure 3.6: *MCC Cp-203 aspect ratio distribution.*

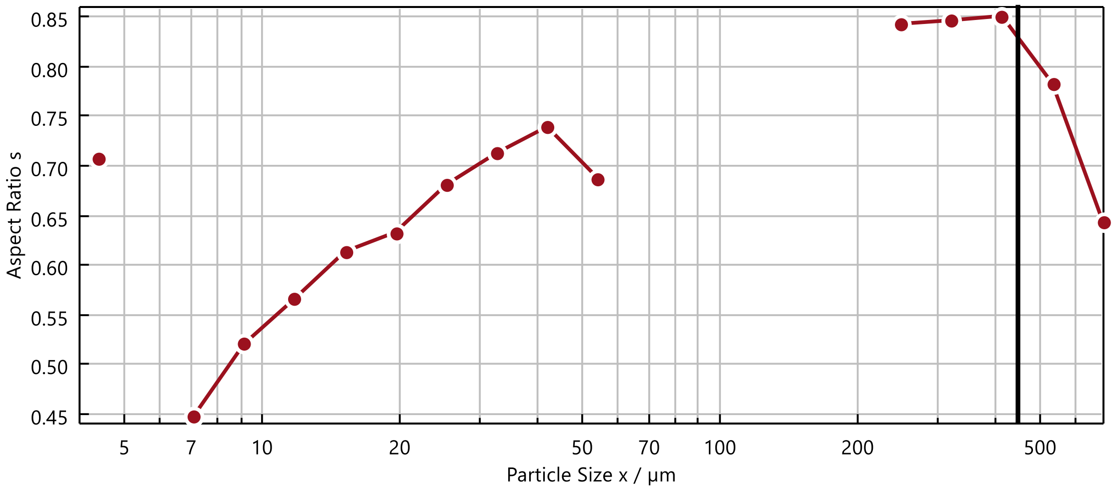

Figure 3.7: *MCC Cp-305 aspect ratio distribution.*

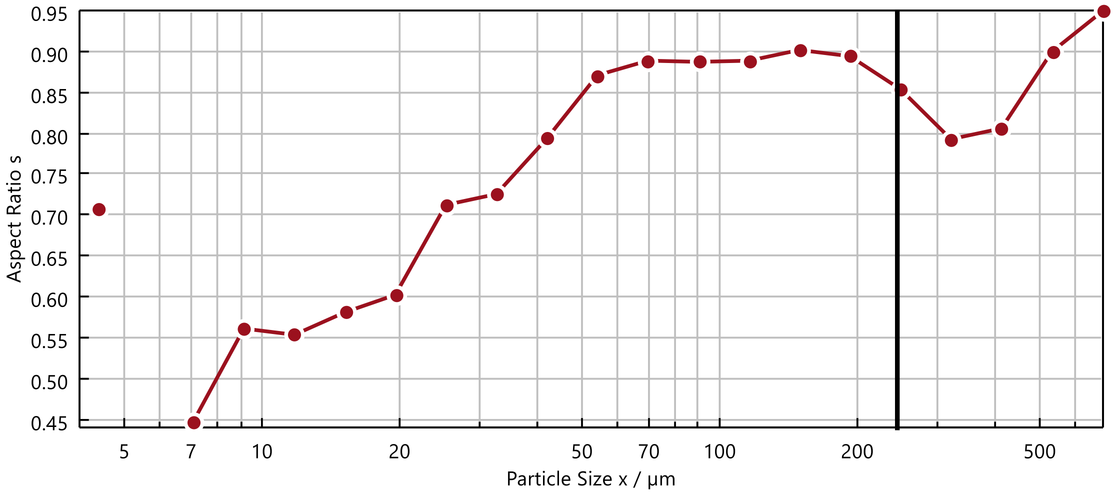

Figure 3.8: *PMMA Elvacite® 3001 aspect ratio distribution.*

The profiles of aspect ratio are different for the four materials, but show generally high values (above 0.8) for the range of particle size of interest. The values of *AR* individuated by the lines are in agreement with the previous knowledge of MCC Celphere™, usually described as an irregular geoid. On the other hand, the profile of the aspect ratio of PMMA Elvacite® 3001 disagrees with the general shape of PMMA powders, generally made of highly regular and spheric plastic beads. In particular, for particle sizes between 250 and 400 micrometers, the value of aspect ratio decreases from 0.9 to 0.8 indicating an increase of irregularities in the particle shape. But knowing that PMMA beads usually have a regular shape, the aspect ratio reduction could be due to the breakage of the spherical particles during the handling and storage phases, and/or to the merging of one or more particle during the production phase. The optical analysis performed in §3.1.4 will help determining whereas this assumption is correct. The values of aspect ratio identified can be seen in Table 3.2:

Table 3.2: *Values of aspect ratio chosen for the modelling, for each material.*

	$\boldsymbol{Aspect\ Ratio}$ $[-]$
MCC Cp-102	0.83
MCC Cp-203	0.84
MCC Cp-305	0.84
PMMA	0.86

Circularity was evaluated with the QicPic image testing, too, and the profiles of circularity versus particle size can be found in Figure 3.9, 3.10, 3.11 and 3.12. The value of d_{50} is marked as well, to identify the corresponding circularity of interest.

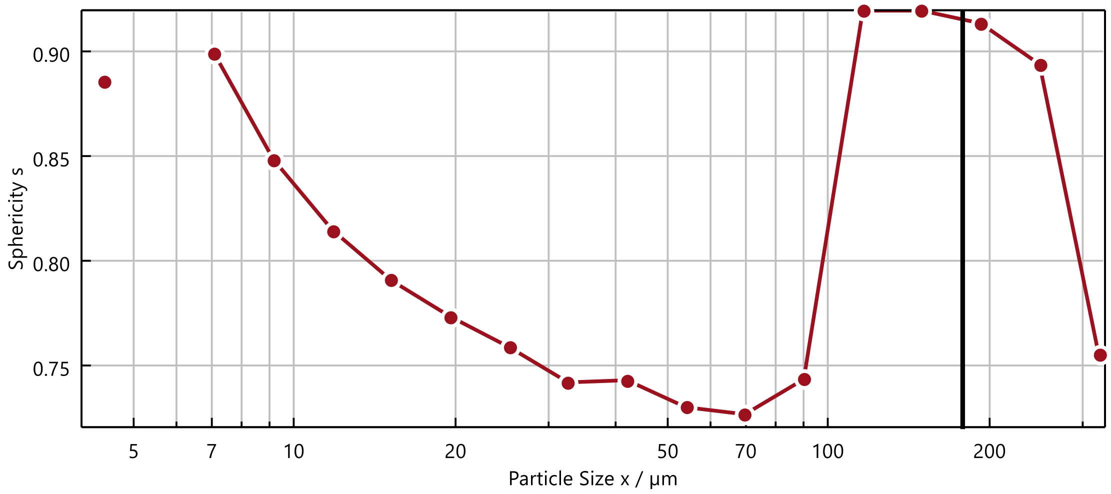

Figure 3.9: *MCC Cp-102 circularity distribution.*

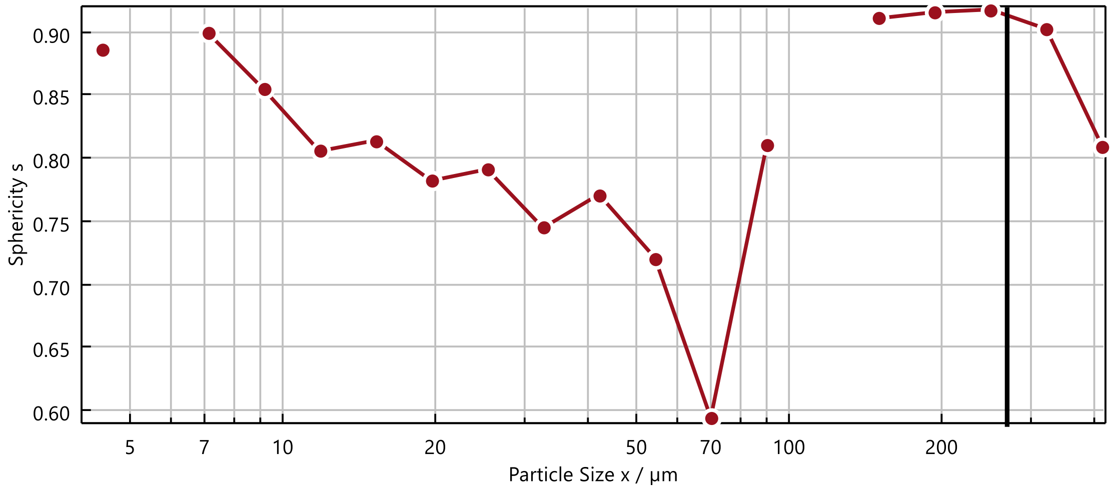

Figure 3.10: *MCC Cp-203 circularity distribution.*

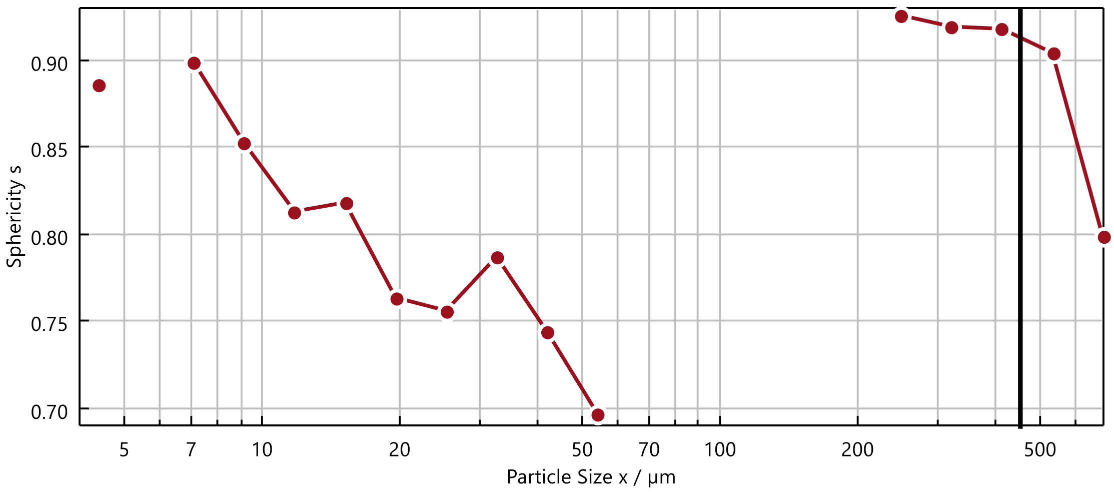

Figure 3.11: *MCC Cp-305 circularity distribution.*

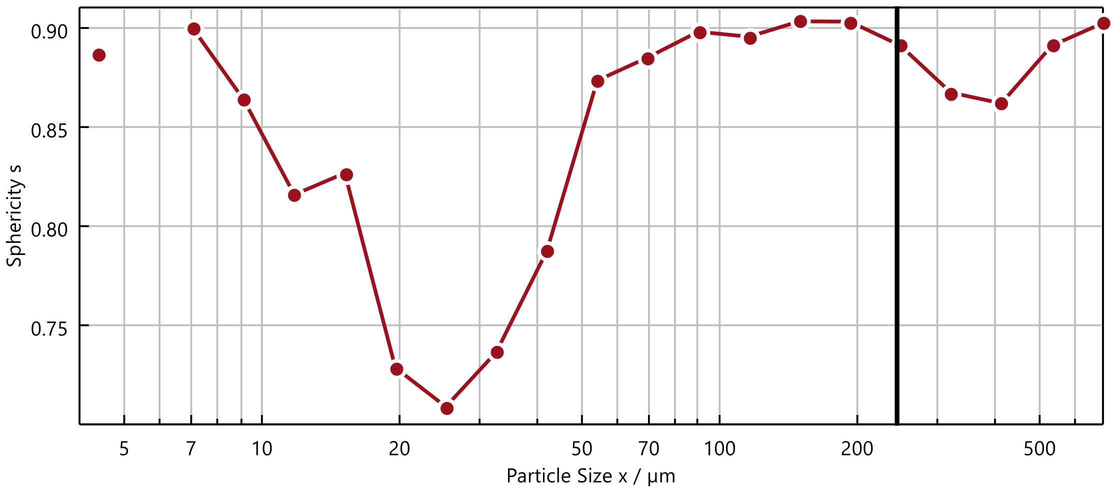

Figure 3.12: *PMMA Elvacite® 3001 circularity distribution.*

As can be seen, the circularity of MCC Celphere™ is particularly high, with values well above 0.90 confirming the already available information regarding the shape of this specific material. PMMA Elvacite® 3001, on the other hand, shows slightly smaller values of circularity for the particle size of interest. This indicates that the perimeter of the particles projected area is fairly larger than the circumference of the circle with the same projected area, meaning that PMMA particles exhibit a more irregular shape than the micro-crystalline cellulose ones. Furthermore, the circularity of PMMA shows the same behaviour as the aspect ratio for particle sizes between 250 and 400 micrometres, enhancing the assumption on the irregularities of the particles. The optical analysis should provide more information regarding this characteristic.

The data regarding the aspect ratio and the circularity distributions collected by the QicPic machine can be found in Appendix 2 and Appendix 3, respectively.

3.1.4 Optical microscope analysis

The knowledge of the powder used during the study was extended by observing the particles through an optical microscope. The information obtained from the QicPic analysis were, indeed, sufficient to further portray the behaviour of the wet granular materials, but unsatisfactory to understand how the single particle characteristics influence the overall bulk behaviour. The optical microscope used is an Olympus DSX500, as described in §2.2.2, and the images were captured for MCC Cp-305 and PMMA. It was assumed that the single particle structures of MCC Cp-102 and Cp-203 are similar to the Cp-305 one, as their production technique is the same and their aspect ratio is comparable, as shown in Table 3.2. Figure 3.13.a and 3.13.b show the images captured for MCC Cp-305, while Figure 3.14.a and 3.14.b show the images captured for PMMA.

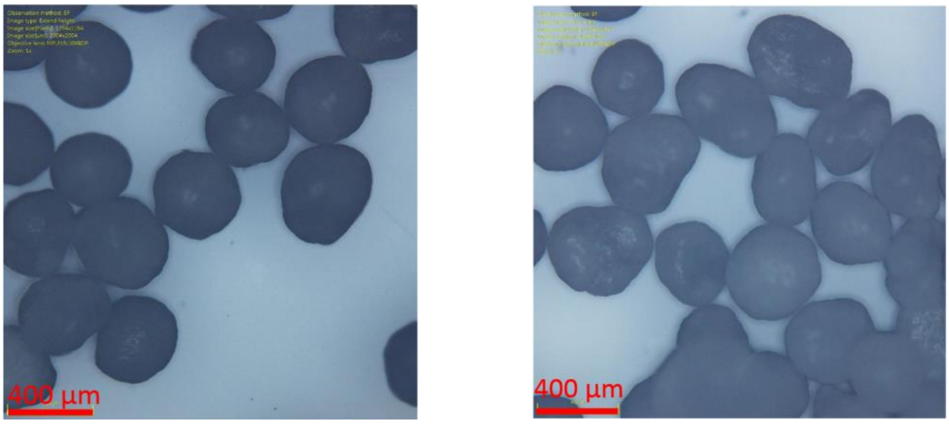

Figure 3.13.a, 3.13.b: *Optical microscope images of MCC Cp-305.*

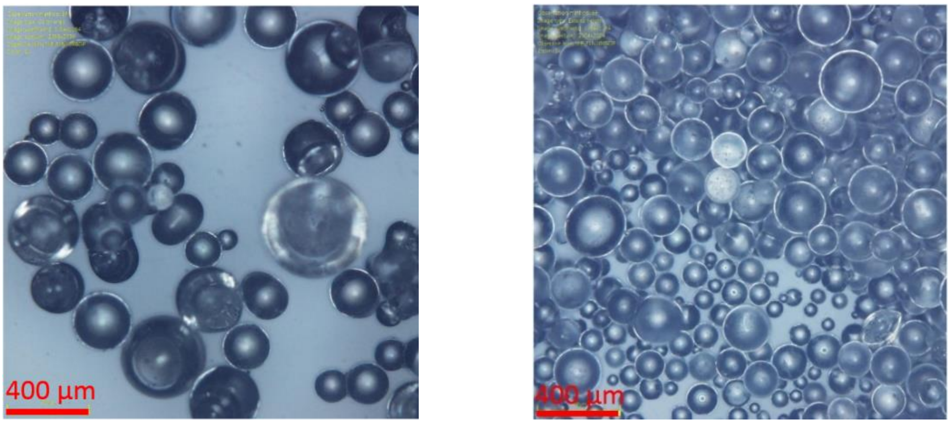

Figure 3.14.a, 3.14.b: *Optical microscope images of PMMA.*

As can be seen from Figure 3.13.a and 3.13.b, the shape of MCC Celphere™ is similar to a geoid, with various elongation levels. The surface looks generally smooth, with small irregularities but without any major fractures nor cracks. Furthermore there are no particles merged together, thus the aspect ratio evaluated in §3.1.3 can be assumed to correspond directly representative of the single particles.

On the other hand, PMMA particles show a wide range of shapes and behaviours. The baseline shape is spherical, as can clearly be seen in Figure $3.14.a$ and $3.14.b$, but in many cases two or more particles are merged together forming irregular structures. Furthermore, some particles look as if the external surface had been damaged, showing an irregular internal structure. Figure $3.15.a$ and $3.15.b$ show two details of irregular particles from Figure 3.14.1.

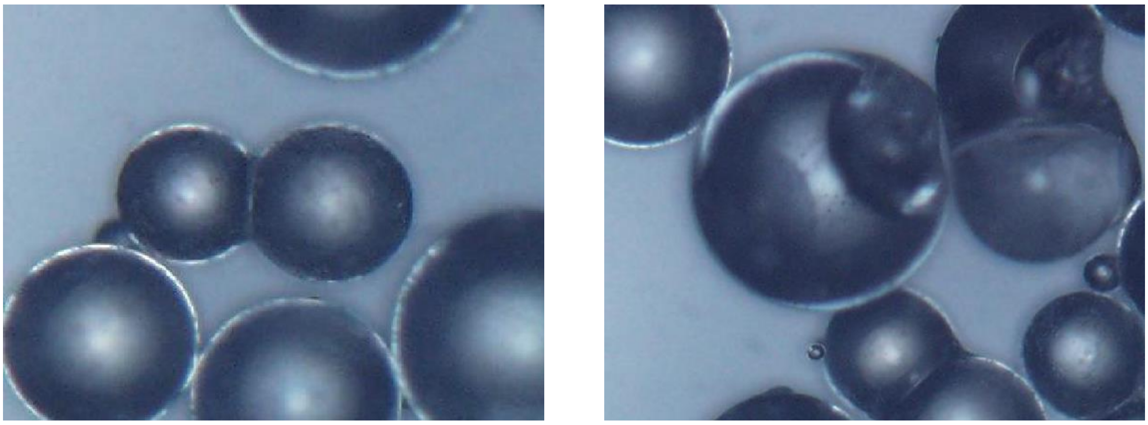

Figure 3.15.a, 3.15.b: *Details of two merged particles (a) and of particles with irregular surface (b) for a PMMA Elvacite® sample.*

Particles such as the ones shown in Figure $3.15.a$ and $3.15.b$, when passing in front of the pulsed light of the QicPic, generate an irregular projected area whose aspect ratio is lower than the one of a single, regular particle, in particular for merged ones. Therefore, the overall aspect ratio of the powder is by far lower than the expected value, which would be particularly close to 1 if there were no merged particles. These defects at single-particle level could be due to the production process, in which two or more PMMA beads could merge together due to high temperatures. If the bound then breaks during the handling or storage phases, the particles may show an irregular surface where they were previously merged. Furthermore, the nature of the surface fractures could have specific effects on the wettability and the buoyancy of the plastic beads, and therefore could influence the values of contact angle in case some air gets stuck in the cracks.

Nevertheless, the most interesting result is that PMMA beads, generally considered as spherical particles with high aspect ratio and circularity, can often show irregular shapes and complex structures that may determine a by far different behaviour from the predicted one. Furthermore, as different production processes employ different operating conditions, the aspect ratio should always be measured for each single batch tested in order to prevent erroneous assumptions of its value. For this study all the samples were taken from the same bag of material, thus it is possible to safely assume that the value of aspect ratio is constant for all the wet granular samples prepared.

This said, the irregular particles are just a fraction of the overall bulk, which is mainly formed by regular beads. Therefore, a close-up image was taken of the surface of a single plastic bead, as shown in Figure 3.16.

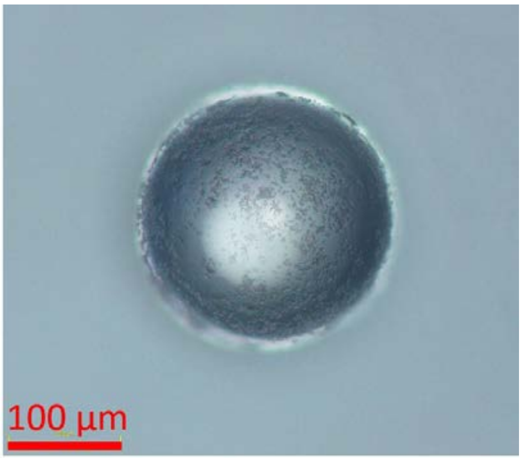

Figure 3.16: *Detail of the surface of a single PMMA bead.*

The bead surface looks smooth and regular, with small imperfections. The aspect ratio, equal to 0.98, is particularly high and in agreement with the previous knowledge of single poly-methyl methacrylate beads. This observation also confirms the assumption for which the merged and broken PMMA particles largely reduce the average aspect ratio of the powder, which would otherwise be close to 1. As regards the characteristics of broken particles, more images were captured during the SEM analysis of §3.1.5.

3.1.5 SEM analysis

A Jeol JSM-7100 F scanning electron microscope was used to capture detailed images of the surfaces of the powders, as described in §2.2.2. Figure $3.17.a$ to $3.17.f$ show the pictures captured for MCC Celphere™ Cp-102 and Cp-305 at different magnification. The white bar corresponds to a length of 100 micrometers.

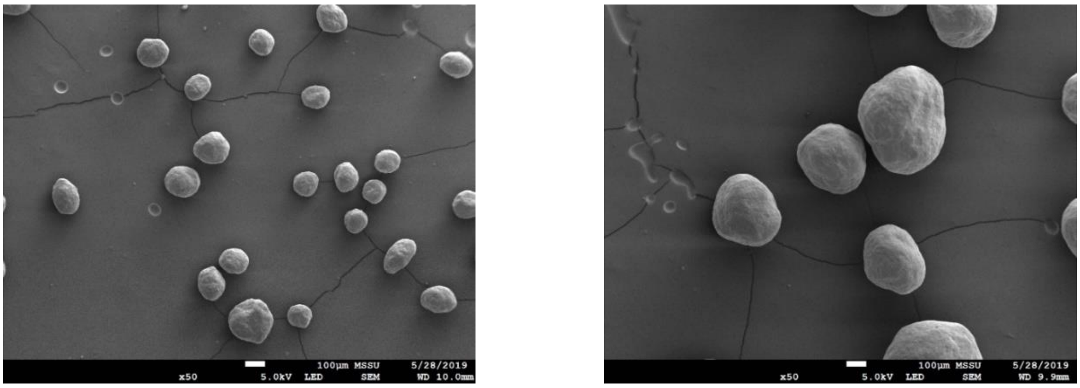

Figure 3.17.a, 3.17.b: *Images of MCC CP-102 (a) and Cp-305 (b) at x50 magnification.*

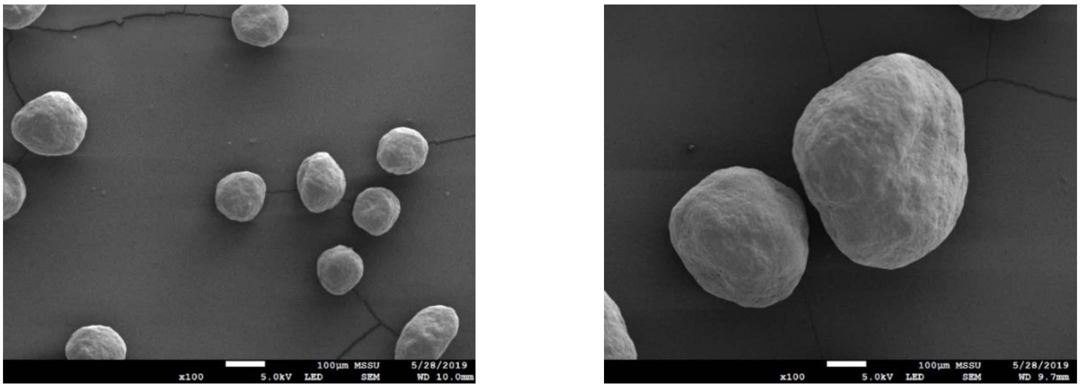

Figure 3.17.c, 3.17.d: *Images of MCC CP-102 (a) and Cp-305 (b) at x100 magnification.*

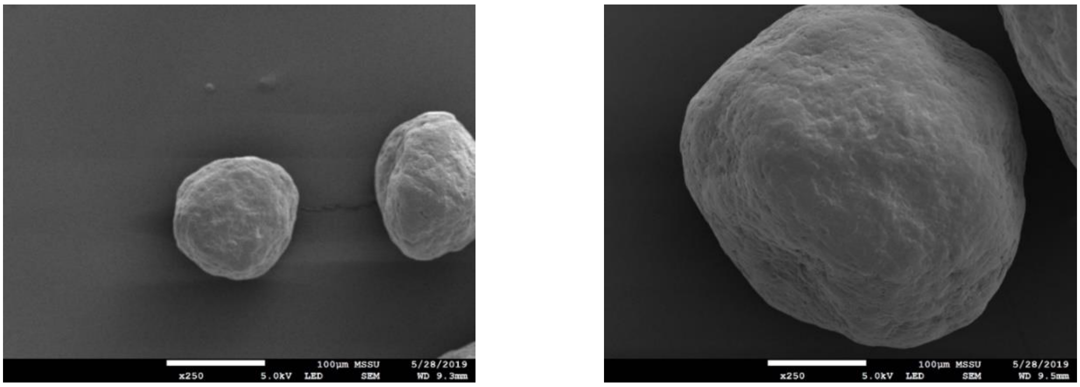

Figure 3.17.e, 3.17.f: *Images of MCC CP-102 (a) and Cp-305 (b) at x250 magnification.*

The images captured with the SEM confirm the initial observations of the optical microscope. The MCC Celphere™ particles have a geoid shape, with smooth and slightly irregular surfaces, similar to polished rocks. The particle morphology is therefore different from the one of more common MCC APIs, such as MCC PH-102, which present a prism morphology [46]. Furthermore, no merged particles were found in the tested sample: it can be safely assumed that the aspect ratio and the circularity measured for MCC correspond to the single particles.

The analysis of PMMA beads was particularly important as its characteristics could partially explain the behaviour of the powder during the other testing phases, such as in the contact angle measurement. Figure $3.18.a$ and $3.18.b$ show two sets of particles with a $x50$ magnification, while Figure $3.18.c$ and Figure $3.18.d$ show regular PMMA beads at $x100$ and $x250$ magnification.

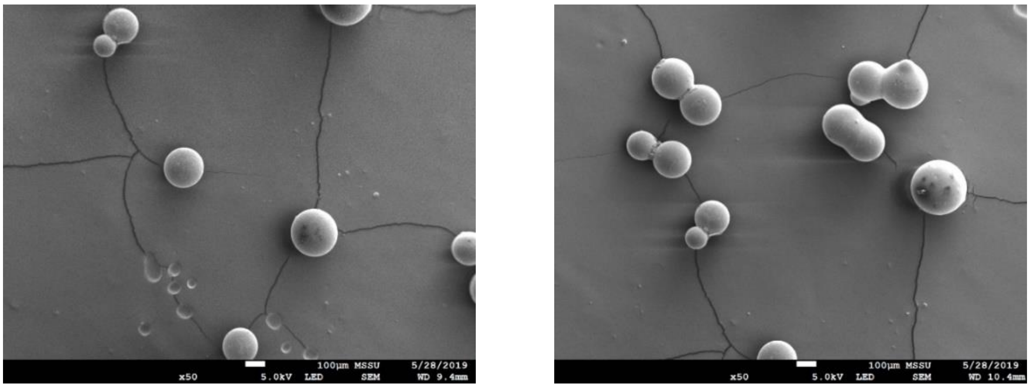

Figure 3.18.a, 3.18.b: *Images of PMMA Elvacite® 3001 at x50 magnification.*

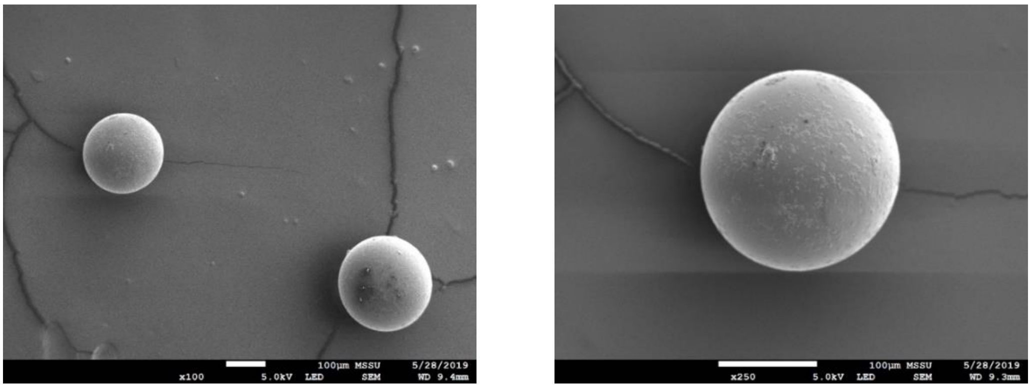

Figure 3.18.c, 3.18.d: *Images of PMMA Elvacite® 3001 at x100 (a) and x250 (b) magnification.*

The SEM images confirm the assumption of §3.1.4: the plastic particles are spherical, with regular shapes and small imperfections on their smooth surface. Some of them are merged together, with different levels of overlapping. Figure $3.19.a$ and $3.19.b$ show two details of different particle bounds.

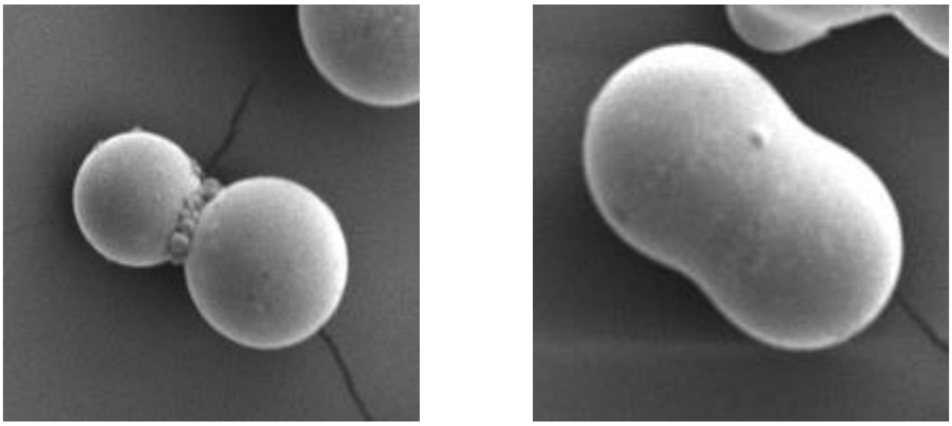

Figure 3.19.a, 3.19.b: *Two different typologies of particle bounding: bounding through small particles interaction (a) and almost total merging (b).*

The two different typologies of particle bounding could depend on the operating conditions of the production process, especially as regards the high merging level ones. An interesting information noticeable from Figure $3.19.a$ is that many fine particles could be released whenever the particle bound breaks due to external forces. Therefore, any application that implies high stresses applied to PMMA beads should take into account the possibility of having an increase in the presence of fines.

Another objective of the SEM analysis was to better understand the characteristics of particle breakage for the plastic beads. Figure $3.20.a$ and $3.20.b$ show two broken particles.

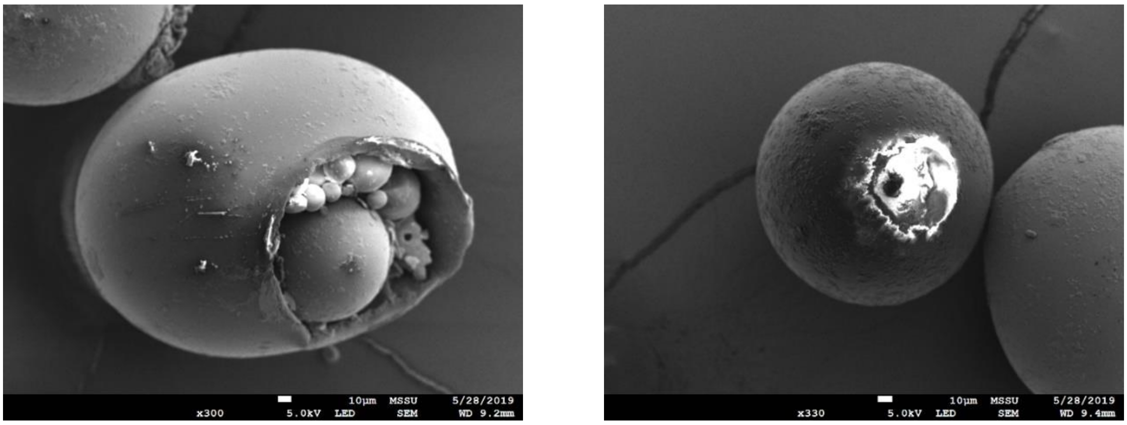

Figure 3.20.a, 3.20.b: *Two different broken PMMA beads.*

From the two images it can be seen how smaller plastic structures are locked inside the external bead shell. In Figure $3.20.a$, in particular, it seems that the particle was previously linked to another one and that the breakage of the bound revealed its internal structure. The internal network is highly intricate, with beads of different size and shape and plastic tendrils partially filling the void space inside the shell. This porous internal structure could give some difficulties when measuring the contact angles with the technique described in §2.2.3, as air could get stuck inside the voids modifying the buoyancy of the particle in liquids. Furthermore, depending on the production technique, some gasses could be stuck even inside intact particles and modify the physical properties of the particle, such as its bulk density.

For the sake of this study the damaged particles were not considered relevant for the overall powder behaviour, therefore the data regarding particle size distribution and aspect ratio distribution of §3.1.2 and §3.1.3 were used for the experimental and the modelling phases. However, particular care was taken in the evaluation of the contact angle for the PMMA-silicone oil system as broken particles testing could yield inconsistent data.

3.1.6 Contact angle measurement

The experiments for the evaluation of the contact angles were performed using a FTA1000 B-Class Drop Shape Analyser, with the methodology described in §2.2.3. For MCC Cp-305, the choice of the particles to use was simple as their shape is generally regular and their PSD is particularly narrow. But knowing the complex shape of PMMA particles and their common irregularities, it was required to select large and regular particles one by one, using the optical microscope view to check their shape before positioning them on the silicone oil surface. In this way merged systems and clearly broken particles were avoided, improving the quality of the data collected by the test.

For the liquid choice, the 500 cSt silicone oil (with dynamic viscosity of 0.485 Pa*s) was selected and it was assumed that the value of contact angle would not change with viscosity. This assumption is especially effective from an experimental point of view, as measuring the contact angle for the 30000 cSt silicone oil could give problems related to its high viscosity: the particles would require, indeed, by far longer time to sink in the oil whereas the contact angle was equal to zero, or may even not be able to move due to the particularly high viscosity. Furthermore, as described in previous works [40] the surface energy of silicone oils is generally low and there is no reason to assume the existence of a remarkable difference between the contact angles of the two liquids.

The single particles were then carefully deposited on the surface of the oil, and their behaviour was captured over time. The test was repeated 5 times for each material: Figure $3.21.a$, $3.21.b$ and $3.21.c$ show three different frames of the behaviour of a MCC Cp-305 particle. The gray area corresponds to the liquid bulk, while the black area at the top of the image is the liquid-air surface.

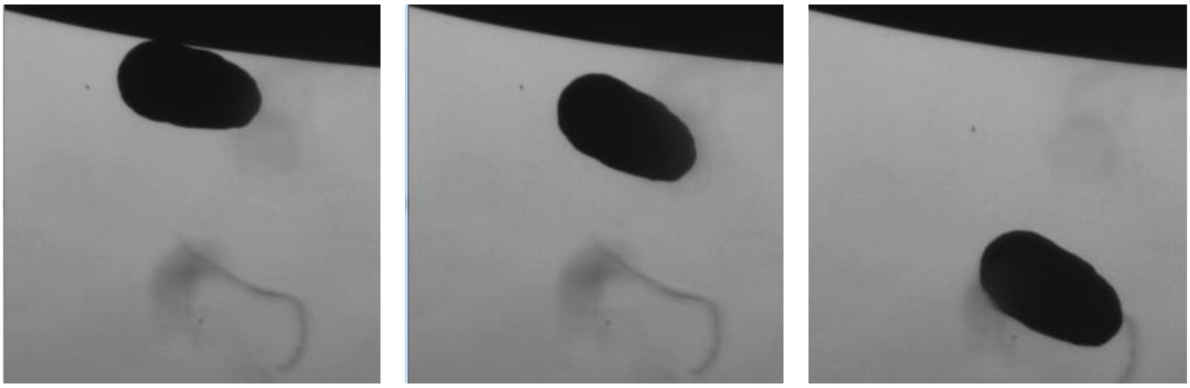

Figure 3.21.a, 3.21.b, 3.21.c: *Three frames of the behaviour of a MCC Cp-305 particle in 500 cSt silicone oil, after 8 seconds from the deposit (a), after 12 seconds (b) and after 16 seconds (c).*

All the MCC Cp-305 particles sank in less than one minute after they had been deposited on the surface. It is thus possible to assume that the contact angle between micro-crystalline cellulose and silicone oil is equal to zero.

Regarding PMMA, the contact angle measurement gave various difficulties related to the particle shape as discussed in §3.1.5. Many of the particle tested were indeed floating closed to the surface, but at a closer look shown fractures similar to the ones in Figure $3.20.a$. This behaviour could be due to the presence of air stuck in the internal porous structure of the particle, reducing the particle density and thus allowing it to float. Therefore, it was decided to do not consider these tests and only focus on regular, spherical particles.

All the spherical particles observed sank in the silicone oil, at different velocities. It can be deducted that this phenomenon is related to the internal porosity, different for each particle, which causes them to sink with different dynamics. Figure $3.22.a$ and $3.22.b$ show two PMMA particles sinking 10 seconds after their positioning on the binder surface.

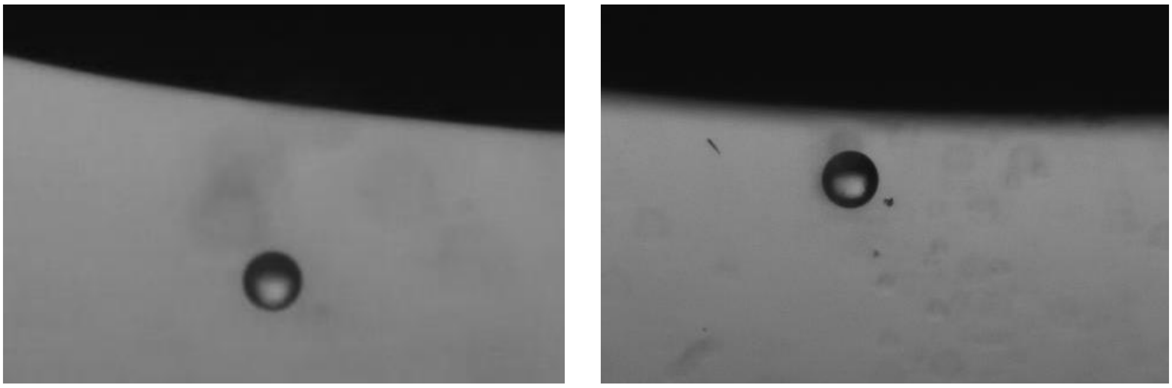

Figure 3.22.a, 3.22.b: *PMMA particles sinking in 500 cSt silicone oil at different velocities.*

As the regular particles sank in the liquid, it was assumed that the contact angle between PMMA and silicone oil is equal to zero, too.

Nevertheless, it should be noticed that more techniques could have been used to determine the contact angle between the powders and the liquids considered [47]. But in the study of wet granule strength just the cosine of the contact angle is considered: even if its value was finite and different from zero, its different impact on the material behaviour would be negligible as the value of the cosine would still be close to 1. Therefore, the results obtained in this section can be assumed as consistent with the objectives of the study.

3.2 Sample preparation

The standardisation of the sample preparation and testing phases was one of the main objectives of this study, as previously described in §2.2.4 and §2.2.5. The choice of the Turbula® shake mixer had to be experimentally analysed in order to confirm its capability of supplying samples with consistent physical properties. The optimal operative parameters have been determined assessing the samples both by eye and by dynamic testing during an initial exploration phase, while particular care was taken in controlling the quality of each batch prepared.

3.2.1 Batch preparation

The containers used to prepare the wet granular samples were LDPE bottles supplied by Fisher Scientific (Bishop Meadow Road, Loughborough, Leicestershire, LE11 5RG) with a volume of 1 litre. They were chosen because of the wide opening, which made it easier to empty and clear them after their usage, as well as facilitating the withdrawal of the material for the tests.

The bottles were filled with the powder up to around 40% of their total height, and the material was weighted. An amount of liquid binder equal to 6% w/w was slowly poured inside the bottle, trying to avoid the formation of a single well. This procedure was particularly complex with the 30000 cSt silicone oil as the liquid tended to form a single, large lump that remained on the surface of the powder bulk. To ease the binder dispersion the silicone oil was added in different stages, in between which the bottle was quickly mixed by hand: in this way smaller liquid lumps formed in the powder bulk, facilitating the successive dispersion of the binder.

Initially the amount of liquid binder used was 10% w/w, similar to many previous works [8, 19, 30, 31], but this content gave many difficulties during the testing of both MCC and PMMA. The samples indeed appeared to be particularly wet and, during the sleeve removal phase of the AUPT testing, several particles stuck to the sleeve surface and moved upwards with it. This caused the sleeve to often get stuck halfway through the piston, so that the test had to be aborted and repeated. And even when the sleeve was able to be fully repositioned, a remarkable amount of material had still been removed from the external surface of the cylindrical sample, making the test unreliable. Therefore, it was decided to operate with a slightly lower amount of binder, equal to 6% w/w, which did not cause any problem during the sleeve removal. This value was kept constant for all the samples tested both uniaxially and diametrically.

3.2.2 Mixing parameters evaluation

The homogeneity of the wet granular material was one of the most important characteristics to check before proceeding with any test of granule strength. In the case of a poorly distributed liquid binder, indeed, the values of granule strength could be similar to the strength of the dry powder (in binder-poor regions) or comparable with a highly wetted granular material (in binder-rich regions). Furthermore, it can be assumed that if even one single portion of the cylindrical samples presents a weaker structure due to the different liquid content, during the compression tests the sample will fail along this zone and provide a non-representative value of the material strength.

Taking into account this mechanism, two levels of mixing control were defined to search for the optimal operative parameters: each sample had first to be visually inspected, to verify that no evident binder lumps were present, and then had to be tested with the AUPT machine and compared to other batches. Furthermore, from each batch two samples were taken, one from the upper layer wet granular material and one as close to the bottom as possible. In this way any internal flow pattern that caused an irregular distribution of the binder could be registered and considered in the final evaluation.

The mixing test was repeated for three batches of MCC Cp-102 and 500 cSt silicone oil. This combination was chosen as the two materials were the first ones to be available in the laboratory, but the visual verification of homogeneity was performed for all the batches prepared, regardless of the materials. Mixing speed was chosen at a medium-high velocity of 72 rpm, sufficiently high to grant a high recirculation and cause the larger liquid lumps to deform and break when impacting against the wall of the container. The batches were then prepared, pouring the same amount of powder in each of them and adding the corresponding amount of binder. The samples were then mixed with the Turbula® shake mixer, and periodically examined to check for the presence of liquid lumps. Table 3.3 collects the observations for the three batches.

Table 3.3: *Presence of liquid lumps at visual inspection for the three batches of MCC Cp-102+500 cSt silicone oil analysed, as a function of the mixing time.*

Mixing time	Batch #1	Batch #2	Batch #3
5 min	Yes	Yes	Yes
10 min	Yes	Yes	Yes
15 min	Yes	No	No
20 min	No	No	No
25 min	No	No	No

A mixing time of 20 minutes is sufficient to avoid the presence of observable liquid lumps in all the three samples considered for the test. Furthermore, in all the other samples using 500 cSt silicone oil the same result was observed for 20 minutes of mixing time.

From each batch, two samples were taken as previously described and analysed with the AUPT machine. The tests were performed using the same testing parameters, shown in Table 3.4.

Table 3.4: *Testing parameters used for the assessment of the mixing homogeneity.*

	Value
Pre-consolidation stress [kPa]	5
Consolidation stress [kPa]	20
Sample height [mm]	56
Failure speed [mm/s]	5

The results can be seen in Figure 3.23.a and the experimental data can be found in Appendix 4.

Figure 3.23.a: *Uniaxial failure stress for the three batches of MCC Cp-102+500 cSt silicone oil tested, comparing the results of the upper layer and of the lower layer.*

The values of failure stress of the different samples agree in an interval of $\pm 2\sigma$, therefore the mixing technique was considered consistent and reliable at obtaining well mixed wet granular materials. Furthermore, no major difference could be noticed between the different sections of the bottles, meaning that there are no relevant segregation effects during the mixing phase.

Once the 30000 cSt silicone oil was available in the laboratory, the mixing technique was assessed again to determine its capability to deal with the distribution of a by far more viscous liquid. Three batches were prepared and mixed at 72 rpm, checking the existence of liquid lumps at different mixing times. The observations are shown in Table 3.5.

Table 3.5: *Presence of liquid lumps at visual inspection for the three batches of MCC Cp-102+30000 cSt silicone oil analysed, as a function of the mixing time.*

Mixing time	Batch #1	Batch #2	Batch #3
5 min	Yes	Yes	Yes
10 min	Yes	Yes	Yes
15 min	Yes	Yes	Yes
20 min	Yes	Yes	Yes

All the samples shown the existence of liquid lumps after the mixing time chosen for the 500 cSt silicone oil. The high viscosity silicone oil indeed formed a small number of liquid-rich granules, too strong to deform and squeeze the binder out during the impact with the container walls. Additionally, the bottle structure and the high viscosity did not allow for a large initial distribution of the binder droplets: the binder was so viscous that it had to be drawn from its storage container with a metal spatula and slowly poured inside the bottle, slightly penetrating in the powder surface and forming large wet structures.

Therefore, it was decided to proceed with a different approach. After the 20 minutes mixing time, the large liquid lumps were broken with a metal spatula and further dispersed in the powder bulk. The samples were then mixed for other 20 minutes at 72 rpm and visually inspected. Out of the three samples no liquid lump could be found, and the wet granular material exhibited a smooth and regular structure. Two samples from each bottle were then tested with the AUPT machine using the same parameters of Table 3.4. The results can be found in Figure $3.23.b$, while the experimental data can be found in Appendix 4.

Figure 3.23.b: *Uniaxial failure stress for the three batches of MCC Cp-102+30000 cSt silicone oil tested, comparing the results of the upper layer and of the lower layer.*

In this case, too, the results of failure stress of the different samples agree in an interval of $\pm 2\sigma$. The mixing methodology was considered as effective and implemented for the preparation of all the wet granular material samples containing the high viscosity silicone oil. Furthermore, all the subsequent samples were visually inspected before the testing phases: out of over 15 samples prepared with the high viscosity binder, just 2 shown the presence of liquid lumps after the double mixing module. Both samples were made with MCC Cp-102 powders, which gave particularly strong granules that barely deformed during the mixing phase. In both cases the lumps were broken again with a metal spatula, dispersed in the power bulk and the samples were mixed for one more mixing module, obtaining a homogeneous sample.

Apart from these two exceptions, the mixing methodology defined in this section proved to be effective for a wide range of batch preparations, providing over 30 batches of wet granular material with regular properties and similar structure. Furthermore, the methodology is quick and can be easily run while working on other experiments, and does not require long cleaning phases as for other equipment. It is particularly suggested for low density binders, as the ones used in this study, while high viscosity liquids ($\mu > 10^2$ Pa*s) may require different techniques.

3.3 Uniaxial testing

The wet granular materials prepared with the Turbula® mixer were visually inspected and tested with the *Advanced Uniaxial Powder Tester*, or AUPT, produced by Freeman Technology (Tewkesbury Business Park, Miller Court, Severn Dr, Tewkesbury GL20 8DN). The main objective of this testing procedure was to determine how the peak failure stress, which is defined as the maximum stress it can sustain before failing, changes as a function of solid, liquid and testing parameters. The results here presented were then used to validate the model shown in §4.1.

3.3.1 Data collection preparation

The data collection phase required to define a quick and consistent methodology for the preparation, collection and organization of the results. All the previous works [8, 18, 31] indeed collected data varying the binder characteristics (viscosity and surface tension), the particle characteristics (particle size and shape, contact angle with the binder) and the failure velocity, while this study introduced the effect of the consolidation stress as a further parameter to consider. This choice required to largely increase the amount of experimental points to collect, as each set of consolidation stresses needed a sufficient amount of experimental data to be properly represented during the model validation. An initial analysis on the main testing parameters was performed, to better define the operating conditions.

3.3.1.1 Consolidation stress

It was decided to fully utilise the range of consolidation stresses available with the AUPT machine, choosing to operate at $20, 40, 60, 80$ and 100 kPa of consolidation. Higher values could be reached working with an Instron® machine, but the testing time would have been too long if compared with the length of this study. Some initial tests were also carried out at lower consolidation stresses, such as 5 and 10 kPa, but the samples gave stability issues and tended to fail during the sleeve removal phase.

The machine also allowed to set the pre-consolidation stress, an initial stress to apply to the cylinder in order to partially compressing it before proceeding with the double-ended consolidation. Its effect is to give a preliminary shape to the cylinder, slightly compressing the material to make it more uniform during the double-ended consolidation. While pouring the material in the cylinder sleeve, indeed, the irregular structure of the wet granular mass leaves voids that may affect its behaviour during the double-ended consolidation: applying a pre-consolidation stress reduces the volume of these voids and prepares the sample for the proper consolidation, without influencing its final behaviour. It was decided to apply a pre-consolidation stress equal to $20-25\%$ of the main consolidation stress, as suggested in the user manual.

3.3.1.2 Deformation velocity

As regards the piston velocity, two parameters had to be set: the consolidation speed and the deformation/failure speed. The consolidation speed is the velocity with which the wet granular material is consolidated, and its effect on the final granule strength was considered as negligible. An intermediate value equal to 0.5 mm/s was selected, granting low testing times and a good accuracy in the evaluation of the consolidation stress. Higher velocities could indeed cause the sample to get compressed above the set value before the system was able to block the piston.

On the other hand the failure speed has a predominant effect on the peak failure stress of the wet granular material, as described in §1.3. Its value is used for the evaluation of the strain rate, seen as the ratio between deformation velocity and sample height, which is then used to evaluate the capillary number. As the objective of the study is to evaluate the granule strength in a wide range of capillary number, in particular focusing on the highest reachable values of Ca, the deformation speed was varied between 0.01 mm/s up to 5 mm/s (which upper limit of the machine). In this way it was possible to span the value of Ca from 10^{-7} to 10^{-2}, and to capture the granule behaviour over a wide range of operating conditions. Figure 3.24 shows the test settings panel available in the software interface.

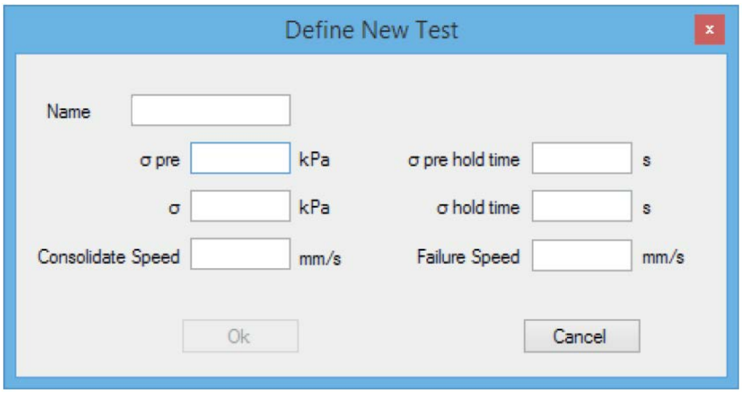

Figure 3.24: *Test settings panel for the AUPT testing.*

The failure speeds were chosen trying to obtain a wide set of data, using $0.05, 1, 2$ and 5 mm/s as reference values. More values were used for PMMA, to better capture its behaviour during the model validation phase, and for MCC Cp-102, as it was the first material tested and was used to improve the expertise with the equipment.

It should be noticed that in previous works values of deformation speed up to 150 mm/s were reached, using specific Instron® machines designed for high speed testing. This allowed to evaluate the granule strength at capillary numbers up to 10^{1}, therefore capturing the change in behaviour that wet granular materials show at Ca equal to 10^{-3}. Unluckily the AUPT does not allow to work at such high deformation velocities, but the choice of a 30000 cSt silicone oil still ensures the representation of the full range of behaviours described in §1.3.

3.3.1.3 Sample height

The AUPT machine allows to choose between three possible cylinder sleeve positions during the testing, enabling to work with three different height to diameter ratio (H/D) for the initial sample. Figure 3.25 shows a picture of the possible sleeve settings, with the corresponding height of the cylindrical sample.

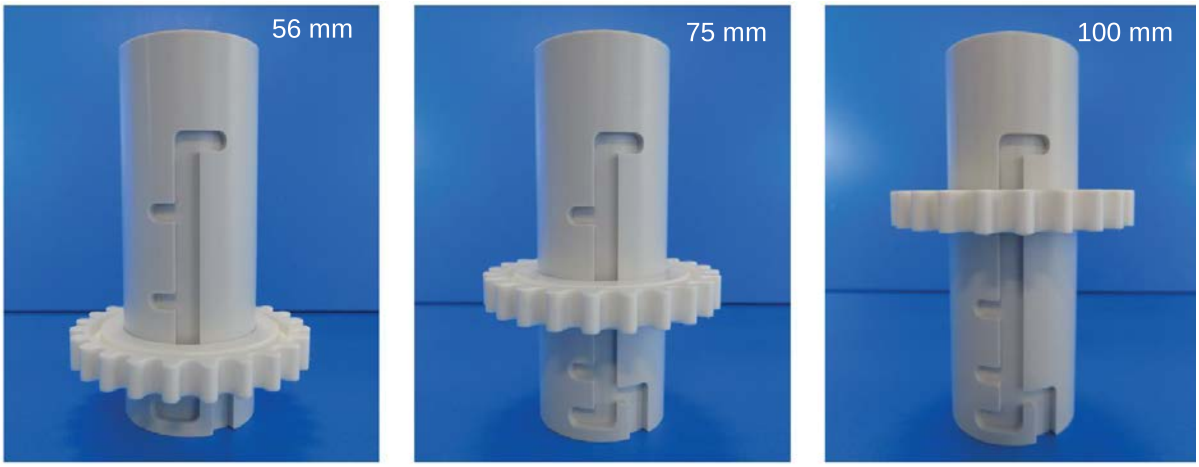

Figure 3.25: *Representation of the three possible positions for the sleeve support.*

The three different positions correspond to three different initial heights for the powder sample. It should be noticed that, during the pre-consolidation and the consolidation phases, the effective height of the wet granular sample decreases as an effect of the compression. The height to diameter ratio, therefore, decreases to values that depend both on the consolidation stresses and on the granular system parameters, such as its own porosity and compressibility. Furthermore, any structural void created while pouring the material in the support sleeve causes the final H/D to decrease accordingly.

The effect of the choice of the sample height is, therefore, largely influenced by material characteristics and random mechanisms. During the experimental exploration of the dynamic strength, the lower sleeve support position was initially used for most of the tests with the low-viscosity binder. This choice was due to the small amounts of powder initially available in the laboratory, and to reduce the overall materials waste.

Nevertheless, the piston of the AUPT machine was designed to be able to compress samples only until their H/D ratio is higher than 1, and to block the test whenever a lower value was reached. Therefore, when testing wet granular materials at high consolidation stresses, it often happened to reach the critical value of H/D and to have to repeat the test. It was then decided to avoid this issue by using the middle sleeve support position, for which critical ratio was never reached.

In order to check if the sample height had any influence on the peak failure strength of the wet granular samples, experimental data was collected with the AUPT machine for different samples of MCC Cp-102 and 500 cSt silicone oil. The data was collected at low capillary numbers in order to obtain the flat dependency between peak failure stress σ_c and capillary number Ca observed by Iveson *et al.* [18] and, therefore, easily compare the results. Different samples were tested at 40 and 100 kPa and at low deformation velocities, and the results can be seen in Figure 3.26.

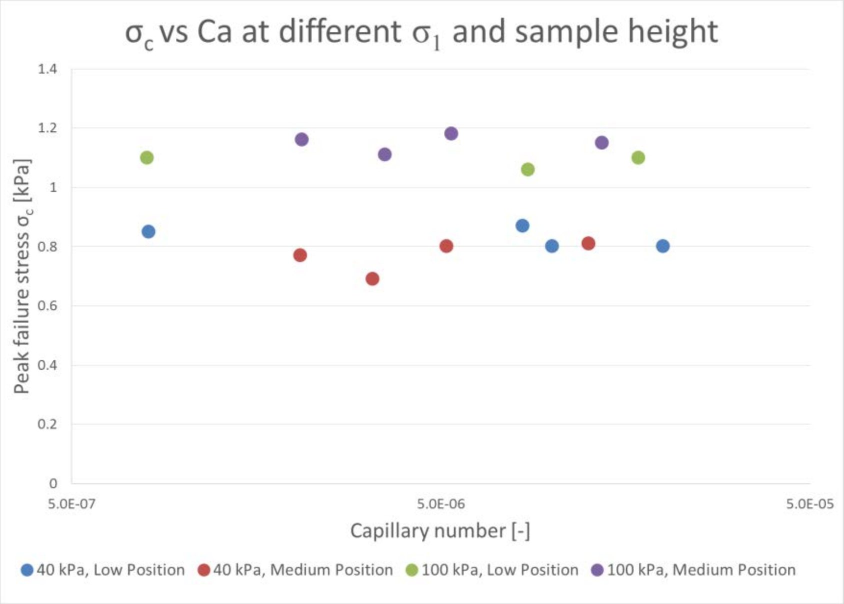

Figure 3.26: *Peak failure stress of MCC Cp-102+500 cSt silicone oil versus capillary number, at two different consolidation stresses (40 and 100 kPa) and for two different sample heights.*

The values of peak failure stress were uniform between the two sample heights, once the consolidation stress was fixed. It can therefore be assumed that, at low capillary numbers, the sample height does not have any relevant effect on σ_c as long as the consolidation stress applied is the same. The data collected with the low-position sleeve support are thus comparable with the ones obtained at medium-position both at high consolidation stresses (100 kPa) and at low consolidation stresses (40 kPa).

A different mind-set should be used when considering samples tested at larger capillary numbers. The work of Iveson and Smith, introduced in §1.3, describes how the viscous effects become predominant in determining the values of granule strength once Ca in larger than 10^{-4}: the term containing the capillary number in Equation 1.7 indeed overcomes the constant parameter and causes the profile of Str* to assume the shape observed in Figure 1.6. Therefore, as the strain rate $\dot{\varepsilon}$ is defined as:

$$\dot{\varepsilon} = \frac{v}{H} \tag{3.4}$$

where v is the failure velocity and H is the sample height, an increase of sample height would cause a decrease in the value of strain rate for the given sample. This would impact on the sample's capillary number as described in Equation 1.6, decreasing its value. Therefore, if Ca is larger than 10^{-4}, two samples prepared with the same wet granular material and tested at the same failure speed and consolidation stress may give as a result a different value of Str*, as they would show different capillary numbers.

It was therefore decided to fix the medium sleeve support position as the standard one, still keeping the initial testing results obtained at low sleeve support. Further experimental data supporting this decision can be found in Appendix 5.

3.3.2 Data collection

A large amount of experimental data was collected a different testing conditions. Considering that four different granular materials were available (three typologies of MCC and one of PMMA) and that each had to be tested at five sets of consolidation stresses, a total of 20 unique samples units had to be prepared. Furthermore, each material could be mixed with two different silicone oils, increasing the samples units number to 40.

It was decided to carry out at least four tests for each unit, at different deformation speed, in order to obtain information in a wide range of capillary numbers. A larger amount of samples were tested for MCC Cp-102 and PMMA, as they were used during the initial exploration phases to better understand the characteristics and the flexibility of the AUPT machine. Overall, over 200 tests were performed. For each test the AUPT software provides a PDF file collecting all the testing parameters, such as consolidation stress and deformation speed, and the testing results, such as failure stress and sample deformation. Figure 3.27 shows the results section of the test report of a MCC Cp-102+30000 cSt silicone oil sample, tested at 100 kPa of consolidation stress and 5 mm/s of failure speed. The red boxes highlight the most important data for the elaboration: the uniaxial unconfined yield stress (uUYS), or failure stress, and the sample compression.

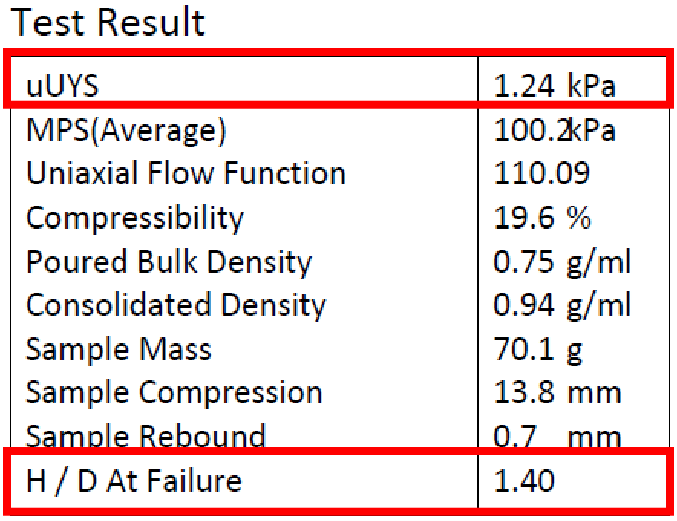

Test Result

uUYS	1.24 kPa
MPS(Average)	100.2kPa
Uniaxial Flow Function	110.09
Compressibility	19.6 %
Poured Bulk Density	0.75 g/ml
Consolidated Density	0.94 g/ml
Sample Mass	70.1 g
Sample Compression	13.8 mm
Sample Rebound	0.7 mm
H / D At Failure	1.40

Figure 3.27: *Example of test results for a MCC Cp-102+30000 cSt silicone oil sample, tested at 100 kPa of consolidation stress and 5 mm/s of failure speed.*

The data regarding failure stress, sample compression and poured and consolidated density were collected in multiple Microsoft Excel files and properly elaborated to evaluate the corresponding capillary numbers and dimensionless peak stresses.

One particular limitation observed during the testing phase is that the AUPT machine does not provide any information on the sample height after the application of the consolidation stress, therefore there is no measure available on the sample height at the beginning of the failure compression. This is an issue correlated to Equation 3.4: the strain rate $\dot{\varepsilon}$ is indeed evaluated as the ratio between the deformation velocity and the sample height at the beginning of the failure phase. But, lacking this last parameter, the exact $\dot{\varepsilon}$ can not be determined from the experimental data. It was therefore decided to assume that the sample height at failure could be approximated to the sample height after consolidation, which is known and can be calculated, as the two values are almost the same. From the AUPT reports, indeed, it was found out that the sample failure happens at low deformation percentages (generally, less than 5% of the sample height) and thus the assumption is solid. The strain rate was calculated as:

$$\dot{\varepsilon} = \frac{v}{H_0 - \Delta H_{fail}} \tag{3.5}$$

where ΔH_{fail} is the sample compression at failure, highlighted in the red box in Figure 3.27. With this assumption on the strain rate it was possible to evaluate the capillary number for each of the tested samples as:

$$Ca = \frac{\mu \cdot \dot{\varepsilon} \cdot d_p}{\gamma \cdot cos\theta} \tag{3.6}$$

where μ is the binder viscosity [Pa*s], d_p is the particle diameter [m], γ is the surface tension [N/m] and θ is the contact angle. As the values of contact angles are close or equal to zero for both MCC-oil and PMMA-oil systems, the value of $cos\theta$ is equal to 1.

The value of dimensionless peak stress was evaluated as:

$$Str^* = \frac{\sigma_c \cdot d_p}{\gamma \cdot cos\theta} \tag{3.7}$$

where σ_c is the uUYS, or peak failure stress [Pa]. The values of Str* and Ca were collected and accurately classified to build datasets that took into account material typology, binder viscosity and consolidation stress applied, in order to ease the further data elaboration. The large amount of data collected and elaborated as described in this section can be found in Appendix 5.

3.3.3 Data elaboration

The experimental values of dimensionless peak stress Str* and capillary number Ca were evaluated for each experimental test, and elaborated graphically in order to capture the behaviour of the different materials.

Initially it was observed how the uniaxial unconfined yield stresses behaved as a function of the different material and testing parameters, looking for preliminary correlations that could support the choices of the modelling phase. The parameters of interest were binder viscosity, particle size, deformation velocity and consolidation stress, each of which were varied as described in §3.3.3.1, 3.3.3.2 and 3.3.3.3. The contact angle with silicone oil, which could have been a parameter useful to distinguish the micro-crystalline cellulose behaviour from the PMMA, was found out to be equal to zero and, therefore, not considered as a variable parameter. The focus was then moved to the correlations between Str* and Ca, as shown in §3.3.4, and on the effects on the flow function, in §3.3.5.

3.3.3.1 Effect of binder viscosity

The first parameter considered was the binder viscosity, which could be chosen between two values: 500 and 30000 centiStokes, corresponding to 0.485 and 29.25 Pa*s, respectively. The effect on the uUYS was observed for all the four typologies of materials, at fixed deformation velocity and consolidation stresses. During the preparation phase it was possible to notice how the samples prepared with the 30000 cSt one were generally more compact and tended to have a more free-standing structure, while the ones with the 500 cSt oil deformed more easily under the effect of gravity and looked less stable. In Figure 3.28.a, 3.28.b, 3.28.c and 3.28.d the values of uUYS are shown for the four materials studied with the two different silicone oils, at a fixed consolidation stress of 20 kPa. The first set of values was captured at a deformation speed of 0.05 mm/s, corresponding to a strain rate of 0.0010 ± 0.0002 s^{-1}.

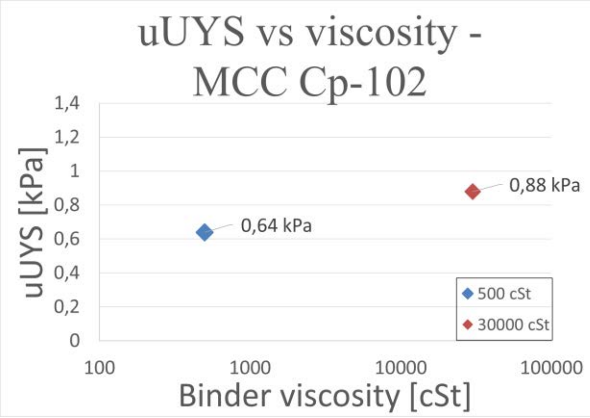

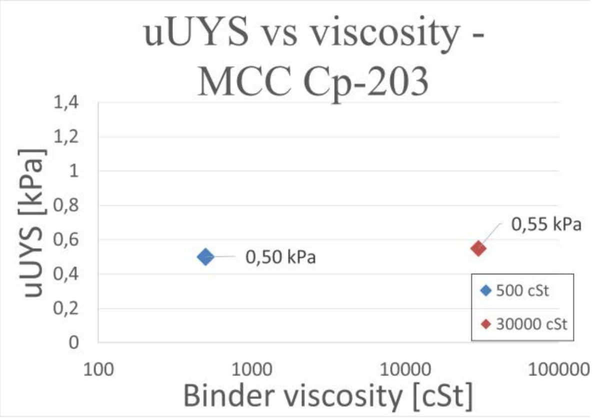

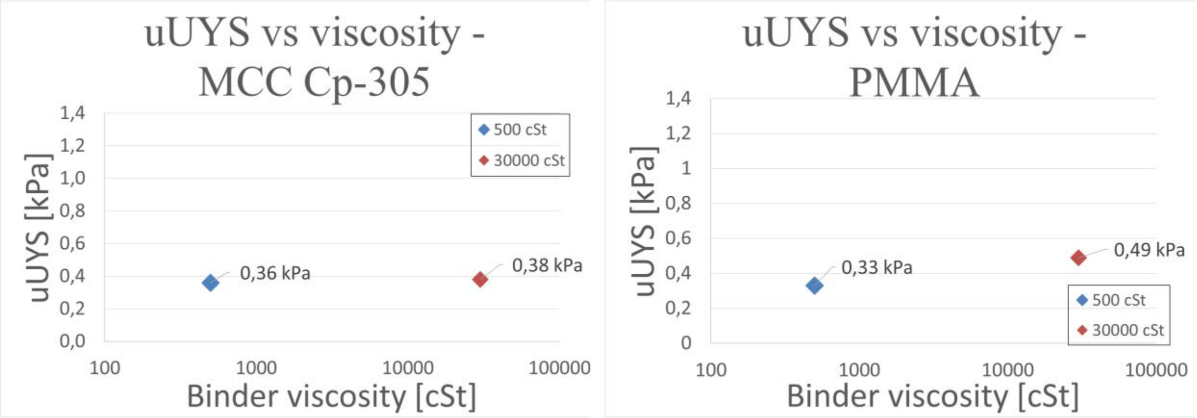

Figure 3.28.a, 3.28.b, 3.28.c, 3.28.d: *Values of uUYS for MCC Cp-102, Cp-203, Cp-305 and PMMA Elvacite 3001, respectively. Values shown for* 500 *cSt and* 30000 *silicone oils, with a constant* 20 *kPa of consolidation stress and measured at* 0.05 *mm/s of deformation speed.*

As can be seen from the graphs, there was a general homogeneity in the values of uUYS measured for samples with the two different silicone oils. The uniaxial unconfined yield stress was indeed just slightly higher for the 30000 cSt silicone oil samples, but the values were by far closer than what was expected from the initial analysis of the samples during the preparation phase.

The comparison was then repeated for values of uUYS measured at higher deformation velocity, equal to 5 mm/s. Figure $3.29.a$, $3.29.b$, $3.29.c$ and $3.29.d$ report the results obtained, still at 20 kPa of consolidation stress applied.

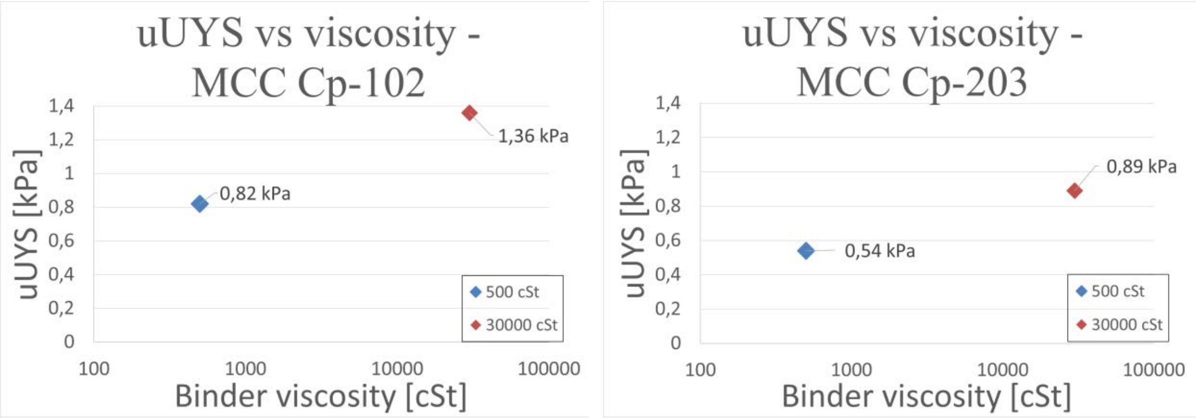

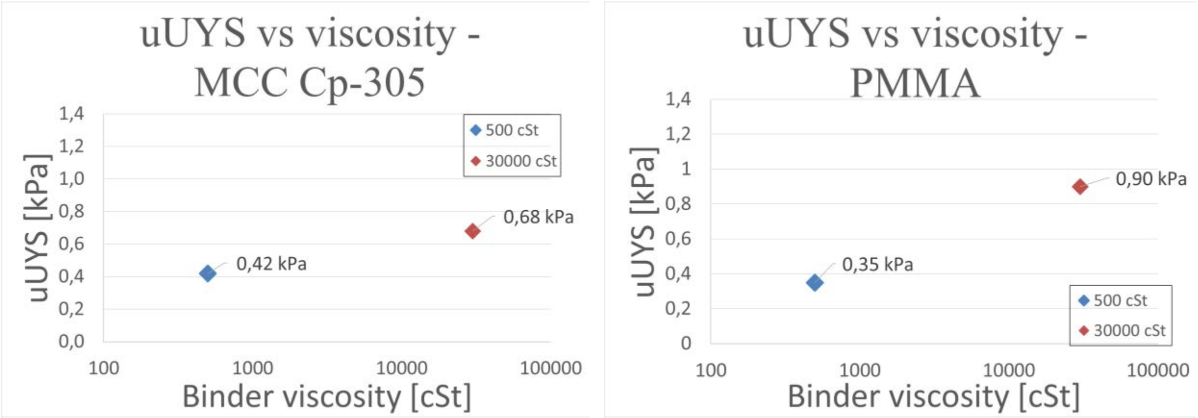

Figure 3.29.a, 3.29.b, 3.29.c, 3.29.d: *Values of uUYS for MCC Cp-102, Cp-203, Cp-305 and PMMA Elvacite 3001, respectively. Values shown for* 500 *cSt and* 30000 *silicone oils, with a constant* 20 *kPa of consolidation stress and measured at* 5 *mm/s of deformation speed.*

The values of uUYS are now by far more different between the samples prepared with the two typologies of silicone oils, with the high viscosity ones showing values around $40\% - 50\%$ higher than the low viscosity ones. Furthermore, the values measured for the 500 cSt silicone oil samples varied just by $5\% - 10\%$ from the previous values, measured at 0.05 mm/s of deformation velocity. The samples prepared with the high viscosity silicone oil instead shown an increase of $60\% - 80\%$ in their uUYS going from 0.05 mm/s to 5 mm/s.

This behaviour could be explained considering the internal structure of the wet granular sample, in which the solid particles are bound together by liquid bridges. At low deformation velocities the internal granules have more time to distribute and rearrange along the preferred deformation direction, offering less resistance to the piston compression and, therefore, a lower uniaxial unconfined yield stress. On the other hand, at high deformation velocities the granules do not have enough time to rearrange along a preferred direction and the sample gets compressed until the formation of internal cracks, at which corresponds the peak failure stress. The sample then proceeds to fail along the so formed failure plans, requiring lower compression stresses.

It was then decided to better observe the behaviour of granule strength as a function of binder viscosity at different consolidation stresses. In Figure $3.30.a$ and $3.30.b$ it is possible to see the values of uUYS for MCC Cp-203 for both binder typologies, at different consolidation stresses $(20, 40, 60, 80, 100$ kPa). Figure $3.2?.a$ reports the results at 0.05 mm/s of deformation velocity, while Figure $3.2?.b$ shows the values at 5 mm/s.

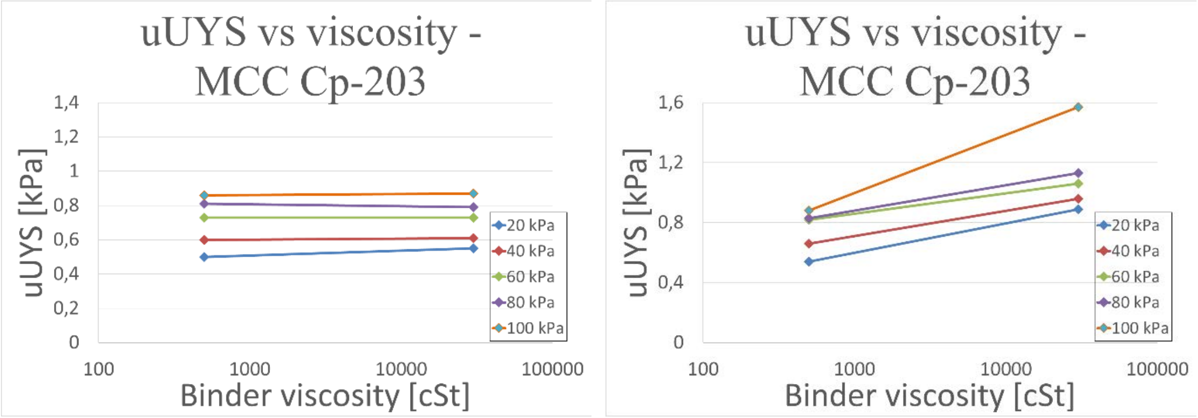

Figure 3.30.a, 3.30.b: *uUYS of MCC Cp-203 at different consolidation stresses, for both binder typologies. Deformation velocity of 0.05 mm/s and 5 mm/s, respectively***.**

It can be seen how the values of uUYS increase for all materials as a function of the consolidation stress applied, which consolidates the material and improves its resistance against deformation forces. The behaviour shown in Figure $3.28.a-d$ and $3.29.a-d$ remains, nevertheless, the same: at low deformation velocities, the uUYS slightly increases even if the binder viscosity increases by two order of magnitude, while at high deformation velocities the effect of binder viscosity is by far more evident. It is particularly interesting to notice how different values of consolidation stresses modify the values of uniaxial unconfined yield stress without significantly modifying the correlation between them, but maintaining the behaviour observed in Figure $3.28.a-d$ and $3.29.a-d$. The effect of the consolidation stress seems, therefore, to just act on the existing relationship between granule strength and material/test parameters by shifting the values of uUYS, but without interacting with their respective position. Further experimental elaboration is required to better capture this behaviour.

From these observations it can be deduced that the dependency of the uniaxial unconfined yield stress from the binder viscosity is not linear, but depends on the interaction of multiple parameters such as particle size, deformation velocity and consolidation stresses applied. Overall, the uUYS values of wet granular materials made of larger solid particles are lower than the ones made of smaller particles, once the other material and testing parameters are fixed. A silicone oil with higher viscosity grants a stronger liquid bonding, as could be expected from the formula for the viscous force shown Equation 1.5, even though its action is influenced by the deformation velocity chosen for the tests and can lead to different behaviours. The effect of aspect ratio was not yet considered, as the four materials offer generally similar values that would not largely impact the final behaviour.

3.3.3.2 Effect of particle size

Particle size effects on the uniaxial unconfined yield stress have already been partially considered in §3.3.3.1, but not fully captured by the experimental analysis. An initial consideration based just on particle structure is that smaller particles offer a larger surface per unit volume on which liquid bridges could form, thus granting generally stronger liquid bounds and an overall more resistant wet granular sample. Equation 1.5, shown in §1.2, describes the dependency of the capillary force from the particle size, d_p: the particle diameter indeed appears twice at the denominator, confirming the assumption for which the liquid bridge between larger particles offers a lower capillary force than the one between smaller particles.

This behaviour could also be observed during the sample preparation phases, as the binders tended to distribute more easily within the samples with larger particles and the so formed samples looked weaker and less compact than the ones made with smaller particles. In particular, while testing the samples made with MCC Cp-305, it happened a few times that the cylinder failed during the sleeve removal phase by slowing deforming in its middle section, which enlarged until failure. This behaviour, mainly related to the effect of gravity, did not show up in any of the other materials tested and was therefore reconnected to the larger particle size of MCC Cp-305, which offers less surface for the creation of liquid bridges.

The four particle sizes available were shown in Table 3.1 in §3.1.2, and the values considered were the d_{50} of each material. The first set of tests was carried out considering both the 500 cSt and the 30000 cSt silicone oil samples, for four different deformation velocities: $0.05, 1.0, 2.0$ and 5.0 mm/s. Figure $3.31.a$, $3.31.b$, $3.31.c$ and $3.31.d$ collect the results of the experimental testing, carried out at 20 kPa of consolidation stress.

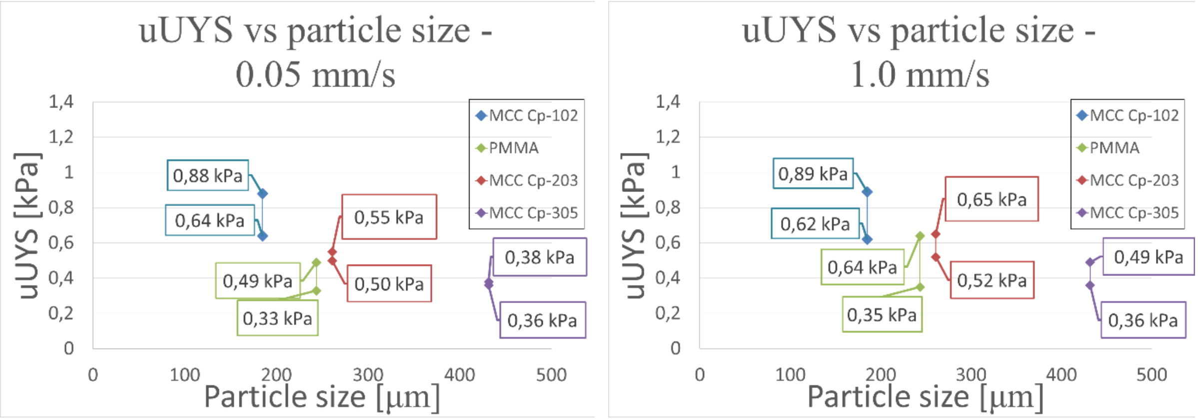

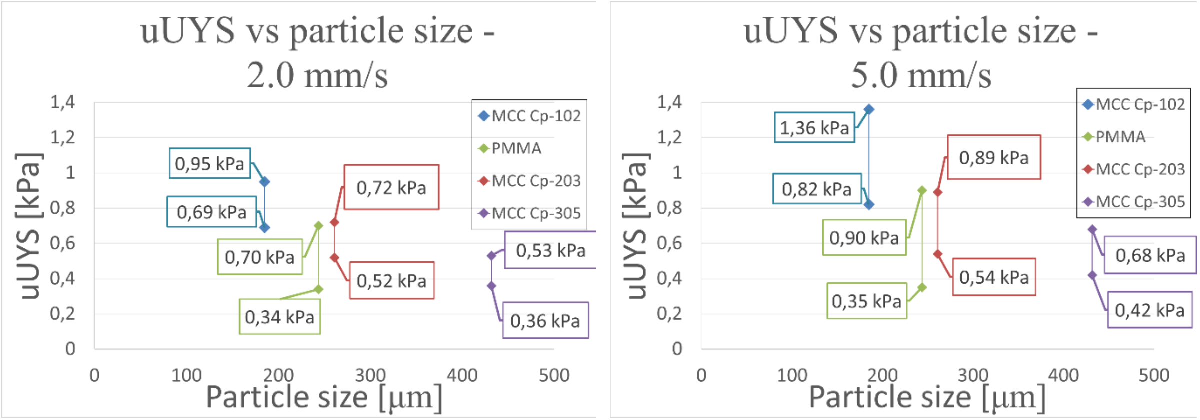

Figure 3.31.a, 3.31.b, 3.31.c, 3.31.d: *uUYS for different particle sizes considered (MCC Cp-102, Cp-203, PMMA, MCC Cp-305) at four different deformation velocities (0.05, 1, 2, 5 mm/s) and consolidation stress of 20 kPa.*

For each couple in each chart the highest value of uUYS corresponds to the 30000 cSt oil sample, which is always stronger due to the increased strength of the liquid bridge. Nonetheless, the gap between the two values increases as the deformation speed increases, as it is particularly clear comparing Figure $3.31.a$ to Figure $3.31.b$. The effect of deformation velocity seems to be indeed correlated to the material properties of the sample in a complex way, as the values of uUYS shift their relative position with different trends at different values of failure speed. Therefore, at lower deformation velocity the effect of the binder viscosity on the material performance under compression is almost negligible for MCC Cp-203 and Cp-305, while it has only a slight effect on the uUYS of MCC Cp-102 and PMMA.

As the deformation speed increases, the values of uniaxial unconfined yield stress for the samples made with the high viscosity binder increase, almost doubling their initial value while the velocity goes from 0.05 mm/s to 5 mm/s. On the other hand, the uUYS of the samples made with the low viscosity oil remain almost constant regardless of the deformation speed, with MCC Cp-102 being the only exception. It could be deduced that the effect of a different deformation speed is more evident in the case of wet granular samples made with smaller particles, even at lower binder viscosities.

The trend shown in Figure $3.31.a-d$ is particularly clear as regards the effect of particle shape on the uniaxial unconfined yield stress, and confirms the previous hypothesis. Wet granular samples made with powders that have a lower average diameter show a by far larger uUYS than any similar sample with larger average diameter, once the testing conditions are fixed. Furthermore, the value of uUYS seems to be more sensitive to changes in the deformation speed at low d_{50}: this can be noticed by comparing Figure $3.31.a$ to $3.31.d$, where peak stress shift shown by MCC Cp-102 is the largest one as absolute value.

Another interesting observation is that the values of uniaxial unconfined yield stress of PMMA is not perfectly aligned with the trend correlating the micro-crystalline cellulose samples, but rather shows slightly lower values than the other material. In the Figures $3.31. a-d$ indeed it can be seen how the PMMA points locate at lower values than the MCC Cp-203 ones, even though the d_{50} of the plastic material is slightly smaller. The uUYS of PMMA is particularly low when the powder is mixed with the 500 cSt silicone oil, causing the wet granular sample to be even weaker than the corresponding one made with MCC Cp-305, whose particle size is almost twice as large. Furthermore, the uUYS of the sample made with the low viscosity oil does not significantly change with the variation of the deformation velocity, staying close to the initial value of 0.33 kPa.

This behaviour could be correlated to the different particle shapes of PMMA and MCC samples, as collected in Table 3.2 of §3.1.3. The PMMA powder indeed shows an aspect ratio of 0.86, higher than the aspect ratios of all the MCC samples which show values equal to 0.83-0.84. A reasonable assumption could be that less spherical particles, such as the ones with lower aspect ratio, tend to pack in a more stable way and offer more frictional resistance to deformation than the more spherical ones. A less regular shape indeed grants more possibilities for particles interlocking, which overall increase the sample mechanical strength and, therefore, its uniaxial unconfined yield stress.

To recap, it is clear how the strength of a wet granular sample is inversely related to the average particle size of the powder used. Nevertheless, the correlation is not linear and depends on the interactions of other parameters, such as the binder viscosity and the aspect ratio of the material. It could be generally assumed that the granule strength inversely depends on both particle size and aspect ratio, with complex correlations.

It was then decided to study the effect of particle size on granule strength at different consolidation stresses, collecting data at the previous set of σ_1: $20, 40, 60, 80$ and 100 kPa. As Figures $3.31. a-d$ already collect the experimental analysis at 20 kPa of consolidation stress, it was decided to collect the data for the remaining four consolidation stresses showing the difference between the uUYS values measured at different deformation velocities. The experimental results can be seen in Figure $3.32. a-h$.

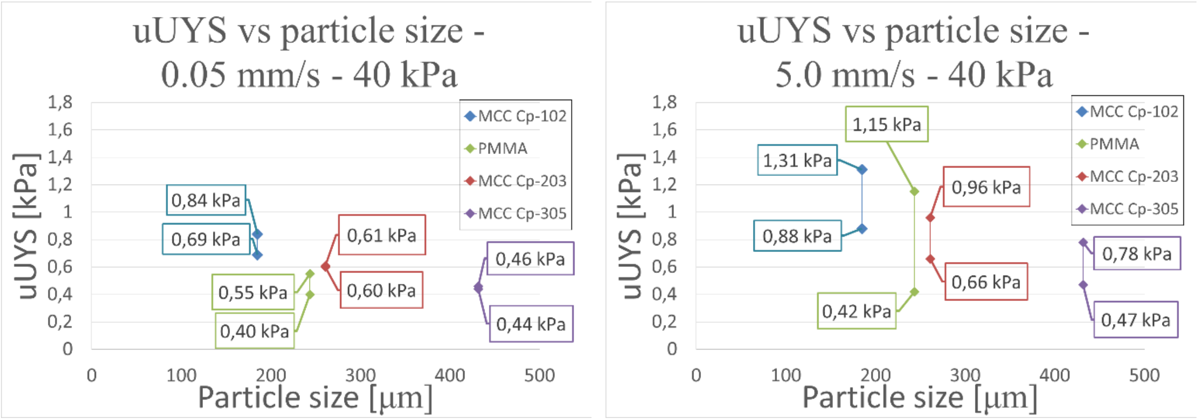

Figure 3.32.a, 3.32.b: *uUYS for different particle sizes considered (MCC Cp-102, Cp-203, PMMA, MCC Cp-305) at 0.05 and 5 mm/s of deformation velocity, and consolidation stress of 40 kPa.*

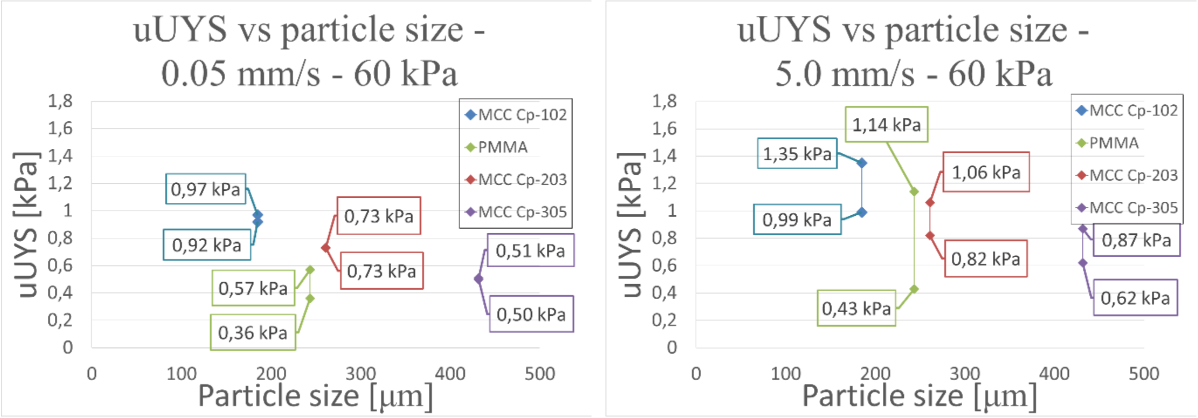

Figure 3.32.c, 3.32.d: *uUYS for different particle sizes considered (MCC Cp-102, Cp-203, PMMA, MCC Cp-305) at 0.05 and 5 mm/s of deformation velocity, and consolidation stress of 60 kPa.*

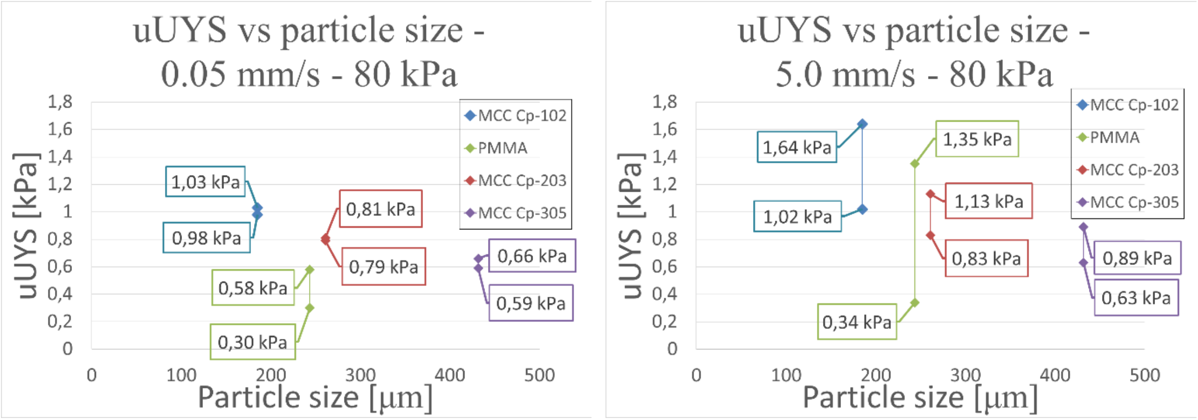

Figure 3.32.e, 3.32.f: *uUYS for different particle sizes considered (MCC Cp-102, Cp-203, PMMA, MCC Cp-305) at 0.05 and 5 mm/s of deformation velocity, and consolidation stress of 80 kPa.*

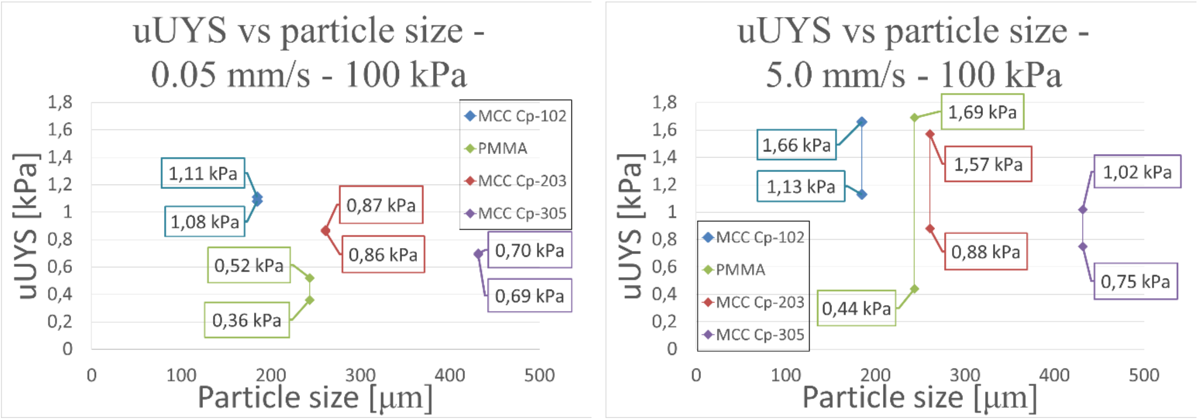

Figure 3.32.g, 3.32.h: *uUYS for different particle sizes considered (MCC Cp-102, Cp-203, PMMA, MCC Cp-305) at 0.05 and 5 mm/s of deformation velocity, and consolidation stress of 100 kPa.*

The trend observed in Figure 3.31.$a-d$ was confirmed by the further experimental analysis at different consolidation stresses shown in Figure 3.32.$a-h$. The wet granular samples made with particles having smaller size tend to offer a larger resistance to compression, and therefore a larger uUYS, regardless of the consolidation stress applied. For materials having particles with similar shapes, such as MCC Cp-102, Cp-203 and Cp-305, there is a clear dependency of the uniaxial unconfined yield stress from the particle size and its value slowly decreases as the d_{50} of the material increases. For PMMA, this behaviour is less regular and the values of the uUYS largely differ from case to case. When compressed at low deformation velocity, the PMMA samples offer a low resistance to deformation at any consolidation applied, with the samples made with the low viscosity oil showing close values to the ones made with high viscosity oil. This behaviour differs from the sample strength observed for the MCC samples tested at 0.05 mm/s, in which the uUYS values are particularly close.

On the other hand, when compressed at high speed the behaviour of the different PMMA samples changes significantly, showing a substantial increase in granule strength for the 30000 cSt samples that gets close to the values of MCC Cp-102. The span between the uUYS of the low and high viscosity samples gets larger as the consolidation stress applied increases, with Figure 3.32.h showing an upper value almost four times larger than the one of the samples made with the 500 cSt oil. The effect of velocity is prominent, too, with the uUYS evaluated at 5 mm/s being always higher than the ones evaluated at 0.05 mm/s.

Another interesting characteristic is that the effect of the different consolidation stresses changes between the samples tested at 0.05 mm/s and the ones tested at 5 mm/s. At lower deformation velocities, the uUYS values of the high and low viscosity samples are almost equal and maintain their relative position as the consolidation stress changes, shifting to higher values as σ_1 increases. The increment is of about 10% from one set of consolidation stress to the other. The only exception is PMMA, whose values of uUYS do not change significantly among the

different consolidation stresses applied but remain almost constant, even decreasing at 100 kPa. This behaviour, which does not have a clear explanation connected to a specific characteristic of the material, was taken into account in the model evaluation of §4.1, even though a more in-depth analysis may be required to fully understand and describe this peculiar characteristic.
At 5 mm/s instead the uUYS values of the high and low viscosity samples increases with the consolidation stress, as well as the gap between them. This phenomenon is more evident for the MCC Cp-102 sample, while the Cp-203 and Cp-305 samples show an increase in the values of uUYS but an almost constant relative position between high and low viscosity specimens. PMMA, once more, shows an irregular behaviour even at 5 mm/s of deformation speed. The strength of the sample made with the low viscosity binder is almost constant, regardless of the consolidation stress applied. The sample made with the high viscosity binder, on the other hand, shows an uUYS almost constant at 40 kPa and 60 kPa and a sharp rise at 80 kPa and 100 kPa, when the PMMA samples reach an uniaxial unconfined yield stress almost equal to the one of the MCC Cp-102 samples. Further experimental analysis was carried out to properly understand whereas this behaviour was intrinsic of the material, possibly due to its interactions with the high viscosity silicone oil, or just depended on a random irregularity in the testing conditions. The effect of the different particle shape was indeed considered to be not sufficient to justify such a large difference in the values of uUYS.

One last, interesting detail that was observed from the graphical representation in Figure $3.32.a-h$ is that each wet granular materials has its own characteristic correlation between the values of σ_1 and uUYS (or σ_c), defined as flow function, or FF. Figure $3.33.a$ and $3.33.b$ show the flow functions for MCC Cp-102 with the 500 cSt and the 30000 cSt binders, respectively, at different deformation velocities.

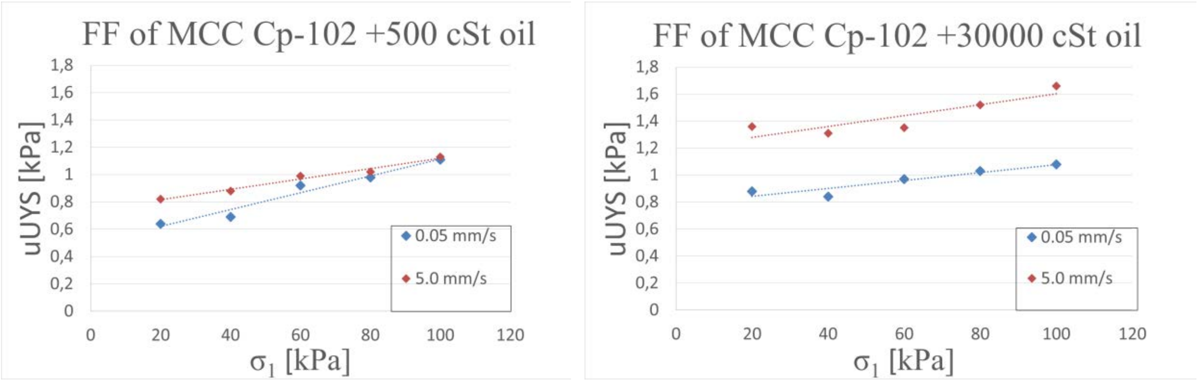

Figure 3.33.a, 3.33.b: *Flow function (FF) of MCC Cp-102 with the 500 cSt silicone oil (a) and the 30000 cSt silicone oil (b), at different deformation velocities.*

It was noticed that the flow function does not just depend on the solid characteristics, such as for the flow functions of dry materials, but also on the binder properties, which determine the strength of the capillary and viscous forces holding the wet granular material together. Their interaction seems to determine both the slope and the intercept of the FF, and thus characterise the resulting flowability of the granular material. Furthermore, from Figure 3.33. a it could be noticed how the two flow functions measured at different deformation speeds are almost coincident, while for the high viscosity sample the two lines differ one from the other by a large gap. It can be deduced that the flow function of a wet granular material may not depend just on the materials characteristics, such as particle size and binder viscosity, but also on the testing conditions at which the experimental analysis is performed. Furthermore, it seems that at high binder viscosity and high deformation speed the material shows a different flow behaviour, with a flow function that largely differs from the ones measured at different material and testing characteristics. The further analysis of §3.3.4 and §3.3.5 aim at investigating these possible implications.

To recap, it was observed how the effect of particle size and, to a less extent, shape largely influence the behaviour of wet granular materials undergoing uniaxial compression. A solid material with smaller particle size offers stronger capillary forces, while a more irregular shape grants the possibility of having particle interlocking and, therefore, a higher uUYS. The effect of different consolidation stresses causes a shift in the values of uniaxial unconfined yield stress, even though different values of binder viscosity and deformation speed interact in a complex and non-linear way. Furthermore, the behaviour of PMMA departs from the one of MCC at higher consolidation stresses and may require further characterization.

3.3.3.3 Effect of deformation velocity

Given the results of §3.3.3.2, specific focus was put onto the analysis of the effects of deformation velocity on the dynamic strength of wet granular materials. It has already been observed how different deformation speed highly influence the behaviour of the wet granular material, interacting with other properties to determine large increases in the values of dynamic strength. Overall, it has been noticed how a powder with small particle size mixed with a high viscosity binder produces a sample more resistant to uniaxial compression, but the grade of increase still seems to be dependent on the speed at which the compression is carried out. This behaviour could be correlated to the microscopic structure of the wet granular sample, in which a slow compression allows the different granules to have time to deform and rearrange along the main direction, which cannot happen in the case of a quick compression. Moreover, in most agglomeration processes the deformation that granules undergo happens at high velocities (impeller tips can move at speeds even above 100 mm/s), therefore there is particular interest in further understanding the effects of such high velocities on the properties of the granules. Unluckily the Advanced Uniaxial Powder Tester available was only able to reach deformation speeds up to 5 mm/s, hence further analysis should be performed to confirm the predictions of this study.

During the initial practice with the AUPT machine a wide range of compression velocities were tested, both to understand the flexibility of the machine and to improve the expertise with the testing procedure. Because of this choice, a large amount of data was collected for the MCC Cp-102 plus 500 cSt silicone oil combination at three consolidation stresses: 20, 40 and 100 kPa. Once the full set of consolidation stresses was chosen, experimental data was collected also for σ_1 equal to 60 and 80 kPa. Figure 3.34 represents the values of uUYS for the sample, as a function of the deformation velocity.

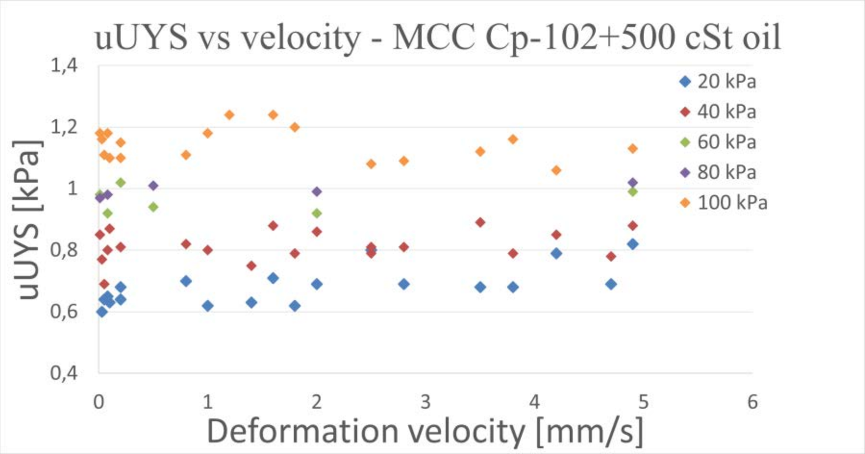

Figure 3.34: V*alues of uUYS versus deformation velocity for MCC Cp-102 + 500 cSt silicone oil, measured at 20, 40, 60, 80, 100 kPa with the AUPT machine*.

The experimental values obtained partially confirm the previous assumptions, as at low compression velocities the uniaxial unconfined yield stresses are almost constant within the same set of consolidation stress. But as the deformation speed increases there is no remarkable growth in the sample strength, not even at 5 mm/s, meaning that for the MCC Cp-102 + 500 cSt oil sample the dependency of uUYS from the deformation velocity and, thus, from the strain rate $\dot{\varepsilon}$ is negligible. This could be due to the low viscosity of the binder, which causes the capillary forces between the particles to be not sufficiently robust to offer an enhanced deformation resistance at high velocities. Nonetheless, the result is particularly interesting as it suggests how the dynamic strength of the wet granular material considered does not depend on the deformation speed: this means that in an industrial application the granules would offer the same resistance to deformation and breakage regardless of the compression speed used (as long as inside the considered interval), which could then be tuned to reduce the power consumption of the granulator.

As regards the effect of the consolidation stresses, it can be observed that the values of uUYS get traslated higher and higher as σ_1 increases. It is not possible to individuate a specific trend yet, but the displacement seems to be linearly correlated to the values of consolidation stress or, at most, with a slight exponential tendency. Furthermore, it is interesting to notice how the traslation effect can be assumed to be, with good approximation, constant along the whole set of deformation velocities tested. Therefore, if a sample of the considered composition gets consolidated during a storage, handling or process phase, it will offer an increased resistance to deformation on the basis of how much it has been consolidated. It could happen that, for a wet granular material consolidated at high stresses and being processed in a granulator, the deformation applied by the breakage device could not be sufficient for the granules to fail, causing irregularities in the particle size of the final product. Extending the knowledge of the effect of different consolidation stresses on the granule strength could allow to predict these problematical operating conditions and, possibly, intervene on the process equipment to confine any irregularity.

Once all the selected powders and the 30000 cSt silicone oil were available, the uniaxial testing was extended to all the other wet granular materials. In Figure 3.35 it is possible to see the values of uUYS obtained for the MCC Cp-102 plus 30000 cSt silicone oil sample, for the five consolidation stresses chosen.

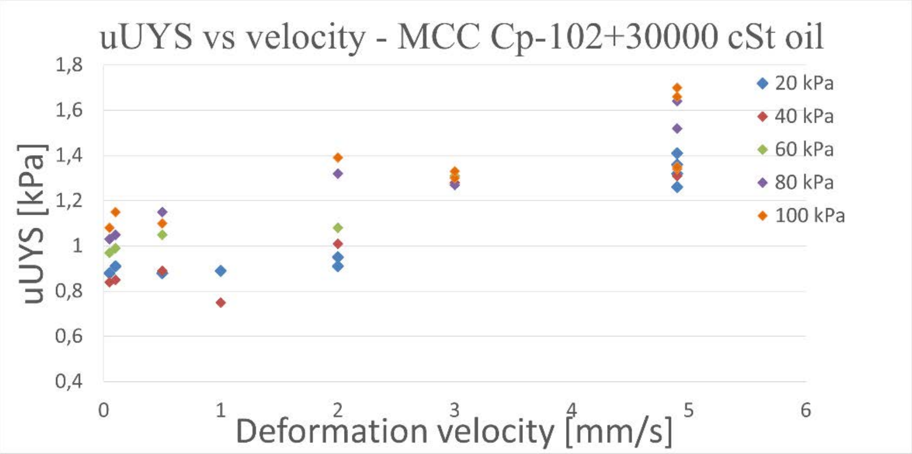

Figure 3.35: *Values of uUYS versus deformation velocity for MCC Cp-102 + 30000 cSt silicone oil, measured at 20, 40, 60, 80, 100 kPa with the AUPT machine.*

The behaviour of the material now is completely different from the previous sample, with a sharp increase in the values of uUYS as the deformation velocity increases. The samples tested at 5 mm/s are indeed almost twice as strong as the ones tested a low velocity, while even at intermediate speeds it is possible to notice a prominent increase in the values of uUYS. The most interesting particular is that at low deformation velocities the samples, even if prepared with a by far more viscous silicone oil, do not show a clear increase from the values of uUYS obtained for the MCC Cp-102 plus 500 cSt oil ones. It can be deduced that at very low deformation speeds the effect of binder viscosity, and thus the strength of capillary forces, has a less significant impact on the overall strength of the wet granular sample, which deforms and fails at similar stresses as the one previously analysed. The main difference between the two behaviours starts to appear only for values of deformation velocities above 1 mm/s.

The effect of the consolidation stresses is not easily observable, given the experimental uncertainty and the low consistency in the cylinder preparation described in §3.3.1 and §3.3.2, but the points distribution still allows to recognise how the samples compressed at 100 kPa present a higher value of uUYS than the other ones. Furthermore, the effect of traslation observed in Figure 3.34 is not so evident, and the analysis of the wet granular materials made with the other three powders was required to test and support the previous assumption. In Figure 3.36.$a - f$ it is possible to see the values of uUYS collected for MCC Cp-203 and Cp-305, as well as for PMMA Elvacite® 3001, mixed with the two different silicone oils.

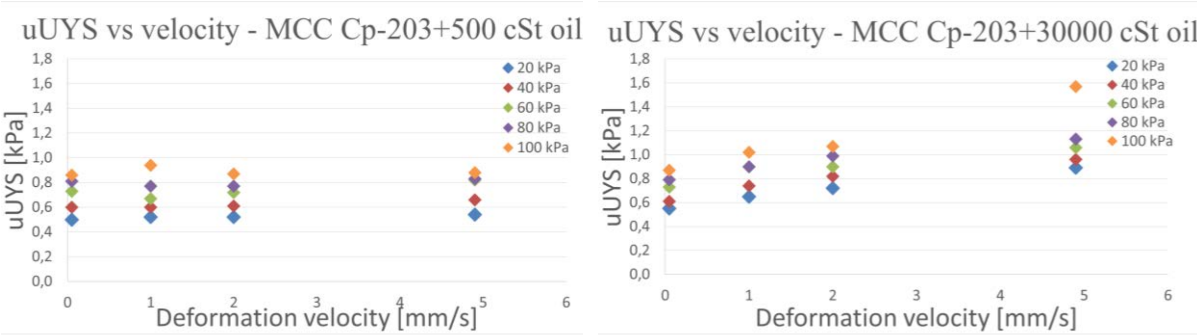

Figure 3.36.a, 3.36.b: V*alues of uUYS versus deformation velocity for MCC Cp-203 + 500 cSt and 30000 cSt silicone oils, respectively. Measured at 20, 40, 60, 80, 100 kPa with the AUPT machine.*

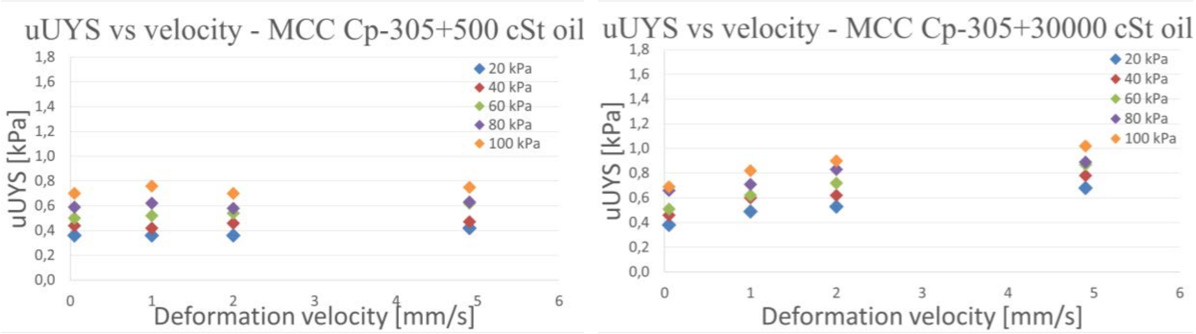

Figure 3.36.c, 3.36.d: *Values of uUYS versus deformation velocity for MCC Cp-305 + 500 cSt and 30000 cSt silicone oils, respectively. Measured at 20, 40, 60, 80, 100 kPa with the AUPT machine.*

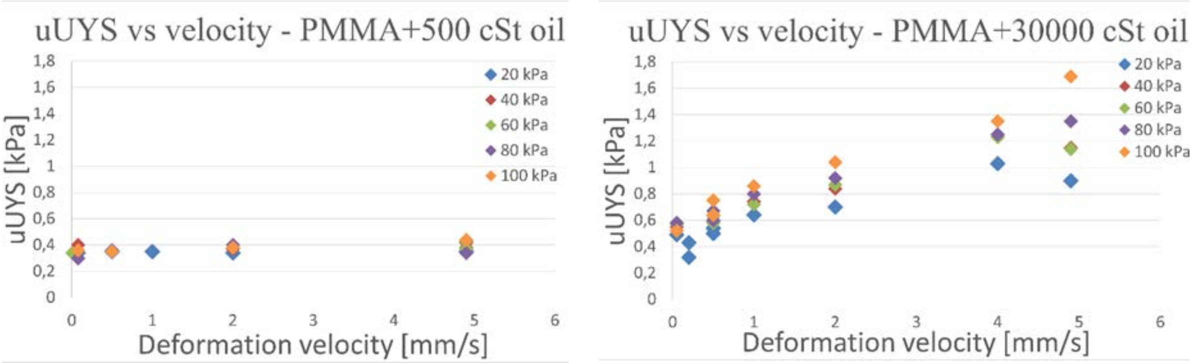

Figure 3.36.e, 3.36.f: V*alues of uUYS versus deformation velocity for PMMA + 500 cSt and 30000 cSt silicone oils, respectively. Measured at 20, 40, 60, 80, 100 kPa with the AUPT machine.*

From Figure $3.36.a - d$ it can be seen how the behaviour of MCC Cp-203 and Cp-305 is by far more regular than MCC Cp-102, mainly due to the smaller amount of experimental data collected. The trend is similar to the one observer in 3.34 and 3.35: for the samples prepared with the low viscosity oil indeed the values of uniaxial unconfined yield stress are almost constant at any of the velocities tested. The values of uUYS measured are, for the same consolidation stress, lower than the ones measured for MCC Cp-102 due to the increasing particle size of MCC Cp-203 and MCC Cp-305. The effect of different consolidation stresses is well represented by both samples, with the values of granule strength getting higher and higher as σ_1 increases. The shape of the dependency is not particularly clear, with a trend that could be either linear or exponential, but overall confirms the assumption of a traslational effect of the consolidation stress.

Considering the MCC Cp-203 and CP-305 samples mixed with the high viscosity silicone oil, it can be clearly noticed how an increase in the deformation velocity causes a mild increase in the values of uUYS, maintaining the relative distance between the values obtained at different consolidation stresses. The values obtained at 5 mm/s are still lower than the ones obtained for the MCC Cp-102 samples, confirming the results of §3.3.3.2. Furthermore, the traslational effect of different consolidation stresses is more evident than in Figure 3.35, and it can be seen how the distance between the datasets remains almost constant at different deformation velocities. This behaviour suggests that σ_1 could affect uUYS in a way that is separated from the effect of material properties and testing parameters. See §4.1 for a more in-depth discussion on this effect.

The behaviour of the PMMA samples is slightly different from the MCC ones, for both typologies of silicone oils. The values of uUYS obtained for the low viscosity oil samples are by far lower than any of those obtained from the MCC samples, and there is no evidence of a traslational effect due to different consolidation pressures. This could be due to the particularly low strength of the wet granular sample, whose particles have a high aspect ratio and, thus, a lower resistance to deformation. The high viscosity oil sample, on the other hand, shows a sharp increase in the values of uUYS when the testing velocity increases, reaching values comparable to the MCC Cp-102 sample when compressed at 5 mm/s. Nonetheless, at low deformation speeds the sample still exhibits a particularly weak behaviour. The traslation is clearly evident in Figure $3.36.f$, with the experimental data confirming the assumptions made for MCC.

3.3.4 Dimensionless analysis of uniaxial compression

In §3.3.3 the dependency of the uniaxial unconfined yield stress, or failure stress, from each material and testing parameters was deeply looked into and supplied with a comprehensive dataset of experimental measures. Table 3.6 collects the effects of each property on the value of uUYS.

Table 3.6: *Effect of material and testing parameters on uUYS.*

Higher value of:	**Effect**
Binder viscosity	At low deformation velocities, the effect is negligible. At high deformation velocities, uUYS increases.
Particle size	The uUYS decreases at any deformation velocity.
Deformation velocity	At low binder viscosity, the effect is negligible. At high binder viscosity, uUYS increases.
Consolidation stress	The uUYS increases at any condition.

It was therefore decided to shift the analysis to two dimensionless numbers, Str* and Ca, able to take into account all the properties and parameters listed in the table. The two dimensionless numbers were evaluated for each experimental test as described in Equation 3.6 and 3.7. The capillary number collects the parameters related to the binder characteristics and the strain rate (and, thus, the deformation velocity), as well as the particle size, while the dimensionless peak stress depends on uUYS and on particle size. From their definition it can be seen how the denominators are the same for both dimensionless numbers, and in the case under study their value will be equal for all the four materials considered as the binder surface tension and contact angle are the same. It should be noticed that the consolidation stress does not appear in their definitions, as none of the previous studies ever considered its role in the determination of the dynamic strength of a wet granular sample. This shortcoming is addressed in §4.1.

The values of Str* and Ca were collected for each material and can be seen in Figure $3.37.a$, $3.37.b$, $3.37.c$ and $3.37.d$, parametrised on the consolidation stress applied.

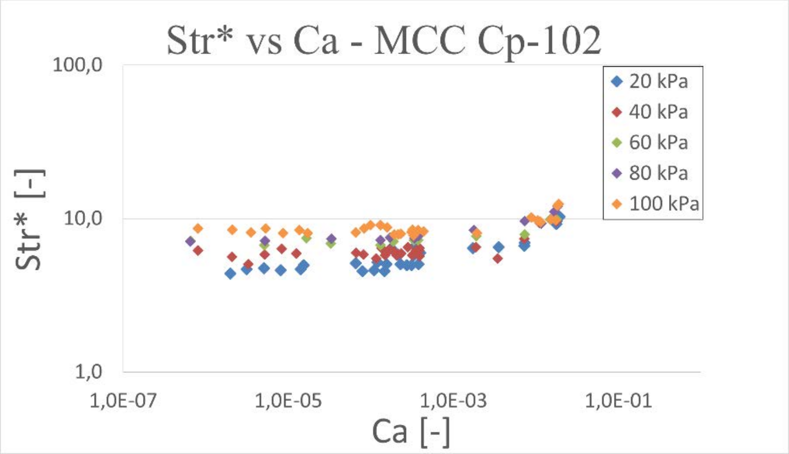

Figure 3.37.a: *Str* vs Ca for MCC Cp-102, measured at 20, 40, 60, 80 and 100 kPa.*

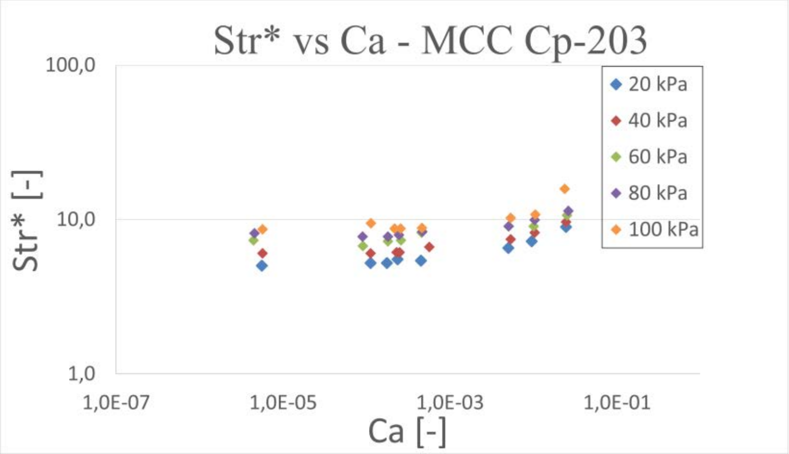

Figure 3.37.b: *Str* vs Ca for MCC Cp-203, measured at 20, 40, 60, 80 and 100 kPa.*

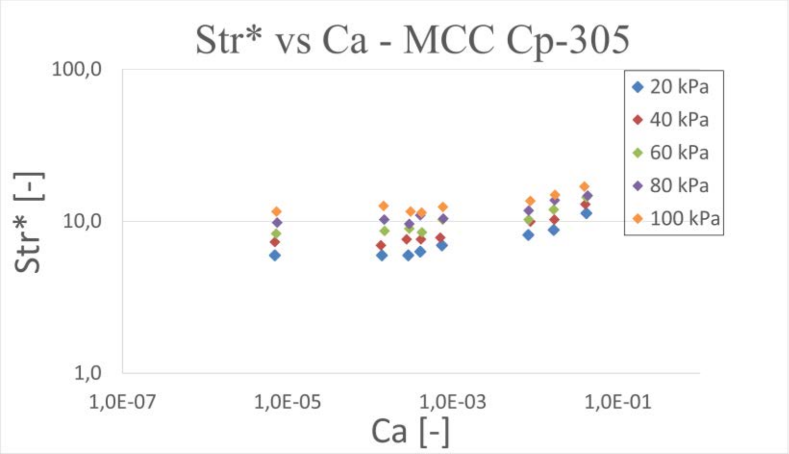

Figure 3.37.c: *Str* vs Ca for MCC Cp-305, measured at 20, 40, 60, 80 and 100 kPa.*

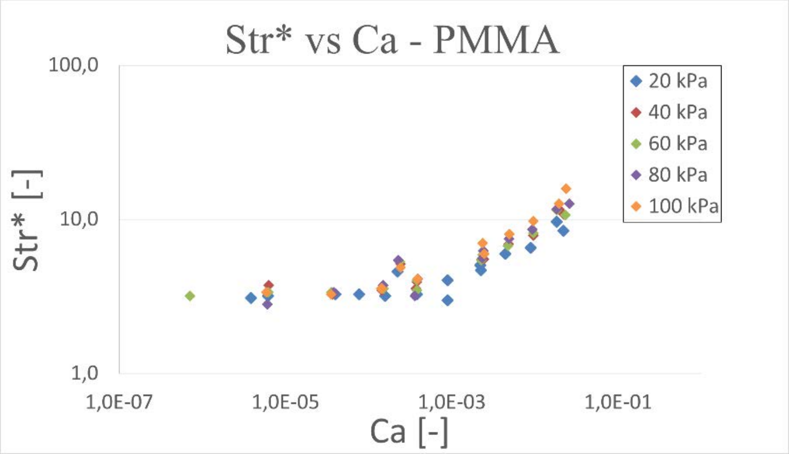

Figure 3.37.d: *Str* vs Ca for PMMA, measured at 20, 40, 60, 80 and 100 kPa.*

All the Figures present a similar trend for their correlation between Str* and Ca. For samples having low capillary numbers ($< 10^{-4}$), which correspond to a low viscosity binder and/or low strain rate, the value of Str* does not depend significantly on Ca for any of the materials tested.

For samples showing a larger capillary number instead Str* starts to rapidly increase, with a trend that seems similar for all the materials tested. It should also be noticed that with the available materials and equipment it was possible to only reach values of Ca in the order of 10^{-2}, and further experiments should be performed with instrument similar to the AUPT but able to work at higher deformation velocities. The most interesting result is the fact that all the four powders studied present, with a good approximation, the same correlation between Str* and Ca. This happens in particular for the values of capillary number higher than 10^{-3}, which corresponds to the more interesting section of the graph: large values of Ca indeed correspond to high deformation velocities, closer to the ones normally used in granulation processes. This correlation is further analysed in §4.1. As regards the effect of the consolidation stresses, it is clear how the traslation phenomenon appears when representing the data through dimensionless numbers, too. Furthermore, even at higher capillary numbers the relative position between curves at different consolidation stresses seems to remain the same, providing further evidence on the hypothesis of non-interaction between the capillary number and the consolidation stress on the final value of uUYS. All the collected and elaborated data can be found in Appendix 5.

3.3.5 Evaluation of the flow function

The traslational effect, widely observed during the examination of the experimental results, has particular interest as it could also be seen as an expression of the flow function of the wet granular material. The dimensionless peak stress indeed is a linear function of the uniaxial unconfined yield stress, as shown in Equation 3.7, and therefore the correlation between Str* and σ_1 can be seen as a correlation between uUYS and σ_1, which is defined as flow function. From this point of view it could be expected that for a given wet granular sample, whose particle size d_p and binder viscosity μ are fixed, the value of uUYS should be fixed once the consolidation stress is fixed. But as can be seen from Figure $3.36. a-f$, the values of uUYS widely depend on the speed of compression, too. This leads to a behaviour that has never been considered nor for the flow function of dry granular materials, nor for wet granular materials: the flow function, and therefore the flowability, do not just depend on material properties but also on the conditions at which the testing has been performed. This is particularly meaningful as it indicates that different equipment that work at different failure speeds could have a high impact on the value of σ_c, and thus on the flow function of the material.

Defining the flow factor ff as:

$$ff = \sigma_1/\sigma_c \tag{3.8}$$

it is possible to characterise, as for dry materials, the flowability of a wet granular material based on its value. To show the effect of testing conditions on the flow factor, the flow function

FF was represented graphically in Figure 3.38 for MCC Cp-203 mixed with 30000 cSt silicone oil at two different deformation velocities.

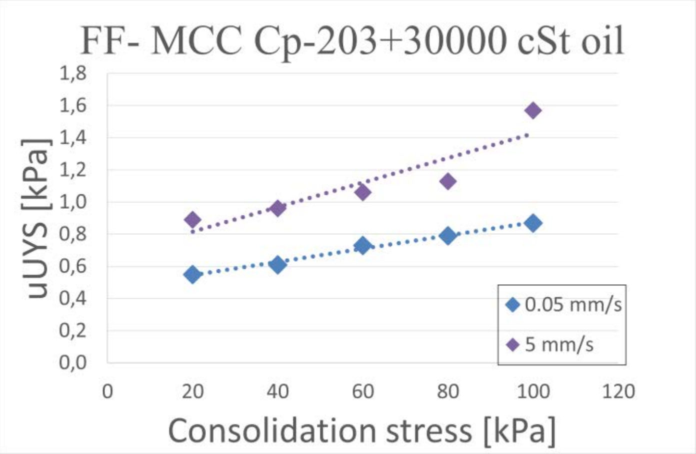

Figure 3.38: *Flow function for MCC CP-203+30000 cSt silicone oil, at 5 mm/s and 0.05 mm/s of deformation velocity.*

It can be easily seen how the two curves have a similar slope at the two different deformation velocities, while the sample tested at 5 mm/s showed a by far larger sample strength once undergoing the same consolidation stress. The material therefore presents different flowability once tested at different conditions, and to compare the two behaviours it is required to identify a flowability index such as the flow factor. Through its evaluation it is possible to characterise the flowability of a wet granular material, as is usually done for dry powders: the higher the flow factor, the less the material is affected by consolidation and, thus, the higher flowability. In §4.1 a possible correlation for the prediction of this behaviour was researched.

3.4 Diametrical testing

The previous section focused on the behaviour of wet granular materials undergoing uniaxial compression, and the effect of different testing conditions. The same analysis was extended to their behaviour during diametrical testing, to possibly identify any recurrent characteristics during their deformation and breakage processes. Furthermore, a new parameter was introduced in the form of the *preparation stress* $\sigma_{1,d}$, defined as the consolidation stress applied during the preparation of the sample, and whose effects on the diametrical strength of the wet granular materials were widely analysed.

3.4.1 Experimental design

The experiments were performed using an Instron® 1175 Universal Testing machine, following the procedure described in §2.2.6. The cylindrical pellets had a diameter of 13 mm and a variable final length in the range $12 - 14$ mm, and were prepared pouring a mass of 1.80 ± 0.05 grams in a 13 mm die and then compacting at fixed pressure. The amount of material was chosen to have a $1:1$ ratio between sample height and diameter, similarly to the geometry of the AUPT testing. The die was then slowly compressed with the Instron machine at the fixed speed of 0.25 mm/s. It should be noticed that the die did not allow to obtain a double-ended consolidation as described in §3.3.1.1, therefore there could have been some structural irregularities along the axis of the cylinder. But as the consolidation stresses applied were generally high if compared to the AUPT values, it could be assumed with good approximation that the cylinder structure had enough time to distribute their effect on the whole granular material, reducing the axial irregularities. Figure 3.39 shows a schematic of the testing procedure:

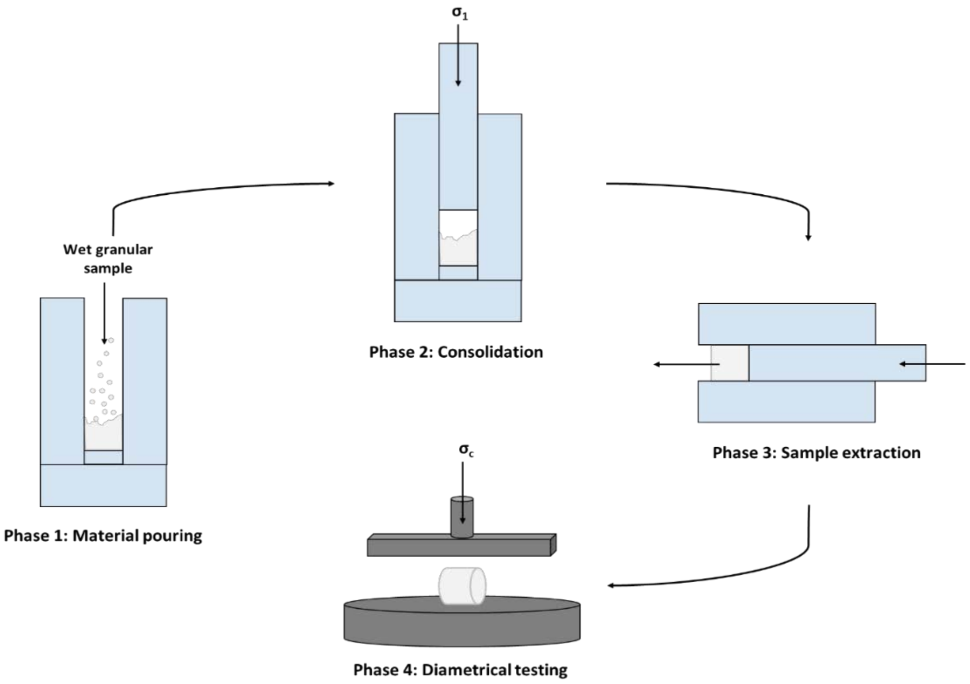

Figure 3.39: *Schematic of the diametrical test procedure.*

The choice of the consolidation stresses was not trivial, as all the previous works never considered the effect of the sample preparation conditions on the final strength of the wet granular sample. Furthermore, while the AUPT machine had a limited range of applicable consolidation stresses, the Instron® machine allowed to utilise a broad range of operating stresses by substituting the load cell with different models. In this way it was possible to go from consolidation loads of 1 N, corresponding to a consolidation stress of 7 kPa, up to 100 kN, corresponding to a consolidation stress of 700 MPa. The accuracy of the measurement varied accordingly to the range of the load cell, with the $1-100$ N one allowing to obtain measurements precise up to 10^{-1} N. Furthermore the top punch of the die was weighted in order to evaluate the stress it was going to apply to the material once it was positioned. With a mass of 152.80 ± 0.05 grams, the applied consolidation stress was calculated as described in Equation 3.9:

$$\sigma_{die} = \frac{m_{punch} \cdot g}{\pi \cdot d_{die}^2/4} \tag{3.9}$$

where m_{punch} is the mass of the top punch [kg], g is the gravity acceleration [m/s^2] and d_{die} is the diameter of the lower punch of the die [m]. The calculation gave as a result a consolidation stress of 11.30 kPa, meaning that the load to apply through the Instron® machine had to be tuned to consider this stress component from the die itself.

Initially it was decided to work with the same set of consolidation stresses used for the uniaxial testing, to grant consistent results between the two studies. Nonetheless, it was soon clear that such low consolidation stresses would not be suitable for the diametrical testing, which required first to remove the compacted cylinder from the die, and then to place it on a plane surface for the deformation compression. Both procedures apply intense stress to the sample, which could easily deform or break even before starting the actual testing if not compacted enough. The first sample considered was MCC Cp-102 mixed with 500 cSt silicone oil, with the same composition used for the uniaxial testing. 1.80 ± 0.05 grams of wet granular material were poured in the die, the upper punch was placed and the die was positioned between the Instron® platens, as shown in Figure 2.7.

The first consolidation load applied was of 12 N, corresponding to a consolidation stress of 89 kPa: combined with the consolidation applied by the top punch the final value of σ_1 was equal to 100 kPa. The consolidation load was applied at a speed of 0.5 mm/s, accordingly to the value used for the uniaxial testing. But as soon as the load was removed and the cylindrical sample was pushed out from the die, it was clear that such low consolidation stresses were not suitable for the diametrical compression testing. The cylinder indeed deformed and broke during the extraction phase, even if carried out with extreme care: out of three samples prepared, none of them was consolidated enough to be able to sustain the process. In the AUPT testing, indeed, the equipment is structured in such a way that the cylinder undergoes very low stresses during the sleeve removal phase, slightly deforming just on the external surface. On the other hand, to extract the cylinder from the dye it was required to push it using the top punch, deforming its surface. Furthermore, once it had been pushed to the end of the die, the sample was collected on a platen to be later positioned for the diametrical testing: if the sample was not consolidated enough the effect of gravity could easily make it deform along the diametrical direction and, during the testing, give a misrepresented value of the actual granule strength.

Because of these observations, it was decided to increase the consolidation load until the cylindrical sample could be properly extracted and positioned for the diametrical testing. The first try was made by applying a consolidation load of 500 N to the same combination of MCC Cp-102 and silicone oil, but with no success: the sample damaged during the extraction phase and quickly deformed along its diameter once positioned on the platen. The successive tries were made applying a consolidation load of 5 kN: the samples looked particularly resilient during the extraction phase but got easily damaged while positioning it on the Instron platens, and deformed because of the effect of gravity. Nonetheless, the order of magnitude of the consolidation stress looked suitable for the application, and a further test was carried out at 10 kN. The sample was extracted without any damage and positioned on the Instron platen without any deformation. Furthermore, it seemed that the effect of gravity was negligible as no major deformation appeared after a set time of 10 minutes. Similar results were obtained when using the 30000 cSt silicone oil. Out of more than 60 samples prepared, just one deformed due to an imprecision during the extraction phase.

It was then decided to test a PMMA sample, mixed with 500 cSt silicone oil, starting from a consolidation value of 10 kN. During the extraction phase it became clear how the PMMA granules were not suitable for the application, as they did not stick together and the sample easily broke. Even increasing the consolidation stress to 90 kN, close to the upper limit of the load cell, the material could not stick together and kept failing during the extraction phase. The same behaviour was observed for the 30000 cSt sample which, even if damaging less during the extraction phase, still largely deformed due to the effect of gravity. For these reasons, it was decided not to test the PMMA samples, and to focus on the MCC ones. The PMMA behaviour could be due to the particular shape of the particles, as previously suggested in §3.3, whose high aspect ratio could reduce the wet granular material strength.

The diametrical testing then focused on the MCC Cp-305 samples and, due to the long preparation and testing phases, it was decided not to analyse the MCC Cp-203 samples. The consolidation stresses chosen for the MCC Cp-102 samples were suitable for the preparation of MCC Cp-305 samples, too. Table 3.7 collects a summary of the testing parameters:

Table 3.7: *Summary of the test parameters for diametrical testing.*

Tested materials	MCC Cp-102 + silicone oil MCC Cp-305 + silicone oil
Consolidation loads	10, 20, 30 kN corresponding to 75, 150 and 225 MPa
Consolidation speed	0.25 mm/s
Consolidation cell	100 kN load cell
Failure speed	From 0.05 to 1 mm/s
Failure cell	100 N load cell

Once the set of consolidation stresses and failure speeds was determined, it was possible to proceed with the systematic testing of the two wet granular materials. As regards the load cells, it was soon noticed that the failure loads were in the range of 1 to 20 N, for which the 100 kN load cell would give too noisy measurements. It was therefore decided to switch to a 100 N one for the failure load evaluation, which would give by far less noisy measurements. Furthermore, the testing procedure was particularly time consuming due to the care that had to be taken to handle the materials, with 4 test taking about one hour to be performed. Indeed, as the Instron® machine had to be used both for the consolidation and for the failure phases, it was decided to first prepare four samples with the 100 kN load cell, then substitute it with the 100 N one and test the four sample before that gravity could cause any relevant deformation. Once the methodology has been defined, the data collection could proceed.

3.4.2 Results collection

The considered materials were tested at different deformation velocities for the three considered sets of consolidation stresses. As a preliminary observation, it should be noticed that the values of consolidation stresses applied in the case of diametrical testing were by far larger than the values used for the uniaxial testing: this was mainly due to the differences between the two machines and to the geometry of the test, which in this case would require a sample solid enough to stand on its external cylindrical surface. Because of this, the two analysis should be considered as focused onto two different operating conditions rather than having a strong theoretical link connecting them. At the same time, the results obtained during the tuning of the consolidation procedure for the diametrical compression highlight an interesting behaviour of wet granular material: even at uniaxial consolidation stresses in the order of MegaPascals, the strength of the cylinder along non-axial directions was really low. Indeed, when the samples consolidated at 5 kN (corresponding to 32 MPa) were positioned on the plane surface, their resilience along the radial direction was so low that they quickly deformed. This behaviour did not show up when they were positioned vertically, during the handling phase. Therefore, this characteristics suggest that only a small percentage of the consolidation stress applied axially improves the radial strength of the wet granular material, which remains particularly week to any external force.

The results collection was obtained through the Bluehill® 3 Testing Software, connected to the Instron® machine. The software was set to register the load applied as a function of time and deformation, which are correlated once the deformation speed is fixed. In this way it has been possible to capture the whole profile of diametrical stresses, eventually evaluating the peak failure stress and any specific stress paths during the deformation. Figure 3.40 shows the profile of stress versus deformation for a MCC Cp-102 plus 500 cSt oil sample tested at 0.05 mm/s.

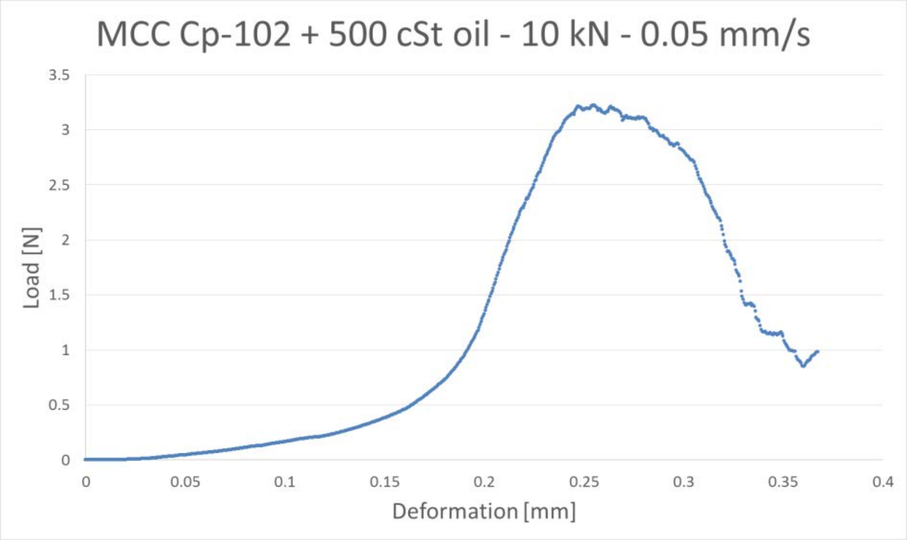

Figure 3.40: *Profile of load versus deformation for a MCC Cp-102 + 500 cSt oil sample, consolidated at 10 kN (75 MPa) and deformed at 0.05 mm/s.*

As can be seen, the load profile started increasing slowly: this could be due to some irregularities in the sample created during the extraction phase, which could deform before the main cylindrical body and cause the instrument to register an initial low load. Nevertheless, as the main body of the sample started to deform, the load rapidly increased up to a peak value: in the considered sample a vertical crack formed and the material started to fail along it, rapidly decreasing its resistance against the deformation.

Some of the experimental tests were filmed to obtain a comparison between the stress profile and the physical behaviour of the material. One of the objectives of the study was indeed to verify the breakage mode of the samples, recognising a plastic, brittle or semi-brittle trend and trying to find a correlation between the stress profile and the corresponding mode. Figure $3.41.a$ shows the stress-deformation behaviour of a MCC Cp-102 plus 500 cSt oil sample, consolidated at 20 kPa and compressed at 0.05 mm/s of deformation velocity. Figure $3.41.b$, $3.41.c$, $3.41.d$ and $3.41.e$ show the images captured at each marked point of the stress profile.

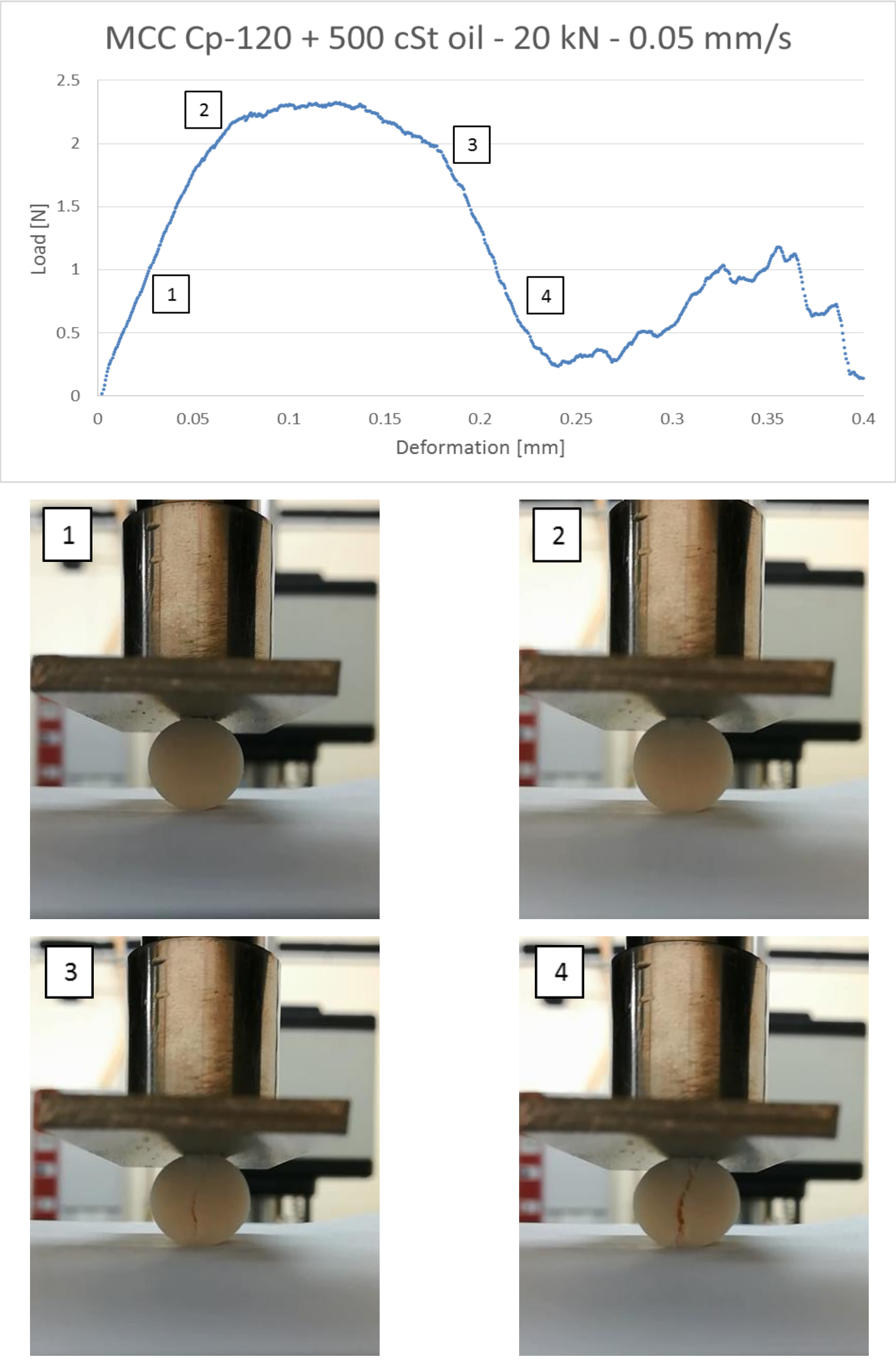

Figure 3.41.a, 3.41.b, 3.41.c, 3.41.d, 3.41.e: *Stress profile vs sample deformation for a MCC Cp-102 + 500 cSt oil sample, consolidated at 20 kN and deformed at 0.05 mm/s (a), with related pictures showing the sample structure (b-e).*

As can be seen the sample in Figure 3.41. *b* does not show any deformation nor damage, and corresponds to the initial phase of compression: the resistance load applied by the sample increases sharply with the deformation, until a breakage plane starts to form in the granular structure. In Figure 3.41. *c* the sample is close to reaching its peak failure stress, and the slope of the stress profile decreases: the compression applied is sufficient to create a preferential plane of breakage. In Figure $3.41.d$ it can be seen how a major crack has formed, and the sample starts to fail along it. The resistance against the deformation rapidly decreases to a minimum, as shown in Figure $3.41.e$, while the two halves of the cylinder rearrange in a more stable position. The sample broke in a typical semi-brittle fashion, with the crack forming almost immediately and the pellet breaking along it, without significantly deforming from the initial structure.

Overall, all the samples tested shown a semi-brittle breakage behaviour at the range of failure speeds available for the Instron® machine. This could be due to the relatively low deformation velocity of the machine, which allowed the formation of cracks through which the material then fails. In the case of higher velocities, the sample would not have enough time to form any crack and would simply deform plastically [8]. From the stress profile of each test it then was possible to evaluate the peak failure stress and its corresponding sample compression: the datasets are shown in Appendix 6.

3.4.3 Results elaboration

The wide dataset collected for the two MCC Celphere™ powders was analysed considering the same parameters studied for the uniaxial compression, and looking for a possible correlation both between the two powders and between the two testing typologies. It should be noticed that the Instron® machine provides the values of peak failure load, which was converted into peak tensile stress with a Brazilian test geometry [45]:

$$\sigma_d = \frac{2 \cdot F_d}{\pi \cdot W_d \cdot d_d} \tag{3.10}$$

where σ_d is the peak tensile stress $[kPa]$, F_d is the peak failure load $[kN]$, W_d and d_d are the sample width and diameter, respectively $[m]$. The analysis performed in this section focuses on this value, which normalizes the sample strength on the sample size.

3.4.3.1 Effect of binder viscosity

During the uniaxial compression analysis it was observed how a higher binder viscosity could increase the strength of a wet granular sample at specific operating conditions. In Figure $3.42.a - d$ the peak tensile stress was represented as a function of binder viscosity for two different deformation velocities, 0.05 and 1 mm/s, at the three consolidation stresses chosen.

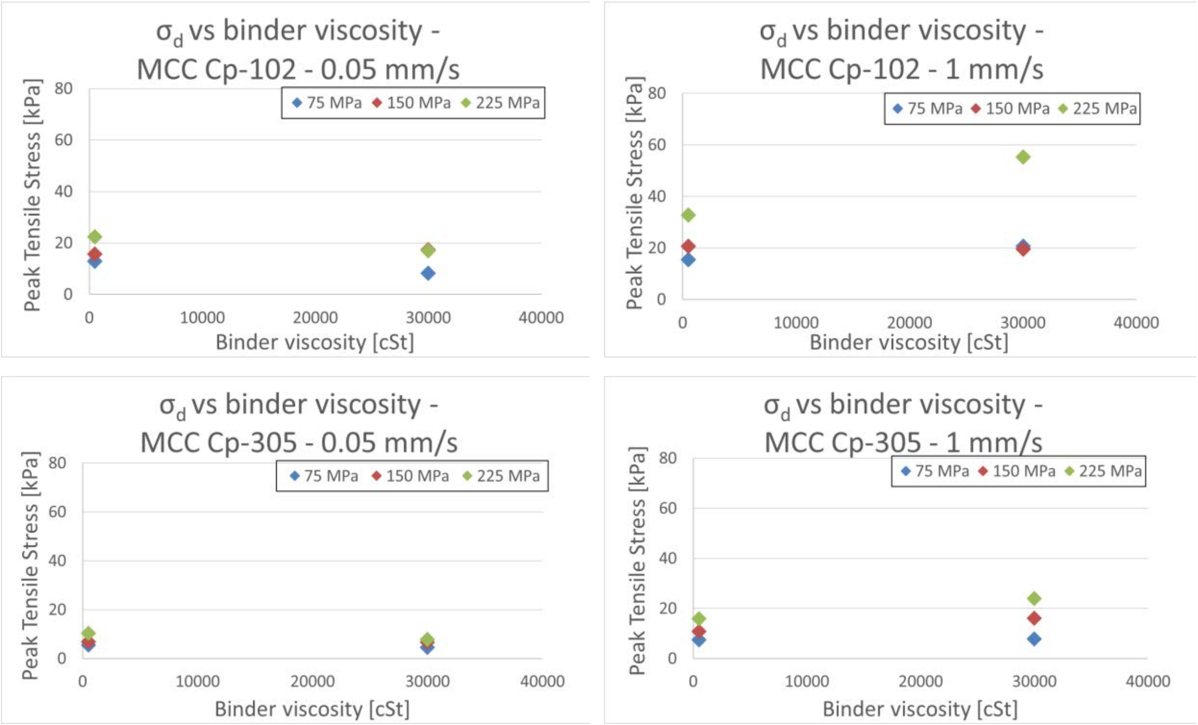

Figure 3.42.a, 3.42.b, 3.42.c, 3.42.d: *Values of peak tensile stress versus binder viscosity for MCC Cp-102 and Cp-305. Measured at 0.05 and 1 mm/s, for samples consolidated at 75, 150 and 225 MPa.*

At low deformation velocities the values of peak tensile stress were almost the same regardless of the binder viscosity, with a slight difference depending on the different consolidation stresses applied: as predicted, the more consolidated samples shown an improved resistance to the deformation. At higher deformation velocities the samples prepared with the low viscosity oil shown the same values of peak tensile stress as the ones deformed at 0.05 mm/s, while the samples using 30000 cSt oil shown an increase in its value. It should also be noticed that the samples prepared with MCC Cp-102 exhibited a value of σ_d more than twice as large as the MCC Cp-305 samples, showing a behaviour similar to the one registered for the uniaxial testing. Indeed it can be seen how the combination of high binder viscosity, high deformation velocity and low particle size correspond to a by far stronger sample, as it was observed in §3.3. The further correlations between different parameters have been analysed in the next sections.

3.4.3.2 Effect of particle size

As it was noticed in §3.4.3.1, given a fixed set of binder and testing conditions a wet granular material shows an improved resistance to deformation when the average particle size is smaller. This mechanism has been further analysed in Figure 3.43. $a - d$:

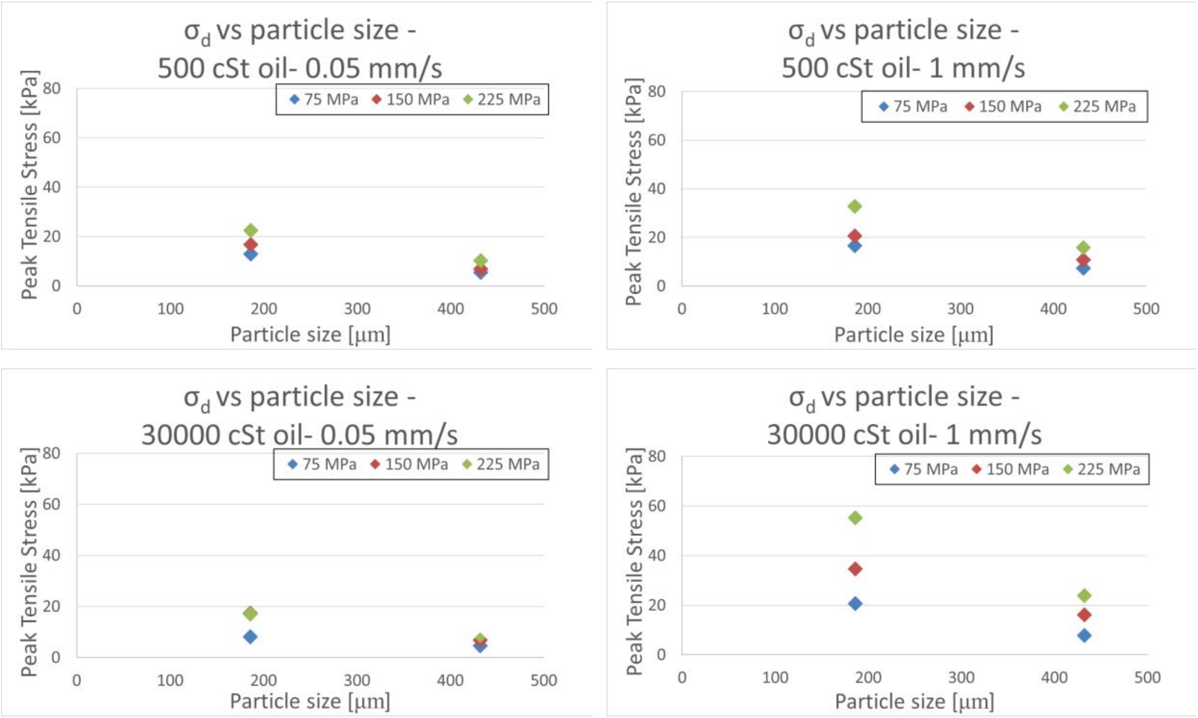

Figure 3.43.a, 3.43.b, 3.43.c, 3.43.d: *Values of peak tensile stress versus particle size for 500 cSt and 30000 cSt silicone oil samples. Measured at 0.05 and 1 mm/s, for samples consolidated at 75, 150 and 225 MPa.*

From the plots above it can be clearly noticed how a lower particle size directly impacts on the wet granular material strength, regardless of the other parameters or operating conditions. As previously explained in §3.3.3.2 the effect of particle diameter is particularly relevant for the evaluation of the capillary forces, and Equation 1.5 highlights how a smaller particle size grants stronger liquid bridges between particles. Furthermore, it can be noticed how the values of peak tensile stress are almost twice as large for MCC Cp-102 when compared to MCC Cp-305, suggesting a direct correlation between its value and the particle size of the powder in exam. This information was taken into account during the modelling phase of §4.2.

3.4.3.3 Effect of deformation velocity

One of the most important and flexible parameters to study was the deformation velocity of the equipment, which was widely varied to cover as many industrial applications as possible. In the case in exam, the Instron® tests were tuned to be performed at velocities spacing from 0.005 to 1 mm/s, which corresponds to the upper limit of the machine. Even if such low deformation speeds are not commonly found in large-scale agglomeration processes, developing and validating a model from which it could be possible to extrapolate the strength of a wet granular material still find large interest for many industrial applications. A more in-depth analysis on the nature of this extrapolation was put during the dimensionless analysis of the next chapters. Figure 3.44.a and 3.44.b show the values of peak tensile stress as a function of deformation speed for MCC Cp-102 mixed with 500 and 30000 cSt silicone oil, respectively, while Figure 3.45.a and 3.45.b represent the values corresponding values for Cp-305. In both cases, the datasets are parametrized on the three consolidation stresses applied.

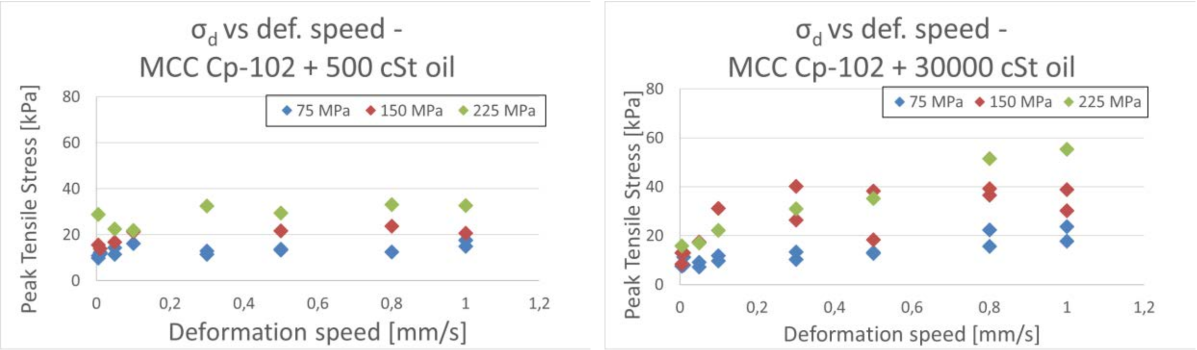

Figure 3.44.a, 3.44.b: *Peak tensile stress of MCC Cp-102 as a function of deformation speed, respectively for 500 and 30000 cSt silicone oils. Parametrized on the consolidation stresses.*

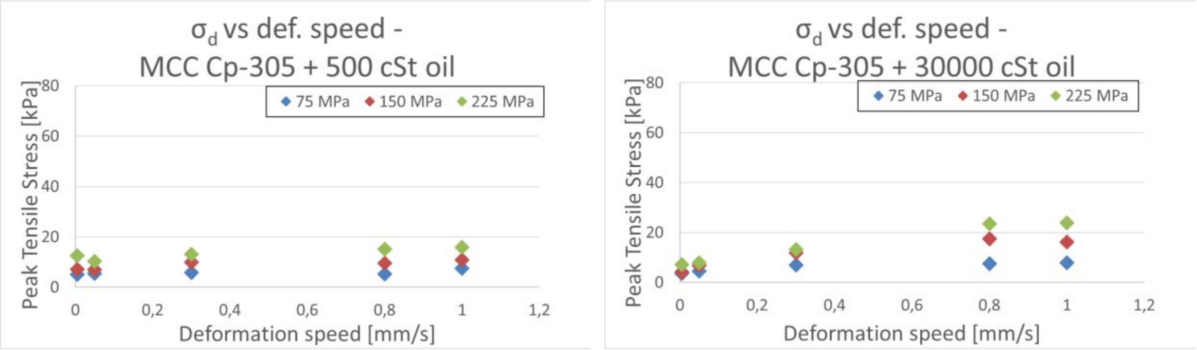

Figure 3.45.a, 3.45.b: *Peak tensile stress of MCC Cp-305 as a function of deformation speed, respectively for 500 and 30000 cSt silicone oils. Parametrized on the consolidation stresses.*

The trend shown by the values of peak tensile strength in the various operating conditions have a shape similar to the ones obtained during uniaxial testing. For smaller particles mixed with low viscosity silicone oil (Figure 3.44.a) indeed the values of granule strength are almost constant in a wide range of operating conditions, regardless of the different deformation velocities. Changing the values of consolidation stress causes the points to traslate accordingly, seemingly by a fixed distance. But when mixed with a high viscosity silicone oil (Figure 3.44.b) the material shown a sharp increase in the values of peak tensile strength, reaching at 1 mm/s of deformation velocity a value of σ_d almost three times larger than the ones measured at 0.005 mm/s. Therefore, it can be deduced that a wet granular material shows an increase resistance to breakage when interested by a combination of high binder viscosity and quick deformation. The effect of different consolidation stresses was still relevant for all the range of velocities, even though the displacement did not look as constant as in the previous case.

MCC Cp-305 shown a similar behaviour, but maintaining its lower values of peak tensile stress, accordingly to its smaller particle size. As for MCC Cp-102, the samples prepared with 500 cSt silicone oil shown a low, constant σ_d at all the testing velocities, with an evident points displacement due to different consolidation stresses. The samples prepared with 3000 cSt silicone oil shown a remarkable increase of tensile peak stress when tested at higher deformation speeds, with the values at the two extremities of the velocities range being almost three times different. In this case the displacement did not look constant but rather dependent on both consolidation stress and deformation speed: the points indeed tended to diverge when going from 0.005 to 1 mm/s of testing velocity, introducing a further degree of analysis in the modelling phase. This possibility was taken into account during the choice of different fitting equations to consider for the final model, as described in §4.2.

As previously mentioned during the uniaxial compression data elaboration, the difference between the aspect ratios of the two powders considered was too small to justify a comparison between the two, and therefore were not considered in this study. The remaining results here obtained, as well as the corresponding observations, were then employed for the model estimation.

3.4.4 Dimensionless analysis of diametrical compression

The next step of the result elaboration phase consisted in the correlation of all the different solid, liquid and testing parameters into some appositely defined dimensionless numbers, from which a comprehensive model could be looked for. The observations of §3.4.3 were initially collected in Table 3.8, taking care of the similarities with the uniaxial case.

Table 3.8: Effect of material and testing parameters on the peak tensile stress.

Higher value of:	Effect
Binder viscosity	At low deformation velocities, the effect is negligible. At high deformation velocities, σ_d increases.
Particle size	The σ_d decreases at any deformation velocity.
Deformation velocity	At low binder viscosity, the effect is negligible. At high binder viscosity, σ_d increases.
Consolidation stress	The σ_d increases but with different trends

Two dimensionless numbers were defined, Str^*_d and Ca_d, described by equations similar to those used in the uniaxial case. The dimensionless peak tensile stress Str^*_d was defined as:

$$Str_d^* = \frac{\sigma_d \cdot d_p}{\gamma \cdot cos\theta} \tag{3.11}$$

where σ_d is the peak tensile stress [Pa], d_p is the particle size [mm], or d_{50} in the case in exam, γ is the binder surface tension [N/m] and θ is the solid-liquid contact angle. The diametrical capillary number was then defined as:

$$Ca_d = \frac{\dot{\varepsilon}_d \cdot \mu \cdot d_p}{\gamma \cdot cos\theta} \tag{3.12}$$

where $\dot{\varepsilon}_d$ is the diametrical strain rate [s^{-1}] defined as the ratio between sample diameter and deformation velocity, and μ is the binder viscosity [Pa*s]. As can be seen, the two dimensionless numbers consider all the parameters modified during the testing phase, with the capillary number focusing on the liquid and testing parameters while the dimensionless peak tensile stress directly depends on the material strength. The consolidation stress does not appear in the definition of the two dimensionless numbers, and its implementation as a factor in the behaviour description was deeply analysed in §4.2. The values of dimensionless peak tensile stress and diametrical capillary number are represented in Figure 3.46.a and 3.46.b for MCC Cp-102 and Cp-305, respectively:

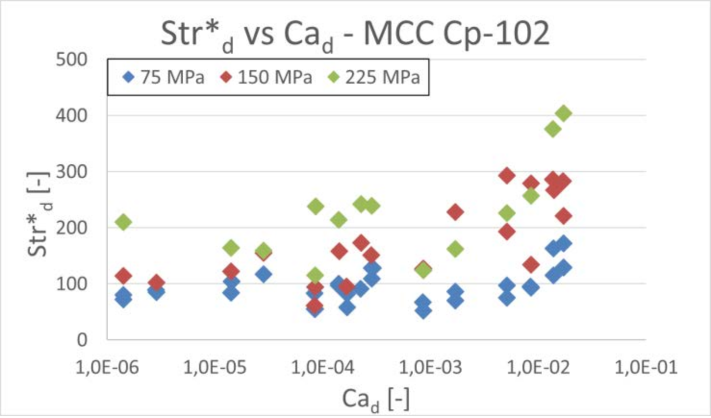

Figure 3.46.a: *Dimensionless peak tensile stress versus Diametrical capillary number for MCC Cp-102, parametrized on the three different consolidation stress.*

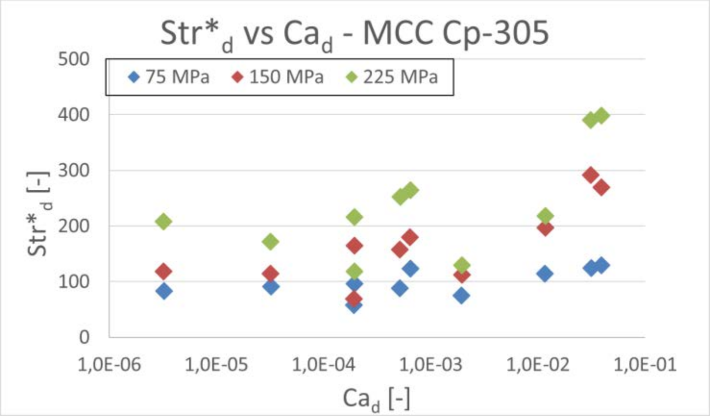

Figure 3.46.b: *Dimensionless peak tensile stress vs Diametrical capillary number for MCC Cp-305, parametrized on the three different consolidation stress.*

The trend obtained is similar to the one observed for the uniaxial compression testing, with the dimensionless peak tensile stress assuming low and almost constant values at capillary numbers below 10^{-3}. The values then quickly increase, almost duplicating at $Ca_d = 10^{-1}$. Furthermore, it should be noticed that the values of Str_d^* are almost one order of magnitude higher than the ones observed in §3.3: given the difference between the two testing typologies there was indeed no reason to expect comparable results. Nonetheless, given the large difference in the consolidation stresses applied in the two cases (100 kPa maximum for the uniaxial compression versus the 225 MPa for the diametrical compression) it could be predicted that the values of Str_d^* would be by far larger. This behaviour suggests that there could be a correlation between the two testing methodologies, for which an equal diametrical and uniaxial strength could be achieved at two different, correlated consolidation stresses once the testing and material parameters are given. Further testing could be performed to evaluate given correlation.

The dimensionless peak tensile stress versus diametrical capillary number trend for the two materials is rather similar and suggests that the correlation between the two dimensionless numbers could actually be independent from solid, liquid and testing parameters. Therefore, all the models analysed in §4.2 were based on a correlation between the two numbers, and further extended to take into account the effect of consolidation stress and aspect ratio.

3.4.5 Fracture Energy and Toughness

Different methods have been defined to analyse the data regarding wet granular material strength. One of them consist in the evaluation of the energy adsorbed by the material up to the failure point, defined as fracture energy E_d, and its comparison with the other testing and material parameters. The Griffith crack theory of fracture [48] defines the fracture energy as:

$$E_d = \int_0^{\varepsilon_{d,f}} \sigma_d d\varepsilon_d \tag{3.13}$$

where ε_d is the sample strain [-], defined as sample compression over initial diameter, and $\varepsilon_{d,f}$ is the strain at the failure point. The integral therefore evaluates the area below the stress-strain curve of the tested material, up to its mode: the failure strain was evaluated from the experimental plots, easily obtained from the Bluehill® software datasets. The value of fracture energy is expressed in Pascals. In Figure $3.47.a$ and $3.47.b$ it is possible to see the values of E_d versus capillary number for both MCC Cp-102 and Cp-305, mixed with the two silicone oils and tested at different velocities:

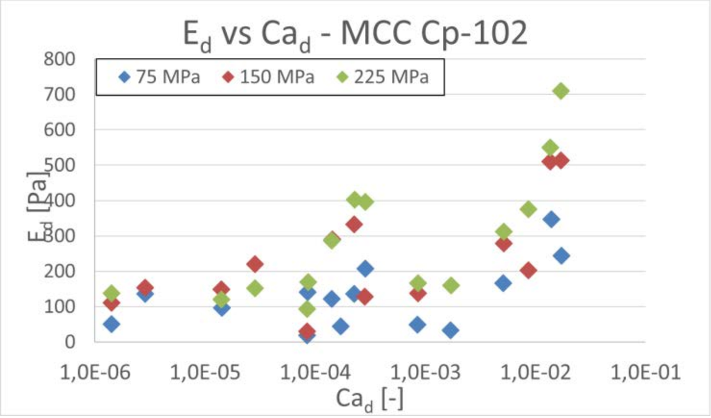

Figure 3.47.a: *Fracture energy vs capillary number for MCC Cp-102, parametrised on the consolidation stress.*

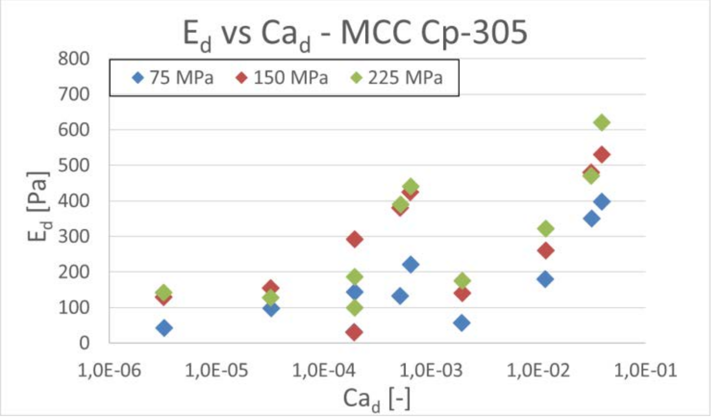

Figure 3.47.b: *Fracture energy vs capillary number for MCC Cp-305, parametrised on the consolidation stress.*

The trend is similar to the one observed for the Str_d^*-Ca_d relationship, with low and constant values of E_d at low diametrical capillary numbers and a sharp increase for values above 10^{-3}. This experimental result is justified by the breakage modes observed during the testing: as all the samples failed in a semi-brittle fashion, it can be assumed that the stress-strain curves of different samples shown similar shapes even when tested at different conditions. Therefore, the values of fracture energy could be considered directly dependent on the peak tensile stress, as the area below the stress-strain curve would only depend on σ_d and no longer on the curve shape. This observation, widely supported by the experimental plots, is particularly interesting as it highlights a direct correlation between fracture energy and capillary number of a given sample, once the failure mode has been observed. Furthermore, the effect of different consolidation stresses was found to influence the values of fracture energy, too, in a similar fashion as for the parameters previously analysed. Nonetheless, the values collected were not normalised on the sample parameters and, therefore, lacked comprehensiveness. One last important detail is that the Instron® machine had difficulties providing measurements quick enough to fully capture the stress-strain behaviour of the material when the testing was carried out at high deformation speed. For this reason, the integral value of Equation 3.12 had a larger error for samples tested at high velocity than for the other ones.

To better compare different formulations of wet granular materials, the fracture energy was made dimensionless in a similar fashion as for the dimensionless peak stress and the capillary number. A new dimensionless number, the dimensionless toughness T_d, was defined as:

$$T_d = \frac{E_d \cdot d_p}{\gamma \cdot cos\theta} \tag{3.14}$$

The values of dimensionless toughness and fracture energy were then studied as a function of the diametrical capillary number, to find out any specific correlation. Figure 3.48 reports all the values obtained from the experimental data elaboration.

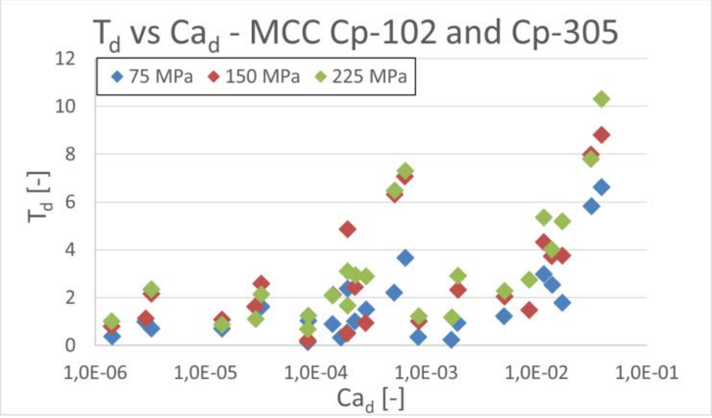

Figure 3.48: *Dimensionless Toughness vs capillary number for MCC Cp-102 and Cp-305. Parametrised on the consolidation stress.*

Apart from a few outliners, the same trend previously observed for the fracture energy and the dimensionless peak tensile stress could be seen for the dimensionless toughness, too. The effect of different consolidation stresses is still evident, even though the points are now by far more randomly distributed due to the large errors on the measurements and the overall difficulty at obtaining regular samples. A particularly interesting detail can be seen for values of diametrical capillary number close to 10^{-3}, which generally marked the difference between the Ca_d of samples prepared with the low viscosity silicone oil and tested at high speed, and the ones prepared with the high viscosity oil and tested at low speed. From Figure 3.48 it is indeed possible to notice a small peak in the value of dimensionless toughness, which could also be seen in the fracture energy plots, after which the curve rapidly decreases and then starts to increase again. This behaviour could indicate that the samples made with low viscosity silicone oil, when tested at high speed, could give values of fracture energy larger than those predicted by previous observations. The peak is not so noticeable in the $Str_d^* - Ca_d$ plots of Figure $3.46.a$ and $3.46.b$, therefore it can be assumed that the main difference is in the shape of the curves rather than on the peak tensile stress values, and thus the fracture energy is different whereas σ_d is coherent. Nonetheless, the amount of experimental points available is not large enough to confirm this behaviour, and further testing may be needed to fully capture this possible irregularity.

3.5 Final experimental considerations

The experimental characterisation and testing of the materials were performed through various issues related to the irregular nature of wet granular materials, and to the difficulties in the handling and testing phases. Overall, the material characterisation has led to a more in-depth understanding of the nature of the materials used, as well as to the expansion of the knowledge of both MCC Celphere™ and Elvacite® 3001 properties. The testing phase was performed having to deal with the various equipment limitations, both regarding the testing parameters and the impossibility to handle some of the materials selected. Nonetheless, a wide and comprehensive set of data was collected for uniaxial and diametrical testing, acting as a solid starting point for any future investigation of the materials considered or of the effect of different parameters on the wet granular strength. The following objectives have been achieved:

- ✓ All the materials were characterised by measuring the particle size and the major shape coefficients (aspect ratio and circularity) and by observing their microscopical structure through both a scanning electron microscope and an optical microscope.
- ✓ The contact angles between the materials and the silicone oils chosen were evaluated experimentally through a drop shape analysis.
- ✓ A consistent and standardized methodology for powder-binder mixing was designed and validated, speeding up the sample preparation phase.
- ✓ Over 300 samples of wet granular materials with different compositions and properties were tested at various deformation speeds and consolidation stresses, both uniaxially and diametrically. The large amount of data collected was elaborated to observe the dependency of granule strength from different material and testing parameters.
- ✓ All the trends between granule strength and other properties have been collected and represented as correlations between dimensionless numbers, looking for a possible model able to describe and predict their behaviour.

Now that the testing phase has been completed, it is possible to take into account the various observations of §3.3 and §3.4 for the design of two experimentally fond models correlating the capillary number and the dimensionless peak stress both for uniaxial and for diametrical testing.

Chapter 4

Modelling

The main objective of the experimental exploration on the dynamic strength of wet granular materials was to fully understand the singular and comprehensive effects of different parameters on the material resistance to compression. The models obtained by previous research groups indeed focused only on the main material and testing parameters, and only on the most easily powders to test. This chapter aims at extending these results, incorporating the datasets obtained for MCC Cephere™ and PMMA Elvacite® 3001 and extending the model to consider also the effect of possible consolidation stresses applied during the handling and processing phases. In particular, the wide experimental analysis of the previous chapter was used for both the model tuning and for its evaluation, while the procedures for data collection implemented proved to be consistent and effective for any future project extension.

4.1 Uniaxial compression modelling

It was chosen to start by modelling the behaviour of wet granular materials undergoing uniaxial compression for a series of different reasons. First of all, the testing procedure has been generally easier and quicker to perform and let less room for measuring errors than the diametrical testing methodology, which resulted to be unreliable for the poly-methyl methacrylate powder. Second, the Advanced Uniaxial Powder Tester allows to test the material at consolidation stresses and deformation velocities that are closer to the ones commonly used in industrial applications: it is indeed possible to test the wet granular samples at velocities up to 5 mm/s (compared to the 1 mm/s of the Instron® machine) and work at lower consolidation stresses, as those more easily obtained in storage conditions. Last and more importantly, all the previous works by Iveson, Smith and Sweat [8, 18, 19, 30, 31] mainly focused on the uniaxial compression of wet granular samples, which provided more consistent results that could be easily fitted with good accuracy by rather simple models. On the other hand, diametrical testing was just considered for the correlations between breakage modes and peak failure stresses, and not looking for specific recurrent characteristics between different parameters. Through diametrical testing it was indeed easier to film and individuate the breakage mode of the samples, which could not be done for the AUPT testing.

4.1.1 Model design

The works of Iveson, Smith and Sweat [8, 18, 31] lead to the formulation of more and more precise models for the prediction of the dynamic strength of wet granular materials, and were based on a wide experimental testing of different granular materials and binders combinations. Nonetheless, as previously mentioned their models did not consider the effect of the consolidation stresses applied during the sample preparation, and therefore worked just in the limited set of consolidation stress that the researchers used. But in §3.3 it was widely observed how the dimensionless peak stress vs capillary number trend was similar between samples tested at different consolidation stresses, and therefore the equations obtained by previous works could still act as a basis for the formulation of a new, more comprehensive model.

In the work of Iveson and Sweat, spherical glass ballottini were mixed with silicone oils with a wide range of viscosities, going up to 2800 Pa*s. The samples were then uniaxially tested with different typologies of Instron® machines, and their dynamic strength values were compared with the material and testing parameters as was done for the AUPT testing in §3.3. The properties considered were binder viscosity, solid particle size and deformation speed applied, all summarised into the capillary number. The model obtained by Iveson [18, 19] and later confirmed by Sweat [31] is reported in Equation 4.1:

$$Str^{*} = a + b \cdot Ca^{c} \tag{4.1}$$

where $a = 5.3$, $b = 280$ and $c = 0.58$. The structure of the model is particularly interesting, with the constant term a evaluated in a way so that it represents the value of Str^{*} at particularly low values of capillary number. At the same time, the terms b is tuned so that it captures the behaviour of the dimensionless peak stress when the value of Ca increases to values close to $10^{-4} - 10^{-3}$. During the experimental testing it was indeed noticed how the values of Str^{*} started to increase at these corresponding capillary number, while they previously maintained a constant, fixed value close to a. Therefore, the choice of b was lead by the requirement to properly fit this behaviour. At higher values of Ca the dimensionless peak stress kept on increasing with an exponential mode, marking a net difference from the previous tendency. The parameter c was individuated from the slope of the curve in a logarithmic plot and, combined with b, modulates the second term of the equation so that its weight becomes relevant only at $Ca \cong 10^{-3}$. At this value of capillary number indeed the viscous effects start to become relevant and the dynamic strength of the wet granular material quickly increases.

In the work of Smith [8] the particle shape started to be considered, too, when it was noticed how wet granular materials prepared with powders of irregular shape (such as lactose) gave plots of dimensionless peak stress that located higher than the values predicted by Equation 4.1.

An irregular particle shape indeed, as mentioned in §3.1, allows a better particle interlocking which improves the solidity and the resistance to deformation of the wet granular sample. The parameter found to better represent this behaviour was the aspect ratio, which was incorporated in Equation 4.1 obtaining:

$$Str^* = AR^d(a + b \cdot Ca^c) \tag{4.2}$$

where AR is the aspect ratio [-], d is equal to -4.3, a is equal to 7, b to 221 and c still to 0.58. The fitting of d was straightforward as a more spherical particle has a larger aspect ratio: a negative exponent was chosen so that for a highly irregular powder gives a larger value of AR^d and, thus, gives the larger dimensionless peak stress experimentally observed. As regards the choice of a and b, the parameters were tuned so that they could still describe the experimental points of previously tested powders when their aspect ratio values were implemented in the equation. Notably, the parameter c was kept equal to the one found by Iveson [18, 19] as the correlation between Str^* and Ca maintained the same exponential slope regardless of the powders tested. In Figure 4.1 it is possible to see a comparison between the two models described, with the Smith's one represented at different aspect ratios:

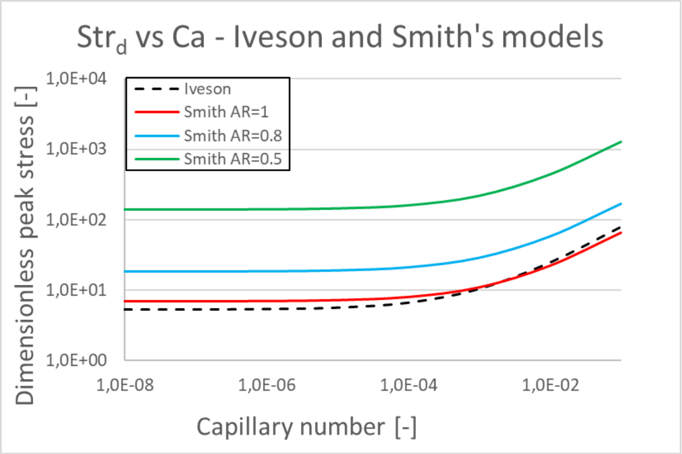

Figure 4.1: *Dimensionless peak stress vs capillary number for Iveson and Smith's models, for different aspect ratios.*

Given all the information retrieved and the considerations regarding the parameters' choice and fitting, the selection of a new model could begin. The main difficulty was related to the choice of how to implement the consolidation stress inside the model, and how many parameters should be implemented to achieve a satisfying fitting. Furthermore, while the works of Smith and Sweat were based on the results previously obtained by Iveson, their datasets could not be used for this project as there was no information regarding the consolidation stresses that were applied for the preparation of their samples. Their datasets would be, indeed, traslated by given amounts depending on the consolidation impressed to the sample during the preparation: not knowing its value, it would be impossible to use it for any model validation. The model design phase thus had to be based just on the experimental data measured for MCC Celphere™ and PMMA Elvacite® 3001.

As all the previous models for the dynamic strength of wet granular materials were based on the correlation between dimensionless numbers, it was decided to introduce the consolidation stress in a similar way. Therefore, a new dimensionless number was defined as “dimensionless consolidation stress” C_s:

$$C_s = \frac{\sigma_1 \cdot d_p}{\gamma \cdot cos\theta} \tag{4.3}$$

where σ_1 is the consolidations stress applied [Pa], d_p is the average particle size, or d_{50} in this case [m], γ is the surface tension [N/m] and θ is the contact angle. The structure chosen is the same as the dimensionless peak stress, considering both particle and solid properties. In this way, it is also taken into account the possible effect that the consolidation stress could have on materials prepared with powders of different size. It should also be noticed that the flow function for the wet granular material, defined as the correlation between σ_c and σ_1, can also be expressed as the correlation between Str^* and C_s. Indeed, as all the other terms get eliminated, the flow function can be expressed independently in dimensionless form or not.

The next phase required to decide which structure the model had to be shaped with, or at least which equations could make sense when implemented for an experimental data fitting. The first characteristic noticed from the plots in §3.3 was that the curves got translated by an amount that looked constant along different values of capillary number. Therefore, the dimensionless consolidation stress could be assumed to act as a traslator for the basic shape of the $Str^* - Ca$ correlation. The most interesting part would be to determine if the traslation effect is directly dependent on the dimensionless consolidation stress or if the dependency has a more complex shape, such as logarithmic of exponential. Nonetheless this dependency would appear as an external addend for the basic core of the model, as a similar shape was noticed for datasets at different consolidation stresses. The initial structure chosen had the following shape:

$$Str^* = (model\ core) + a + b \cdot {C_s}^c \tag{4.4}$$

where a, b and c are parameters that will have to be fitted accordingly to the experimental data. In particular, the constant a has to be fitted so that it properly describes the dynamic strength of the wet granular material when the consolidation is close to zero.

As regards the core structure of the model, different approaches could be taken. But, knowing the previous work of Iveson and Smith [8, 18, 19], it was decided to operate with a similar core:

the curves at different consolidation maintained the same shape and, therefore, there is no reason to change their equation. Furthermore, as the experimental data could not be obtained at capillary numbers higher that 10^{-1}, the choice of using the basic structure of Equation 4.2 is safer and more conservative than trying to fit different equations. Therefore, the chosen structure was:

$$Str^* = (a + b \cdot Ca^c) + d \cdot {C_s}^e \tag{4.5}$$

where a, b, c, d and e are dimensionless and must be fitted on the experimental data. The core part of the model describes the dependency of the dimensionless peak number from the capillary number as was discovered by previous works, and has three parameters that can be tuned to optimally capture the behaviour of the wet granular material when the consolidation stress is fixed. At low capillary numbers ($< 10^{-3}$) the value of Str^* is mainly given by the constant a and by the consolidation stress applied, while as Ca increases a larger and larger part of the peak stress is determined by its value.

One last choice had to be made regarding the effect of the aspect ratio on the final shape of the model. From the work of Smith [8] it could be seen how irregular particles have stronger interlocking effects than spherical ones, and thus give a wet granular material more resistant to deformations. In this case it was required to decide whereas the aspect ratio should appear just connected to the model core (similarly to Equation 4.2) or considered also for the effect it could have on the dimensionless consolidation stress. It makes sense to assume that more irregular particles, when undergoing consolidation, interlock with each other more effectively and, thus, grant the material a larger resistance to deformation. Therefore, it was decided to base the study on the following model structure:

$$Str^* = (a + b \cdot Ca^c + d \cdot {C_s}^e) \cdot AR^f \tag{4.6}$$

The structure is rather general and has a strong theoretical fundament, while the presence of six different parameters allows for a more elastic fitting of the experimental points.

The choice of the number of experimental points was later questioned, as some of them had already been fitted by the previous studies and could be kept used for this analysis, too. The exponent of the aspect ratio indeed had already been found out to be equal to -4.3 by Smith [8] and could be used in Equation 4.6, making the model more consistent with the ones previously developed. A similar concept cold be applied for the choice of the parameter c, which was determined to be equal to 0.58 both by Iveson and Smith. It would therefore make sense to keep it constant, as it was observed from the experimental data that different consolidation stresses should not change the trend of the curve. To perform a comprehensive analysis it was decided to fit and test all different combinations of models and verify which of the previous assumptions provides a more suitable result. The following sets of equations were formulated and tested in 4.1.2:

Model 1: $$Str^{*} = (a + b \cdot Ca^{c} + d \cdot {C_s}^{e}) \cdot AR^{f} \tag{4.7}$$

Model 2: $$Str^{*} = (a + b \cdot Ca^{0.58} + d \cdot {C_s}^{e}) \cdot AR^{f} \tag{4.8}$$

Model 3: $$Str^{*} = (a + b \cdot Ca^{c} + d \cdot {C_s}^{e}) \cdot AR^{-4.3} \tag{4.9}$$

Model 4: $$Str^{*} = (a + b \cdot Ca^{0.58} + d \cdot {C_s}^{e}) \cdot AR^{-4.3} \tag{4.10}$$

Model 5: $$Str^{*} = (a + b \cdot Ca^{0.58} + d \cdot C_s) \cdot AR^{-4.3} \tag{4.11}$$

As can be seen, Model 1 is the most generic one, with 6 parameters that can be modified accordingly with the necessities of the fitting. Model 2 and 3 use one fixed parameter each obtained from the previous works of Iveson and Smith, while Model 4 implements both assumptions. Model 5 on the other hand uses both assumptions plus a further consideration noticed from §3.3.3.2 and §3.3.5: in the representation of the flow functions for different compositions of wet granular materials, the trend was generally linear in the range of consolidation stresses used for the testing (such as can be seen in Figure 3.33). Therefore, it could be assumed that the dependency between dimensionless peak stress and dimensionless consolidation stress is linear once the capillary number is fixed: the parameter e could thus be set equal to 1. It should also be noticed that other different models were designed at tested, introducing more complex correlations between Ca and C_s, but the fitting was not satisfying in most cases and lacked any solid theoretical base. The equations proposed in models $1-5$ on the other hand have a strong theoretical fundament and gave a more satisfying representation of the experimental points.

4.1.2 Model fitting and validation

The five selected models were fitted on the experimental data for each of the four materials. The procedure was carried out using the *cftool* tool in the MATLAB® software, as it allows a quick and flexible setup while still granting a satisfying choice of possible robustness models and algorithms. Furthermore, given the large amount of data that had to be processed from Excel spreadsheets, it was particularly effective to directly process the data with the tool rather than setting up an effective MATLAB® script.

The fitting was initially carried out for the four materials separately, to better understand which model granted a higher R-square and, thus, a better fitting of the experimental data. The values of SSE (Sum of the Square Errors) was evaluated by the tool, too, and reported as a second statistical parameter to evaluate the fitting quality. As regards the fitting method, the *Nonlinear Least Squares* was implemented by MATLAB® by default and leaving the possibility to choose the robust and the algorithm for the fitting. The number of function evaluation, the initial guess and the parameters ranges could be set, too, as well as the tolerance on the errors. Different combinations of methods, algorithms and fitting options gave as a result different parameters, and the choice was based on which one was providing the highest R-square. In Tables 4.1 to 4.4 the parameters obtained and the statistical indicators were reported for each material and each model tested, while the fitting structure can be found in the last column. The legend below explains the corresponding setup. As regards the initial guesses and possible intervals, all the parameters except f had to be positive in order to maintain the physical meaning of the model: any negative value would have meant that an increase in Ca or C_s could reduce the value of Str^*, which is illogical. At the same time, no positive value of f could be accepted otherwise the model would claim that wet granular material made with more spherical particles would show a larger resistance to deformation, which contradicts all the previous observations.

Table 4.1: *Fitted parameters and statistical indicators for the MCC Cp-102 dataset of uniaxial tests.*

	a	b	c	d	e	f	R-square	SSE	Structure
Model 1	2.102	188.2	1.121	0.010	0.818	-3.471	0.921	27.20	2
Model 2	2.666	27.62	**0.58**	0.008	0.886	-2.038	0.917	29.68	3
Model 3	1.571	84.10	0.958	0.020	0.705	**-4.3**	0.983	5.948	1
Model 4	1.741	18.15	**0.58**	0.0056	0.882	**-4.3**	0.919	28.93	4
Model 5	1.861	18.15	**0.58**	0.0024	**1**	**-4.3**	0.922	29.07	1

Table 4.2: *Fitted parameters and statistical indicators for the MCC Cp-203 dataset of uniaxial tests.*

	a	b	c	d	e	f	R-square	SSE	Structure
Model 1	1.586	13.43	0.591	0.0031	0.923	-5.308	0.963	5.981	2
Model 2	2.464	20.02	**0.58**	0.0051	0.915	-2.743	0.969	4.913	1
Model 3	1.891	16.01	0.591	0.0037	0.923	**-4.3**	0.970	4.794	1
Model 4	1.878	15.26	**0.58**	0.0039	0.915	**-4.3**	0.977	3.659	1
Model 5	1.959	15.57	**0.58**	0.0021	**1**	**-4.3**	0.985	2.368	1

Table 4.3: *Fitted parameters and statistical indicators for the MCC Cp-305 dataset of uniaxial tests.*

	a	b	c	d	e	f	R-square	SSE	Structure
Model 1	3.263	29.49	0.618	0.0016	1.079	-2.013	0.984	4.971	3
Model 2	3.077	25.02	**0.58**	0.0016	1.071	-2.257	0.984	4.943	4
Model 3	2.202	18.45	0.599	0.0012	1.059	**-4.3**	0.981	6.006	2
Model 4	2.151	17.54	**0.58**	0.0011	1.069	**-4.3**	0.985	4.648	3
Model 5	2.044	17.58	**0.58**	0.0019	**1**	**-4.3**	0.986	4.305	3

Table 4.4: *Fitted parameters and statistical indicators for the PMMA dataset of uniaxial tests.*

	a	b	c	d	e	f	R-square	SSE	Structure
Model 1	1.008	49.73	0.537	0.100	0.391	-2.038	0.979	11.89	3
Model 2	1.023	58.69	**0.58**	0.155	0.339	-2.088	0.983	9.463	4
Model 3	1.098	35.32	0.539	0.010	0.663	**-4.3**	0.983	9.395	3
Model 4	1.035	41.45	**0.58**	0.029	0.492	**-4.3**	0.988	6.814	2
Model 5	1.276	41.70	**0.58**	0.0010	**1**	**-4.3**	0.993	4.242	1

Structure legend:

1 - Robust: LAR, Algorithm: Trust-Region

2 – Robust: LAR, Algorithm: Levenberg-Marquardt

3 – Robust: Bisquare, Algorithm: Trust-Region

4 – Robust: Bisquare, Algorithm: Levenberg-Marquardt

It can be clearly seen how the most effective model at fitting the experimental data is Model 5 for three cases out of four, with a particularly high R-squared for the PMMA samples. The values of R-square for the MCC Cp-102 samples are generally lower, maybe due to some errors during the initial AUPT investigation phase that could give a less regular distribution of the points. The fitting is still acceptable, as values of R-square above 0.90 can already be considered acceptable for an empirical model. Values above 0.95 instead indicate an optimal fitting, especially if paired with a low SSE as is generally achieved with the Model 5. It is particularly interesting to see how this less flexible three-parameters model works better than the others, even though more parameters are usually associated with an improved fitting. This behaviour could be due to a sub-optimal choice of the initial guesses, or to a difficulty of the fitting model to find the optimal convergence. Nonetheless Model 5 has a strong theoretical basis, implementing two parameters from previous works that extensively analysed a wide range of wet granular materials. Furthermore, the assumption on which the choice of the parameter $e = 1$ is based is further justified by a higher R-square than Model 4 and, thus, can be considered as confirmed in the range of operating conditions chosen for the experiment.

As a further analysis, it was decided to fit the five models to a common dataset containing all the experimental results from the four materials tested. The methodology used was the same as the one implemented for the results of Table $4.1 - 4.4$, and the parameters obtained can be seen in Table 4.5.

Table 4.5: *Fitted parameters and statistical indicators for all the datasets of uniaxial tests.*

	a	b	c	d	e	f	R-square	SSE	Structure
Model 1	3.263	29.49	0.618	0.0016	1.079	-2.013	0.984	4.971	3
Model 2	3.077	25.02	**0.58**	0.0016	1.071	-2.257	0.984	4.943	4
Model 3	2.202	18.45	0.599	0.0012	1.059	**-4.3**	0.981	6.006	2
Model 4	2.151	17.54	**0.58**	0.0011	1.069	**-4.3**	0.985	4.648	3
Model 5	2.044	17.58	**0.58**	0.0019	**1**	**-4.3**	0.986	4.305	3

All the models proposed accurately fitted the experimental datasets, each with a high R-square and a low SSE. Model 5 once more proves to be the optimal choice, and further justifies the assumption of the linear flow function. Furthermore, the parameters are rather similar to the ones determined for each single material, and thus it was decided to use this final equation for the model:

$$Str^* = (2.04 + 17.6 \cdot Ca^{0.58} + 0.0019 \cdot C_s) \cdot AR^{-4.3} \tag{4.12}$$

The model and the experimental points can be seen in Figure 4.2:

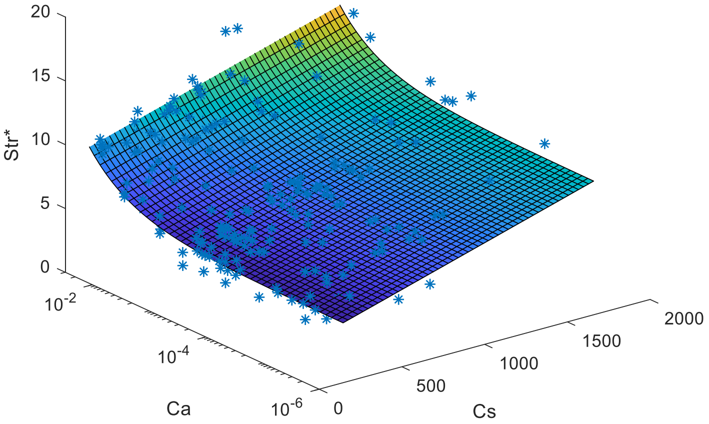

Figure 4.2: *Dimensionless peak stress vs capillary number and dimensionless consolidation stress. Experimental points and fitted model.*

For a more effective representation it was decided to represent Equation 4.12 in a single 2D plot. The model was therefore rewritten as:

$$f(Str^*, C_s) = Str^* - 0.0019 \cdot AR^{-4.3} \cdot C_s = (2.04 + 17.6 \cdot Ca^{0.58}) \cdot AR^{-4.3} \tag{4.13}$$

and represented graphically for each of the four materials. The percentual errors for each dataset were represented graphically, too. Figure $4.3.a$ to $4.3.h$ show the corresponding plots:

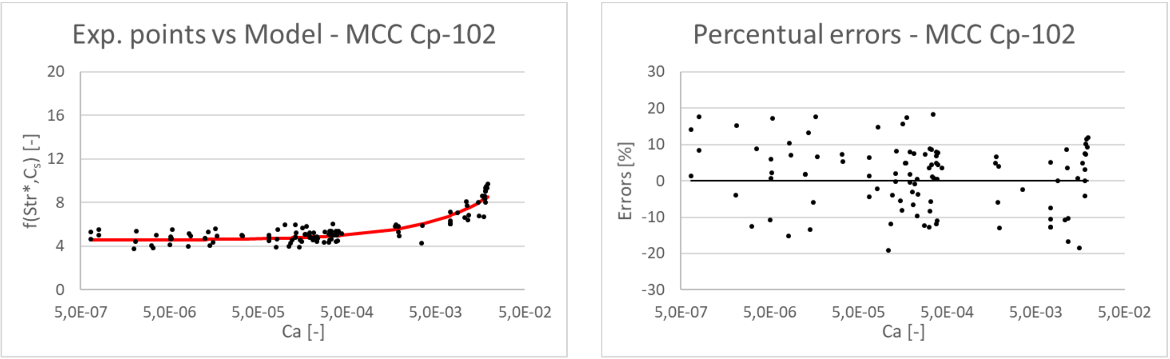

Figure 4.3.a, 4.3.b: *Experimental points vs model curve for MCC Cp-102 (a); percentual errors between model and experimental points (b).*

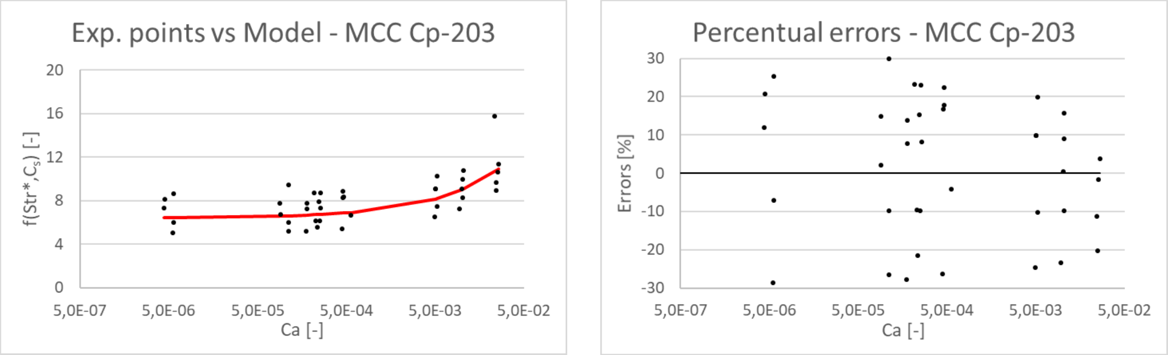

Figure 4.3.c, 4.3.d: *Experimental points vs model curve for MCC Cp-203 (c); percentual errors between model and experimental points (d).*

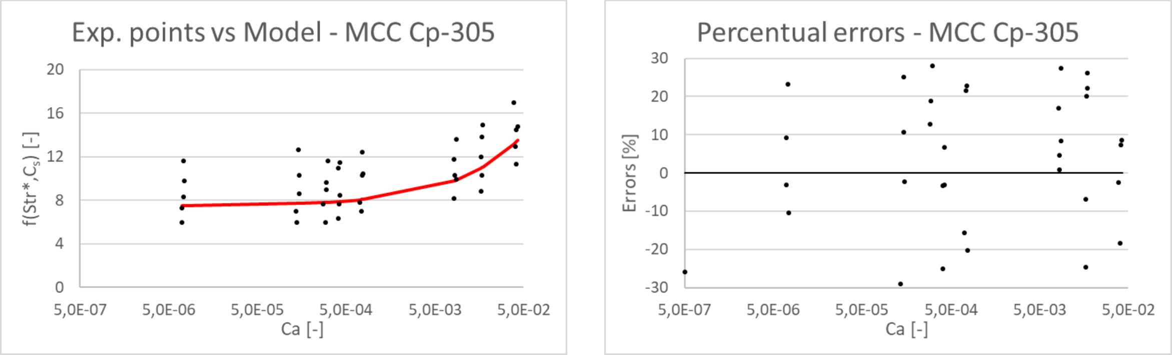

Figure 4.3.e, 4.3.f: *Experimental points vs model curve for MCC Cp-305 (e); percentual errors between model and experimental points (f).*

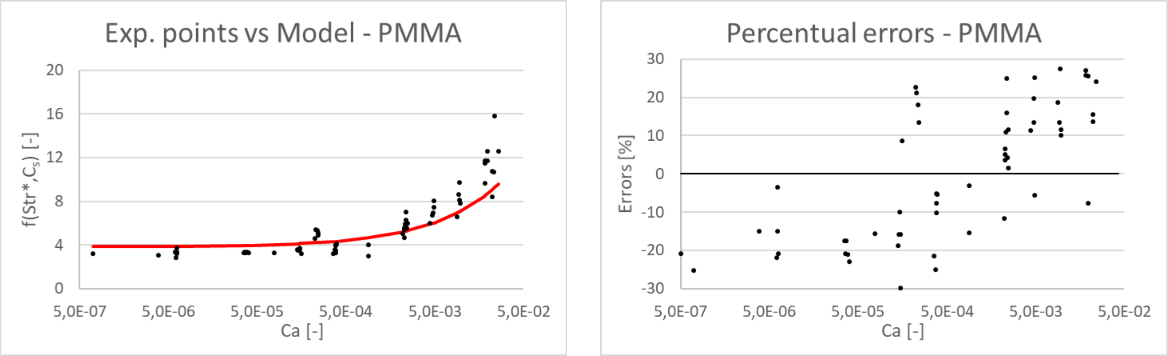

Figure 4.3.g, 4.3.h: *Experimental points vs model curve for PMMA (g); percentual errors between model and experimental points (h).*

It can clearly be seen how the model nicely represents the four datasets of experimental points, with an improved fitting for MCC Cp-102 and PMMA. The fitting for MCC Cp-203 and Cp-305 is still satisfying but could be influenced by the large impact of the errors in the measurement of σ_c with the AUPT machine. Indeed, as their values of failure stress are generally lower than the other two materials (due to the larger particle size), any mistake on the measurement has a larger impact on the final value of Str^*. This is due to the amplifying effect that an incorrect measurement undergoes when its dimensionless peak stress is evaluated with Equation 3.7, as σ_c gets multiplied for the particle size: the larger the particle size, the more the error on Str^* increases. Therefore, the distribution of the experimental points tends to spread out more giving the results observed in Figure $4.3.c$ and $4.3.e$.

Another important result is the fact that the errors distribute uniformly on the whole range of capillary numbers for all the four materials. This statistical characteristic highlights how the model is able to capture the experimental behaviour in the whole range of Ca, and further supports the quality of the fitting. One last observation that should be made is that only the initial section of the change of trend corresponding to $Ca \cong 10^{-3}$ can be captured experimentally, due to the equipment limitations. Therefore, the model parameter b could require a more precise fitting once more experimental points at higher capillary numbers are available. This could be achieved with an AUPT machine able to compress the samples at larger velocities, which is not currently available.

This said, it is clear how the behaviour of the wet granular materials analysed is optimally captured by the model formulated, whose equation is both based on the results of previous works and on information obtained during the experimental and computational analysis. Moreover, given the model structure the prediction of the dynamic strength of the wet granular material is quick and does not require specific calculations. An improved fitting quality could surely be achieved with the testing of other wet granular materials, especially as regards parameter a and e as they are the ones not confirmed by previous experimental analysis. Nonetheless, the quality of the experimental investigation has been confirmed by the comparison of the results with other studies [8, 18, 19] and suggests how the usage of the AUPT machine is more effective and efficient when compared to the use of an Instron® machine.

One more interesting application of the model could also involve the estimation of the level of consolidation of a wet granular material in storage or handling conditions. If the solid particle size and the binder properties (viscosity, surface tension, liquid-solid contact angle) are known, it is possible to measure the failure stress σ_c of the material through an AUPT or Instron® machines, applying a very low consolidation stress. The values of Ca and Str^* could then be easily calculated and, substituting them in Equation 4.12, it would be possible to extrapolate the corresponding value of C_s. Therefore, if it is required to evaluate whereas a given material in given operating conditions undergoes consolidation (due to vibration effects, compression or even particle rearrangement over time), a consistent result could be evaluated through a quickly uniaxial failure test and the model fitted by this study. It should be noticed that the knowledge of the capillary number is required for this estimation, as different values of Ca seem to provide different flow functions: see the analysis of §4.1.3 for more details on this topic.

One last, important point is the flexibility of this analysis. It has been mentioned many times how the dynamic strength of the wet granular materials depends on the capillary number, which contains the product between the binder viscosity and the strain rate of the deformation. One main issue of this experimental investigation was the limitation on the maximum deformation speed achievable with the AUPT machine, which was lower than the velocities used by previous studies. Therefore, the capillary numbers of the samples could not be as high as if tested with the equipment used in those works. But choosing a silicone oil with high viscosity it was possible to compensate this deficiency: a sample prepared with the 30 Pa*s silicone oil indeed and tested at 5 mm/s has the same capillary number of a sample of the same granular material mixed with a 0.3 Pa*s silicone oil and tested at 500 mm/s. The Ca indeed depends on the product between viscosity and deformation speed, and therefore Equation 4.12 is able to be used also for samples undergoing extremely high strain rates, such those used in agglomeration processes. In this way it is possible to use it to predict the dynamic strength for a wide range of materials and operating conditions, as long as they are inside the boundaries of consistency of the model. The counterpart is indeed that the model fitted in this work has been validated only for capillary numbers up to 10^{-1}, and therefore it should not be used to try to predict the behaviour of wet granular materials with particularly large binder viscosity or deformed at high speed. Any extrapolation of the dynamic strength outside the model boundaries should not be carried out, especially for capillary numbers that exceed for more than one order of magnitude.

4.1.3 Flow Function

It was already observed in §3.3.5 how different testing velocities provided different plots of the flow function (FF) for the same wet granular material. Furthermore, it was also noticed how a similar effect was achieved in some cases by changing the binder viscosity once the deformation speed was fixed: the flow function therefore seems to be related to these two parameters, whose modifications lead to different flowability characteristics for the materials. Both parameters appear in the definition of capillary number, therefore it was decided to widely analyse the interaction of failure stress (or uniaxial unconfined yield stress uUYS) with both the consolidation applied and the capillary number of the sample. The main objective is to determine if and how a modification of the capillary number causes significant changes in the behaviour of the flow function, and if it would be possible to predict it. It was decided to consider both uUYS and the consolidation stress σ_1 with their dimensionless forms, Str^* and C_s respectively. From their definition indeed their correlation does not change once the stresses become dimensionless, and this choice allows to consider for the analysis the model shown in Equation 4.12. The model indeed correlates Str^* with both C_s and Ca, and has already been validated with the experimental data in §4.1.2. Therefore, it was assumed to be fully adequate for the description of the materials considered, at least in the range of operating conditions used for the current testing.

The first thing that was noticed was that once the solid material and the binder are chosen, the values of particle size, particle aspect ratio, binder viscosity, binder surface tension and the solid-liquid contact angle are fixed. Equation 4.12 thus becomes:

$$c_1 \cdot \sigma_c = [2.04 + 17.6 \cdot (c_1 \cdot \mu \cdot \dot{\varepsilon})^{0.58} + 0.0019 \cdot c_1 \cdot \sigma_1] \cdot c_2 \tag{4.14}$$

Where σ_c is the uniaxial unconfined yield stress uUYS [Pa], μ is the binder viscosity [Pa*s], $\dot{\varepsilon}$ is the strain rate [s^{-1}], σ_1 is the consolidation stress [Pa], c_1 is a constant for the solid-binder choice, equal to $d_p/(\gamma \cdot cos\theta)$ [Pa^{-1}], c_2 depends on the aspect ratio of the solid particles and is equal to $AR^{-4.3}$. Dividing both sides for c_1 and collecting all the constant terms, Equation 4.14 becomes:

$$\sigma_c = k_1 + k_2 \cdot \dot{\varepsilon}^{0.58} + k_3 \cdot \sigma_1 \tag{4.15}$$

where k_1, k_2 and k_3 depend on solid and liquid properties. In particular:

$$k_1 = \frac{2.04 \cdot AR^{-4.3} \cdot \gamma \cdot cos\theta}{d_p} \qquad [Pa] \tag{4.16}$$

$$k_2 = 17.6 \cdot \mu^{0.58} \cdot \left(\frac{\gamma \cdot cos\theta}{d_p}\right)^{0.42} \cdot AR^{-4.3} \qquad [Pa \cdot s^{0.58}] \tag{4.17}$$

$$k_3 = 0.0019 \cdot AR^{-4.3} \qquad [\text{-}] \tag{4.18}$$

From Equation 4.15 it can clearly be seen how the uUYS can be expressed just as a function of two parameters, the consolidation stress applied and the strain rate used during the test. The strain rate specifically depends on the height of the sample, which is fixed when working with the AUPT machine, and on the deformation velocity chosen for the test. The result is particularly interesting as it highlights how the shape of the uUYS-σ_1 correlation does not depend just on the material properties, as it was previously believed, but also on the testing velocity. The same wet granular material therefore would give two different flow function equations if tested at two different deformation velocities: this means that there is not an unique flow function for a wet granular material, but that it may behave differently depending on the dynamics of the system. Indeed, once the strain rate is fixed, Equation 4.15 becomes:

$$\sigma_c = k_4 + k_3 \cdot \sigma_1 \tag{4.19}$$

with $k_4 = k_1 + k_2 \cdot \dot{\varepsilon}^{0.58}$, in Pa. This result is extremely important as it summarizes the flow function for the material in just one simple equation, whose parameters can be easily calculated from the powder and binder literature data and from the velocity chosen for the test. Furthermore, it allows to **predict** the flow function from uniaxial test for a wet granular material without having to measure it experimentally, saving a large amount of time and money. One further detail should be noticed from Equation 4.19: due to the assumptions made in §4.1.2 regarding the value of the parameter e, the correlation between uUYS and σ_1 is a straight line. The assumption has proved to be suitable for the materials studied, but if the analysis will be extended to a larger set of wet granular materials it may be required to modify its value to better fit the new experimental data. Nonetheless, this modification would not deny the result here presented but just change Equation 4.19 to incorporate an exponent for σ_1, changing the shape of the flow function but not its predictability.

To validate the results obtainable from Equation 4.19 it was decided to compare the predicted flow functions with the experimental ones: in Figure $4.4.a$ $4.4.d$ it is possible to see the difference between the two for MCC Cp-203 plus the low viscosity silicone oil at four different testing velocities. The corresponding four strain rates could have small fluctuations in their values due to the slight difference in the height of the samples, as mentioned in §3.3.

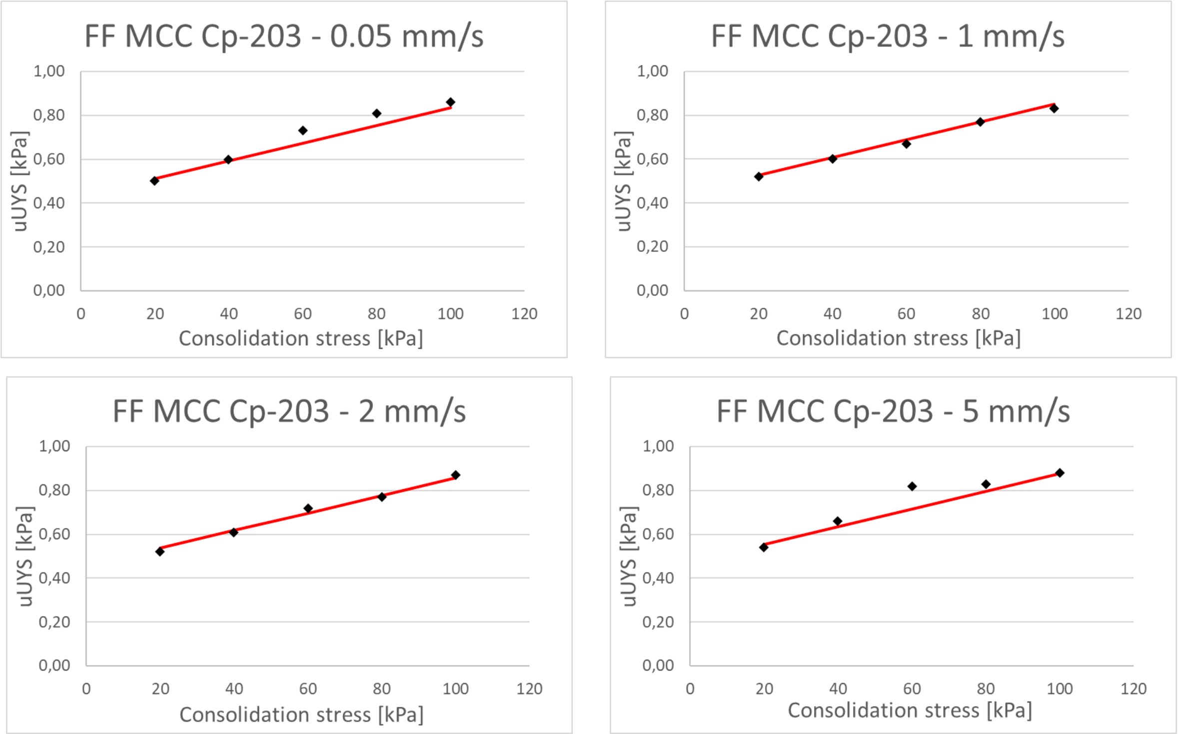

Figure 4.4.a, 4.4.b, 4.4.c, 4.4.d: *Flow function of MCC Cp-203 plus 500 cSt silicone oil, experimental points vs predicted line. At 0.05 (a), 1 (b), 2 (c) and 5 (d) mm/s of deformation speed, corresponding to strain rates of 0.0011, 0.022, 0.041 and 0102 s*$^{-1}$.

As it can be seen, the model fits the experimental results with high accuracy, confirming the assumptions on its capability of predicting the flow function of the wet granular materials analysed. It can therefore be assumed that the model is able to predict the flow function of a wet granular material just from its basic physical characteristics and from the testing parameters, without the need of carrying out any experimental evaluation. The amount of time saved is unbelievably large, as the calculation setup took only a few minutes compared to the $5 - 10$ required for each AUPT testing.

But there is no large difference between the flow functions at the four deformation velocities. Indeed, the magnitude of the changes in the flow function due to different velocities widely varies based on the operating conditions of the test. In particular, it would be interesting to see which combinations of testing speed and binder viscosity could cause the *FF* to largely change from one set of operating conditions to the other, as for the cases in Figure $4.4.a - 4{,}4, d$ the difference is almost negligible. To better deal with this analysis, it was decided to work with the dimensionless numbers: in this way the analysis no longer depends on the k_1, k_2, k_3 and k_4 of the single material but on more general parameters. It has already been mentioned how the capillary number depends on the product between binder viscosity and strain rate of the deformation, which have been individuated to be the main parameters influencing the shape of the flow function. Therefore, for a fixed value of capillary number, Equation 4.12 becomes:

$$Str^* = AR^{-4.3} \cdot (n + 0.0019 \cdot C_s) \tag{4.20}$$

with $n = (2.04 + 17.6 \cdot Ca)$. The equation is the same flow function as 4.19 but expressed in dimensionless numbers and, therefore, the parameter m just depends on the already fixed capillary number. It was then represented parametrised for different capillary numbers, to fully capture where the increase in magnitude becomes remarkable. Figure 4.5 reports the analysis:

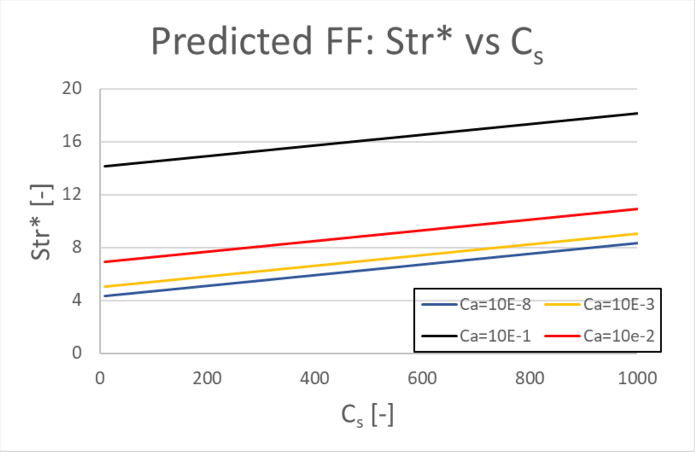

Figure 4.5: *Predicted dimensionless flow function for different values of capillary numbers. Aspect ratio fixed equal to 0.84.*

The dimensionless flow functions evaluated for $Ca = 10^{-7}$ up to $Ca = 10^{-4}$ were almost impossible to distinguish one from the other and, therefore, not reported in the plot. Nonetheless, as soon as the capillary number gets closer to 10^{-3} the lines start to diverge more and more, following the exponential law that relates the dimensionless peak stress to the capillary number. For such high Ca indeed the viscous effects start to become predominant and influence the flow function of the material, too, which rapidly becomes more and more resistant to deformation without having to apply a larger consolidation. This behaviour could even be predicted from Figure 4.2 by observing how the $Str^* - C_s$ changed along different planes at fixed Ca: the curve initially remains constant at low capillary numbers, and then starts to shift getting closer to $Ca = 10^{-3}$. This result is particularly important as it shows how the flow function is highly dependent on the viscous effects inside the wet granular material, mainly related to the binder viscosity and the deformation speed, and not only to the solid and interaction properties.

This result also sets a new obstacle on the characterisation of the flow function of wet granular materials: a given sample indeed could provide different *FF* when tested at different conditions, in particular when its resulting capillary number is already large. For example, considering an uniaxial test with a dimensionless consolidation stress equal to 200, a wet granular material that has a capillary number equal to 10^{-3} when tested at 0.05 mm/s will give, when tested at 5 mm/s, a value of Str^* that is almost 4 times larger. The correlation traslates in dimensional parameters, with an uUYS that is four times larger. Any further calculation of the flow function would thus be unreliable, providing different equations. This issue is particularly relevant in the industrial practice, too, where different equipment or different test setups could easily cause the measurements of the flow function to not comparable one with the other. Nonetheless, it should be noticed that the shifting effect of Figure 4.5 appears only at particularly high capillary numbers: no major differences between the *FF* appear when testing materials having a $Ca < 10^{-3}$, which corresponds to the majority of the samples of wet granular materials used industrially.

One more time it should be reminded how these results have proven to be highly representative of the wet granular materials chosen for the study, but that particular care should be used in extrapolating them for describing other combinations of solids and binders. The study has indeed proven to be effective for generally regular particles, with medium-high aspect ratios and high wettability by the binders chosen. The equipment availability set more restricted limits for the experimental analysis, too, diminishing the comprehensiveness that the study aimed to reach. Only when more materials will be tested and the model's parameters will be tuned accordingly, the model would be considered validated and fully used for its purpose of predicting the wet granule strength and its flow function.

To sum up, the elaborations in this section have provided an effective and theoretically fond empirical model able to predict both the dynamic strength and the flow function of a wet granular material just knowing some basic physical parameters and the deformation speed applied. The statistical investigation proved the quality of the model as well as its effectiveness in the whole range of operating conditions available for the experimental analysis, further justifying the assumptions used for the model design. Last but not least, the concept of flow function of a wet granular material has been reconsidered in the light of the results of §4.1.2, highlighting its weaknesses in correlation with the capillary number.

4.2 Diametrical compression modelling

The diametrical compression tests performed did not provide a clear correlation between the failure stresses and the consolidation applied at different capillary numbers, especially if compared to the uniaxial compression tests. Furthermore, the previous study by Smith [8] could not find a model for the correlation between Str_d^* and Ca_d, and focused just on the failure mode of the samples. The objective of this section will thus be to design and possibly validate a new model correlating these two dimensionless numbers with the dimensionless consolidation stress C_s, hopefully obtaining a suitable equation. The focus will then switch to the correlations of fracture energy E_d and dimensionless toughness T_d with the diametrical capillary number.

4.2.1 Model design and validation for the dimensionless peak stress

The wide analysis of §3.4.4 allowed to evaluate and represent the correlation between the diametrical dimensionless peak stress and the diametrical capillary number, parametrised on the consolidation stress, for the four possible combinations of MCC Cp-102, Cp-305 and silicone oils. The distribution of the points is wide, both due to the difficulties in preparing the samples and to the experimental errors. In Figure 4.6 it is possible to see the general results.

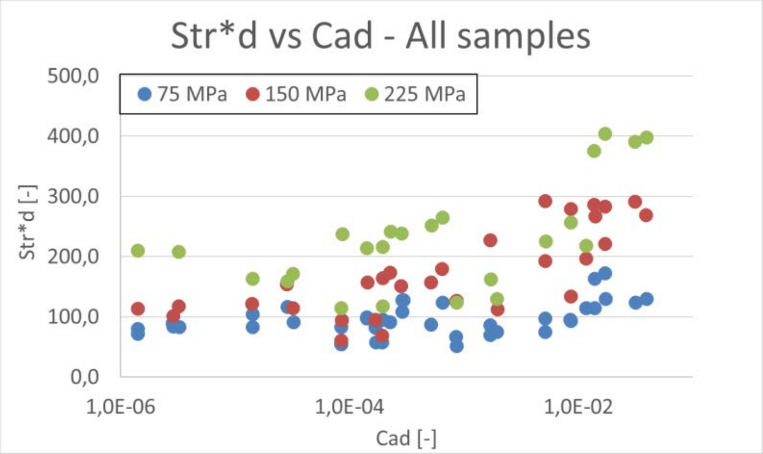

Figure 4.6: *Dimensionless peak stress vs capillary number for the diametrical testing of MCC Cp-102 and Cp-305, all the samples. Parametrised on the consolidation stresses.*

It can be clearly seen how the points distribution still maintains a general shape, similar to the one observed during the uniaxial testing, with an almost constant initial value that rapidly increases when $Ca_d \cong 10^{-3}$. The effect of different consolidation stresses can still be seen, even if not so evidently at higher capillary numbers (thus for samples prepared with the high viscosity oil and tested at high speeds), while the actual loads applied are by far larger than the corresponding ones in the uniaxial compression tests. Given these observations it was decided to proceed with a similar model design as it was done for the uniaxial compression, as the basis on which the models shown in Equation 4.7 to 4.11 were based could still suit the diametrical results. In Table 4.6 it is possible to see the fitting results for each model tested.

Table 4.6: *Fitted parameters and statistical indicators for all the datasets of diametrical tests.*

	a	b	c	d	e	f	R-square	SSE	Structure
Model 1	10.01	0.715	10.50	0.099	0.480	-2.050	0.802	1.27e+5	1
Model 2	7.350	418.1	**0.58**	0.024	0.562	-2.803	0.553	2.88e+5	1
Model 3	5.312	0.715	10.5	0.076	0.471	**-4.3**	0.850	9.66e+4	2
Model 4	6.895	328	**0.58**	0.014	0.577	**-4.3**	0.555	2.86e+5	2
Model 5	27.62	359.4	**0.58**	1.83e-5	**1**	**-4.3**	0.673	1.11e+5	2

It can be clearly seen how the quality of the fitting is by far lower than the one achieved for the uniaxial testing. All the R-square are indeed below 0.90, which is considered the lower value to even accept a possible model: by comparison, the model chosen to represent uniaxial compression had a R-square close to 0.99. Other more complex structures have been tested incorporating different relationships between Ca_d and C_s, but no better fitting than Model 3 was found out. For this reason, it was not possible to suggest any empirical equation able to properly capture the behaviour of wet granular materials undergoing diametrical compression.

This said, the results obtained during the experimental investigation are still valuable: a common trend between the different materials analysed has been highlighted, and a whole set of dependencies between sample strength and material and testing conditions has been evaluated. Furthermore, it has been proven once more how the effect of the consolidation stress applied during the sample preparation cannot be neglected, and that different levels of consolidation can affect the dynamic strength as much as different operating conditions. The two indeed interact in a rather complex way and should not be considered singularly, as was previously done by all the works on the dynamic strength of wet granular materials [8, 18, 19]. The focus can now be switched to the fracture energy and the breakage modes of the samples, to look for possible correlations between the behaviours observed.

4.2.2 Analysis of the breakage mode

To further classify the breakage mode of the samples, it was decided to maintain the definition used in previous works [8] and define a semi-brittle behaviour as the mode at which failure occurs before 5% of deformation of the sample is reached. From Appendix 6 it can be clearly seen how the sample failure always happened before 0.65 mm of deformation had been reached, which is the value corresponding to 5% of strain for a cylinder prepared with a 13 mm die. The failure mode was therefore classified as semi-brittle for all the samples tested.

The values of fracture energy calculated in §3.4.5 were collected in a single plot, to highlight any trend in their distribution. Figure 4.7 collects the results:

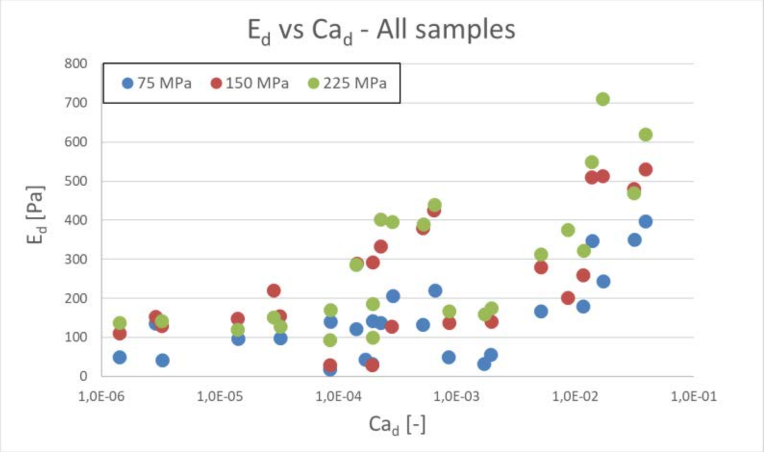

Figure 4.7: *Fracture energy versus diametrical capillary number for all the samples tested. Parametrised on the consolidation stress.*

It can be seen how two different peaks can be individuated in the graph, with one smaller one corresponding to a capillary number equal to 10^{-3}. As no physically fond model could be designed to describe a similar trend, it was decided to separate the experimental points following different criteria looking for the characteristic that causes the peaks in Figure 4.7. In Figure $3.47.a$ and $3.47.b$ it was already observed how the two peaks still appeared when representing the points divided by solid typology, denying how the unusual trend could be due to the particle size of the solid material. It was therefore decided to check whereas the peak could be due to the two different binder choices. As was previously mentioned in §3.4.5, the peak in fracture energy could be due to the slightly different shapes in the stress-strain profiles of the wet granular materials at different velocities. Considering two samples with the same capillary number, one with a low viscosity binder and tested at high speed, and the other with a high viscosity binder at tested at low speed, the fracture energy could be different because of different shapes of the stress-strain correlation. To verify this hypothesis, it was decided to represent separately the experimental $E_d - Ca_d$ points of the samples containing the two silicone oil: the graphs can be seen in Figure $4.8.a$ and $4.8.b$.

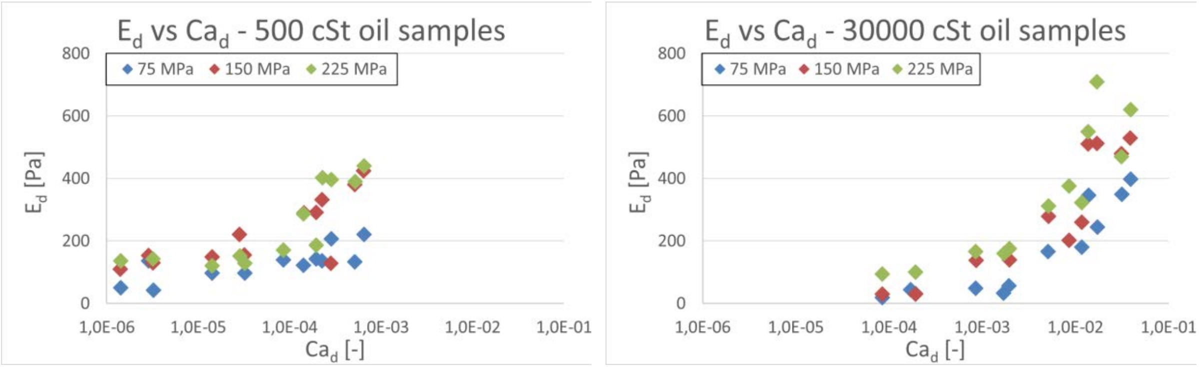

Figure 4.8.a, 4.8.b: *Fracture energy vs diametrical capillary number parametrised on the consolidation stress. For samples with 500 (a) and 30000 cSt oils (b).*

It two plots perfectly split the behaviour observed in Figure 4.7 and confirm the previous hypothesis: in the interval of capillary numbers between 10^{-4} and 10^{-3} indeed the two sets overlap, showing two largely different behaviours. Therefore, it can be deduced how the values of fracture energy do not depend just on the capillary number and on the consolidation stress, but also on the binder viscosity. Its value indeed causes the whole curve of experimental points to be shifted to the right the higher the binder viscosity is, giving local peaks of E_d as the ones observed in Figure 4.7. It could be assumed that for each set of consolidation stress and binder viscosity a whole different correlation between Str_d^* and Ca_d could be evaluated, with different shifting effects depending on the values of σ_1 and μ. An increase in consolidation stress would indeed cause the values of fracture energy to be shifted upwards, as it can be seen in Figure $4.7, 4.8.a$ and $4.8.b$ for the three sets of consolidations used for the tests. At the same time, using a more viscous binder would shift the curve to the right maintaining a rather similar shape.

This observation is particularly interesting as it allows to understand how the shape of the stress-strain relationship has a more complex dependency from the binder viscosity than the one previously observed by Smith [8]. The fracture energy indeed seems to have a fixed correlation with the capillary number, but different values of binder viscosity cause it to be shifted along the x axis. Furthermore, as only two typologies of powders could be tested during the experimental investigation, it was not possible to fit a model on such few materials. It was then decided to check how the transition to the dimensionless toughness T_d would impact the graphical representation of the results. In particular the focus was on the possibility that the normalisation of the fracture energy could provide a more general correlation between the toughness and the other parameters, Ca_d and consolidation stress. Figure $4.9.a$ and $4.9.b$ report the plots of dimensionless toughness versus diametrical capillary number for the materials prepared with the 500 cSt and the 30000 cSt silicone oils, respectively:

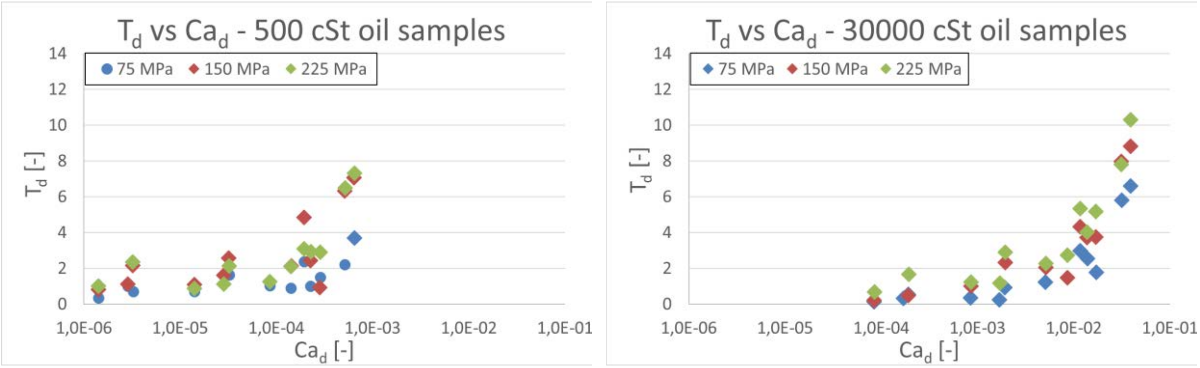

Figure 4.9.a, 4.9.b: *Dimensionless toughness vs diametrical capillary number, parametrised on the consolidation stress. Samples with 500 (a) and 30000 cSt (b) oils.*

The behaviour registered is the same as the one observed for the fracture energy, with the two materials showing different trends at the same value of capillary number. Furthermore, the effect of different consolidation stresses gets even less evident when moving to dimensionless terms, with the experimental points getting even more randomly distributed. The more interesting result is the confirmation that the dimensionless toughness maintains an almost constant value until a certain value of capillary number is reached, equal to $\sim 10^{-4}$ for the samples made with the low viscosity binder and to $\sim 10^{-2}$ for the high viscosity ones. Comparing this information to Figure 4.6, it can be seen how the dimensionless peak stresses are still almost constant at $Ca_d = 10^{-4}$ while T_d of the low viscosity samples shows a peak. Therefore, as the toughness is directly related to the shape of the stress-strain curve, it can be deduced that at higher deformation velocities the area below the curve increases (as described by Equation 3.13 and 3.14) while its peak is constant (as the values of Str_d^* remain constant). This introduces further complexity in the prediction of the values of dimensionless toughness and fracture energy, which should both be considered more as comparison parameters between different breakage modes than actual predictable information. Nonetheless, specific trends have been observed and could justify a further experimental investigation aiming at correlating the two models of breakage characterisation, the one based on the peak stress and the one based on the area below the stress-strain curve.

4.3 Final modelling considerations

The modelling phase of the experimental data was rather complex and required a lot of time to be properly set up both theoretically and computationally. The previous works on the topic have been widely analysed and taken into account for the choice of the models and of the parameters, always leaving room for more independent choices regarding the equations' structures and the parameters values. While the modelling of the uniaxial compression tests proceeded smoothly and provided an efficient and properly validated model, no satisfying correlation could be found for the diametrical compression experimental data. Switching the point of view of the analysis to the fracture energy did not help either, but allowed to capture the more complex correlations between material and testing parameters with improved quality. The following objectives have been achieved:

- ✓ Different models for the uniaxial testing were designed using the observations of Chapter 3, validating their fitting capability with the experimental data. A final 6-parameters model has been proposed, with a R-square close to 0.99.
- ✓ The designed model has been used to try to predict the flow function of a wet granular sample, obtaining optimal agreement between the theoretical results and the empirical values. The interactions between viscous forces and consolidation stresses have been further investigated.
- ✓ Different models for the diametrical testing were designed, but no satisfying fitting could be achieved. The breakage modes of the samples have been characterised in correlation with the failure energy and the dimensionless toughness, but no empirical model could be found, too.

Chapter 5

DEM Simulation

One of the main objectives of the whole experimental investigation was to provide a wide and consistent set of experimental data on the strength of wet granular material, on which a suitable DEM simulation of the uniaxial testing could be based. Given the complexity of recreating the different steps of the tests, the quality of the experimental data was fundamental to properly choose and then tune the simulation to fully represent the experimental procedure. In this chapter the set-up of the simulation will be described, with particular focus on the final sequence and on the predicted results.

5.1 Theoretical background

The term DEM, or *Discrete Element Method*, defines a group of numerical methods aimed at evaluating the behaviour of large groups of small particles. The method computes the motion and interactions of group of particles basing the calculations on the molecular dynamics, allowing the description of rotational degrees of freedom too. The modern improvements in the computational power and the continuously improving algorithms have allowed to increase the number of particles simulated on single processors, upon reaching millions and millions of single units with even more complex shapes. The method furthermore allows to take into account more effects not strictly related to the solid particles, such as capillary bridges, once a suitable model has been proposed. This characteristic is particularly interesting for the application of this study, as the presence of liquid binders has a primary role in the determination of the strength of the wet granular samples. It should also be noticed that if more discontinuous materials have to be described (such as granular flows, highly wetted granular materials, particles flowing in liquids) the method can be coupled with CFD to form an EDEM, *Extended Discrete Element Method*, taking into account thermodynamics and fluid mechanics.

The main drawback of DEM simulations is the high computational requirement, which increases even more for each element of complexity added to the system. Furthermore, to have acceptable simulation times it is often required to scale down the systems, reducing the overall number of particles while still maintaining the geometrical and physical characteristics of the system. This alternative had to be chosen for all the simulations carried out during the project: it can be easily calculated that, even considering the MCC Cp-305 particles and an average level of packing, over than 10^6 single particles are present inside the testing cylinder of the AUPT machine. Considering the increased computational effort of introducing the liquid binder, the computational effort would have been incompatible with the short amount of time available for the project. Furthermore, having to first design the simulation procedure and then perform the computation for more sets of samples, it was mandatory to choose a scaling able to be simulated in less than 48 hours. See §5.2 for more information on the design.

The code used for the simulation has been developed by the research group lead by Professor Charley Wu, working at the University of Surrey, Guildford (UK). The code incorporates various models for the description of the interparticle forces, based on previous literature works and chosen to obtain an optimal representation of the behaviour of wet granular materials. In particular, for the description of the capillary force the model of Lian and Seville [49] was implemented, which has the following equation:

$$F_{cap} = \frac{(2\pi - 2.082\varphi_0^{0.9197})[cos\theta - 0.16\varphi_0(1 + \varphi_0)tan\theta]}{1 + 0.8438\varphi_0^{-0.724}S_\theta + 1.3393\varphi_0^{-1.459}S_\theta^2} \tag{5.1}$$

where θ is the contact angle, φ_0 and S_θ are the half filling angle and the rupture distance respectively, defined as functions of the volume of liquid in the liquid bridge. Their correlation is given by:

$$V = (1 + 1.653\varphi_0 sin\theta)0.654\varphi_0^{3.73} \tag{5.2}$$

$$S_\theta = \frac{S[1 + 0.5\theta cos^2(\varphi_0 + \theta)]}{(1 + 0.5\theta)(V^{1/3} + 0.1V^{2/3})} \tag{5.3}$$

where S is the dimensionless separation distance. Solving Equation 5.2 and 5.3 it is possible to obtain both parameters. The work of Thornton *et al.* has been used for the computation of the contact force model [50, 51].

5.2 Simulation design

The setup of the simulation was the most crucial part of the whole computational analysis. The simulation indeed had to be properly designed to avoid any kind of numerical instability, while at the same time maintaining the physical characteristics of the system. The main issues were related to the calculation cycling, which had to be finely tuned for each section to obtain the exactly required parameters. Other complications were connected with the compression of the particles during the consolidation and wall removal phases, which often caused some particles to bounce away if the relaxation was not sufficient. All these problems had to be solved by trial and error, with different solutions providing different results.

5.2.1 Particle generation and consolidation

The initial phases of the simulation required to generate, deposit and consolidate the particles inside the testing cylinder, as is achieved during the AUPT testing. It also had to be properly designed to avoid that any imperfection propagates to the successive phases, while the initial choices on the system size and on the number of particles determine the time scale of the whole simulation. To maintain a simulation time below 48 hours it was initially decided to work with a $20:1$ ratio, creating a cylinder that was 20 times smaller than the real one. Therefore, it was found out that to obtain a sample geometry similar to the experimental one it was needed to generate, deposit and consolidate around 1200 particles: this is suitable with the simulation times chosen while still granting a bulk of particles large enough to avoid interferences by local irregularities.

Given the large times required for designing, tuning and then performing a sufficient amount of simulations, not all the wet granular samples could be tested. The models implemented in the code were not designed to describe capillary bridges for high viscosity binders, such as the 30000 cSt silicone oil, and therefore it was not possible to simulate any of the samples made with it. Modifying the code implementing different models was not possible, both because of the lack of time and of the complexity of the procedure. It was thus decided to stick to the 500 cSt oil and choose suitable combinations of binder-powder. It was indeed decided to simulate only the MCC Cp-102 particles, mainly to have more time to obtain satisfying results and set up a perfectly tuned and consistent simulation. Furthermore, using the $20:1$ scaling both MCC Cp-203 and Cp-305 would be too sensible to local irregularities, given the lower number of particles that could be fitted in the cylinder. Having to setup different scaling for each different material would have required too much time compared to the length of the study. With these limiting choices it was possible to begin the simulation setup phase, which was divided into 5 different sections, each of which had its own list of commands. At the end of the simulation analysis it was decided to quickly perform an extra series of simulations using a $10:1$ scaling, still for MCC Cp-102 and 500 cSt silicone oil. This setup was based on the final simulation design of the $20:1$ scaling, properly tuning the structure size and particle number to fit the new scaling. In particular the particle number was increased by 8 times to fit the new cylinder size, and therefore the simulation time increased, too. For sake of simplicity, the simulation steps and results of the two scaling are reported together.

In the first phase, *generation*, the parameters and indexes of the powder were introduced: particle size, elastic module, density and friction coefficient had already been measured or taken from the technical sheet of the material, and grouped up under the definition of *material 1*. The wall material was defined as *material 2* and its properties were set to be similar to a glassy polymer, with a high elastic module that grants the rigidity of the walls. Then, the cylindrical support was designed creating a floor plane and 20 vertical planes forming the cylinder walls, as the code was set to work only with flat surfaces. The walls were designed to be by far taller than the real ones, to make it easier to generate the particles inside. The 1200 (10000 in the 10: 1 scaling) single units were then generated inside the cylinder with 3 different particle sizes respecting the PSD measured in §3.1, and the gravity acceleration was introduced as the only force acting on the particles. The time fraction was set in this section, too, as the fraction of the critical time-step to be used in the computational cycles: a value of 0.5 was chosen to better deal with numerical instability. In Figure 5.1 is is possible to see the state of the system at the end of the generation phase, for the 20: 1 and the 10: 1 scaling. The whole list of commands can be found in Appendix 7.

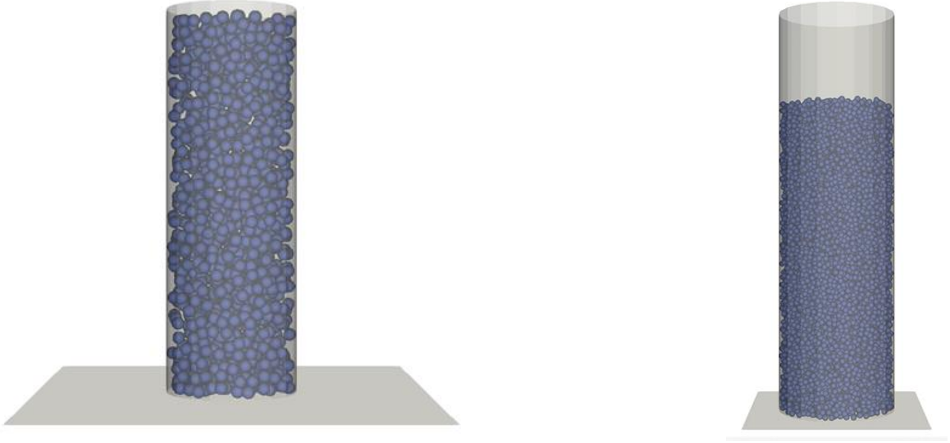

Figure 5.1.a, 5.1.b: *Simulation state at the end of the generation phase, for a 20:1 sample (a) and s 10:1 (b) sample scaling.*

In the second phase, *deposition*, a set of calculation cycles were run to give enough time for the gravity force to act on the particles, allowing their deposition on the bottom of the structure and their compaction due to gravity. This section corresponds to the pouring of the material inside the cylindrical sleeve of the AUPT machine, and was achieved with 16 sets of 10^5 iterations each. This value was determined by setting a high number of iterations and checking the height of the powder bulk, until its value became almost constant. Initially an extra simulation phase was added after the deposition, named *Trimming*, in which a horizontal plane was inserted at the top of the powder bulk and slid alongside it. The objective was to make the powder surface more regular, but it had the effect of adding elastic potential energy to the top layers of particles, which tended to move as soon as the plane was removed. The phase was thus substituted with an increased cycling during the deposition.

In Figure $5.2.a$ and $5.2.b$ the state of the systems at the end of the deposition phase can be seen:

Figure 5.2.a, 5.2.b: *Simulation state at the end of the deposition phase, for a 20:1 sample (a) and s 10:1 (b) sample scaling.*

The next phase was the *consolidation*, in which the samples were compressed until the desired consolidation stresses were reached. This phase has been one of the most complex to fully achieve correctly, both due to the difficulties at evaluating the top surface stress and to the long times required to tune the cycling phase. Initially the liquid binder was "added" to the powder system, meaning that the model equation, Equation 5.1, was introduced in the system to solve, while the liquid properties were introduced to determine the various liquid bridge parameters. After this, a single flat plane was disposed horizontally above the powder bulk, as close as possible to the particles to save some computational time. It was then moved downwards at a fixed, slow speed, consolidating the particles more and more. As it was not possible to insert a feedback control cycle that stopped the consolidation when the desired σ_1 was reached, the simulation had to be run slowly and with small cycles sets. Initially it was decided to work with a 20000 iterations set, after which the particle distribution and the top stress were checked while the total number of iterations was registered. Once the value got closer to the desired one the number of iterations per set was reduced, finely tuning the total number until a value was obtained inside a $\pm 5\%$ range of the desired σ_1. This procedure was lengthy and had to be repeated each time any modification on the previous phases occurred, and checked every time a different level of consolidation had to be reached. In Figure $5.3.a$ and $5.3.b$ it is possible to see the final state of the samples after the consolidation phase.

Figure 5.3.a, 5.3.b: *Simulation state at the end of the consolidation phase, for a 20:1 sample (a) and s 10:1 (b) sample scaling.*

After this phase the samples are in the same condition of the AUPT ones, when the piston stops at the end of the consolidation for the sleeve removal. The particles have rearranged and compacted, but have also accumulated elastic potential energy that could be released as soon as the walls are removed. For this reason, an extra relaxation phase will have to be added to avoid any relevant particle motion during the final failure testing. It should also be noticed how the samples have a height to diameter ratio slightly larger than 1, which agrees with the experimental data obtained during the uniaxial compression testing.

Furthermore, while in the AUPT testing the consolidation was achieved in two separate compression phases, in the simulation it was decided to achieve it with a single compression. The design of the relaxation phase between the two could have added further complexity in an already difficult tuning

5.2.2 Relaxation and failure compression

The design of the *relaxation* phase was particularly complex and provided different computational solutions, none of which was completely satisfying. In the experimental procedure the cylinder sleeve is removed while the piston is still compressing the sample: this done, the piston moves upwards until the stresses on the wet granular material are removed and then proceeds with the failure compression. It was therefore tried to recreate the same mechanism in the simulation, too, preparing different setups until a suitable design was found.

In the first setup it was tried to exactly replicate this procedure: the external plans forming the cylinder were moved upwards, maintaining the upper plane in its position. Nonetheless, many of the external particles got stuck on the walls or were simply dragged away, causing wide damages to the external layers and neglecting the quality of the sample. In the successive design all the walls external were deleted rather than moved upwards, still maintaining the top wall in position. But, due to the elastic potential energy accumulated during the consolidation, many particles tended to jump off from the cylinder and scatter in the external space, making the sample not reliable for the simulation. Other designs involved: the contemporary removal of the external and top walls; the removal of the top wall first, a relaxation phase and the removal of the external walls later; the removal of the external walls while the top wall slides upwards. None of the designs was properly suitable for the application, mainly because of the displacement of the particles as soon as one of the walls was removed.

In the final design, which was the one granting the lower loss of particles, the initial relaxation was performed with all the walls still in position, for a total of 10^5 cycles. Immediately after the relaxation the external walls were removed and the sample was ready for the failure phase. It was decided not to replicate the upwards-downwards movement of the upper wall (as happens in the AUPT testing) as the particles tended to stick to the wall giving an unrealistic behaviour. In Figure $5.4.a$ and $5.4.b$ it is possible to see the two samples immediately after this phase:

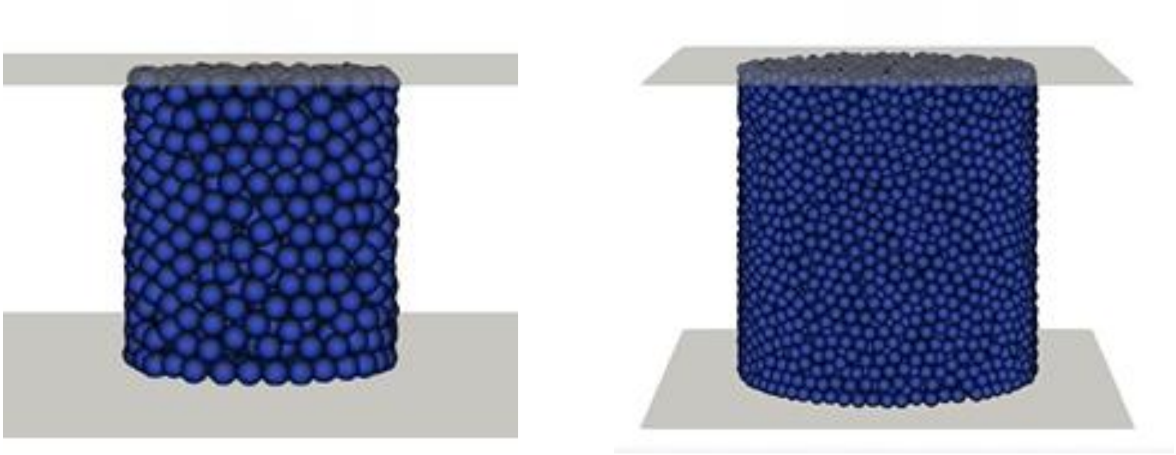

Figure 5.4.a, 5.4.b: *Simulation state at the end of the relaxation phase, for a 20:1 sample (a) and s 10:1 (b) sample scaling.*

The successive step was the failure deformation, that had to be achieved by compressing the sample at a given, fixed speed. It should be noticed that the velocities used in the simulation were maintained equal to those chosen for the AUPT tests: the downscaling was used to describe just a cylindrical section of the whole real sample, and therefore the velocity should no be changed. Furthermore, as the analysis will shift to the dimensionless numbers Str^* and Ca, the relevancy of the choice was limited.

The *compression* phase was rather simple if compared with the previous ones: the top wall, kept from the consolidation phase, was moved downwards at the desired velocity. At the end of each set of cycles a sheet was updated with various system properties, such as the top wall displacement and the top wall force. The length of the deformation depended on the number of cycles computed, but generally only the $5-10\%$ of strain was of any interest for the comparison with the experimental data as the peak stress could be generally found in that interval. Furthermore, as the $10:1$ sample had around eight times more particles than the other one and thus required by far longer simulation times, it was tried to limit the deformation to small strain levels. In Figure $5.5.a$ to $5.5.c$ it is possible to see three states of deformation for the $20:1$ sample scaling, while in Figure $5.5.d$ to $5.5.f$ three states can be seen for the $10:1$ sample.

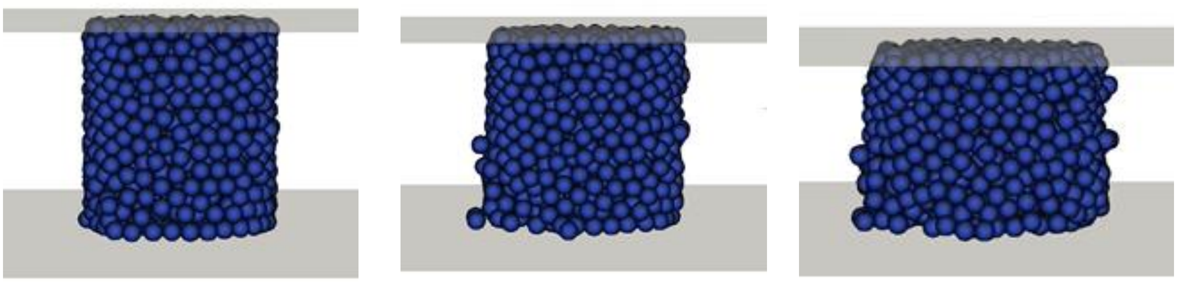

Figure 5.5.a, 5.5.b, 5.5.c: *Simulation state at different strain rates, for the 20:1 sample.*

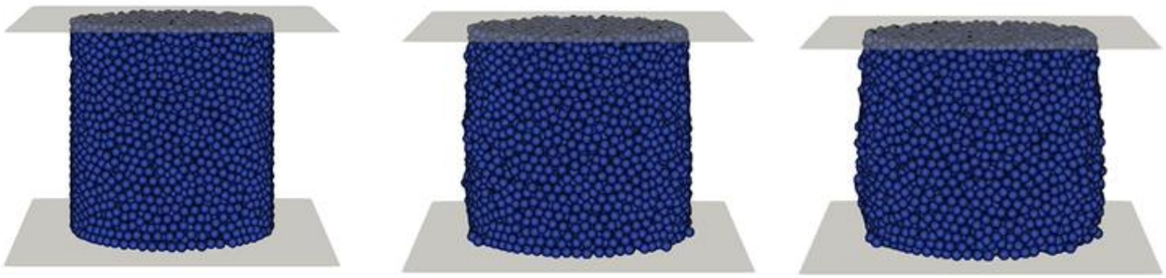

Figure 5.5.d, 5.5.e, 5.5.f: *Simulation state at different strain rates, for the 10:1 sample.*

5.3 Simulation results

As previously mentioned, each iteration of the compression phase produced a new set of values in the data sheet of the simulation. This sheet included the normal and tangential forces on the top wall in all directions, as well as the simulation time and the top wall displacement. The datasets were particularly lengthy, thus it was decided not to report them in the appendix. Each set of data was elaborated through the MATLAB® software, first to obtain the stress-strain profiles of the samples, and then the $Str^* - Ca$ correlation. It was immediately clear that it would have not been possible to simulate all the experimental conditions analysed with the AUPT testing, as a single simulation could easily take more than 24 hours. Furthermore, the set of velocities of interest could not be entirely represented, as any value below 10^{-1} would have taken too much time: more than 15 days were indeed estimated to be required for the simulation of a sample compressed at 0.01 mm/s, making it unfeasible with the length of the study. It was also decided to work with two different consolidation stresses, 20 and 100 kPa, to obtain a reliable set of data before proceeding with a more in-depth study. This led to the design and testing of 12 different samples configuration, whose characteristics are reported in Table 5.1:

Table 5.1: *Testing parameters and configurations for the simulated samples.*

	Parameter choice
Deformation speed	0.5, 2, 5 mm/s
Consolidation stress	20, 100 kPa
Sample scaling	20:1, 10:1

The stress-strain profiles were then represented graphically for each sample, to verify the behaviour and evaluate the peak stress. In Figure 5.6.a to 5.6.d it is possible to see the experimental representation.

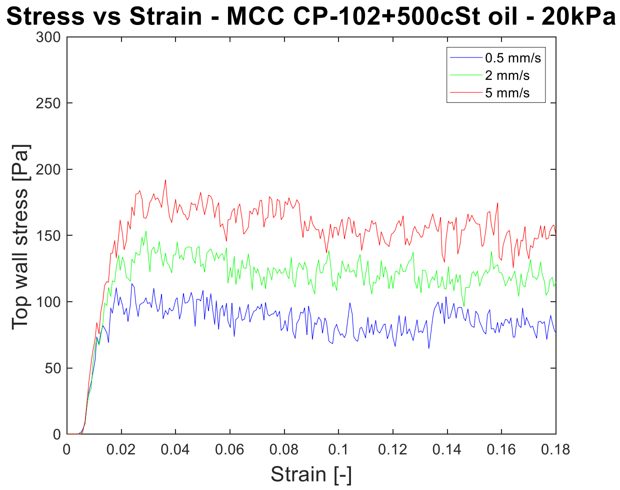

Figure 5.6.a: *Stress-strain correlation for MCC Cp-102 plus 500 cSt silicone oil samples, with a 20:1 scaling. Consolidated at 20 kPa, compressed at 0.5, 2 and 5 mm/s.*

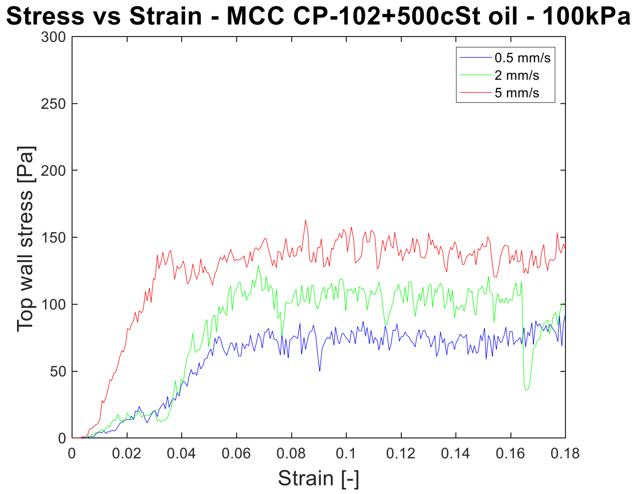

Figure 5.6.b: *Stress-strain correlation for MCC Cp-102 plus 500 cSt silicone oil samples, with a 20:1 scaling. Consolidated at 100 kPa, compressed at 0.5, 2 and 5 mm/s.*

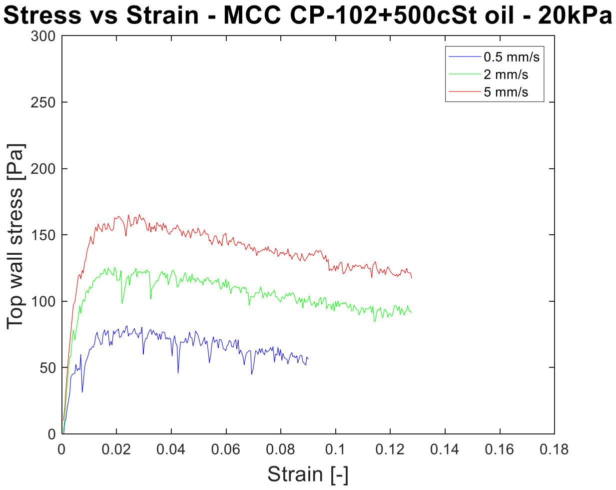

Figure 5.6.c: *Stress-strain correlation for MCC Cp-102 plus 500 cSt silicone oil samples, with a 10:1 scaling. Consolidated at 20 kPa, compressed at 0.5, 2 and 5 mm/s.*

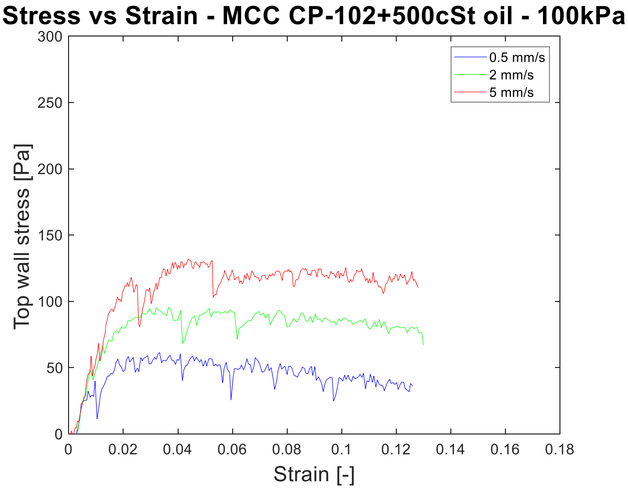

Figure 5.6.d: *Stress-strain correlation for MCC Cp-102 plus 500 cSt silicone oil samples, with a 10:1 scaling. Consolidated at 100 kPa, compressed at 0.5, 2 and 5 mm/s.*

The stress-strain graphs have a rather interesting distribution. The shape of the plots is similar to the ones observed experimentally by most previous works [8, 18, 19], but could not be compared with the experimental results obtained with the AUPT machine as it does not provide the stress-strain datasets. The values of stress increase rapidly at the beginning, reaching a soft peak and then slowly decrease as the levels of strain increase. From the macroscopic point of view, therefore, it can be assumed that the simulation is able to capture the behaviour of the wet granular materials with good accuracy. Furthermore, in all the four figures it can be seen how the resistance to deformation of the samples increases as the deformation velocity increases, which is a phenomenon widely observed experimentally in §3.3 and §4.1. But, if from a general point of view the simulation seemed to be working properly more issues were noticed when the attention was switched to the numerical results.

It is indeed possible to see how the difference between the $20:1$ and the $10:1$ scaling is significant, with the smaller samples providing stress values about 20% larger than the other ones for all the testing conditions. Furthermore, and more importantly, the samples compressed at 100 kPa presented stress values that were by far lower than the ones obtained at 20 kPa. This issue highlights the limits of the simulation, as during the experiments it was observed how an increase in the consolidation stress makes the sample more resistant to deformation. It is not clear why the samples show this behaviour, but a hypothesis could be that the extra consolidation applied to the 100 kPa samples does not result in just a particle rearrangement, but also in an accumulation of potential elastic energy. As a result, when the walls are removed and the compression begins the particles have already started failing, giving a weakened structure. Moreover, this hypothesis could explain why the 100 kPa samples have an initial stress-strain curve that increases slower than the 20 kPa ones, reaching the peak value at a higher strain. It was tried to solve the problem by modifying the relaxation time before the compression, both increasing or decreasing its value, but no relevant improvement could be achieved. It was therefore decided to switch the analysis to the dimensionless numbers Str^* and Ca, looking for a more general description.

In Table 5.2 it is possible to see a summary of the testing parameters and results of each sample. The corresponding capillary number and dimensionless peak stress were calculated for each sample, too. To better compare the data with the experimental results, the values of Str^* were calculated with the model developed in §4.1, expressed in Equation 4.12.

Table 5.2: *Summary of the testing parameters of each simulation performed.*

Scaling	Consolidation Stress [kPa]	Def. speed [mm/s]	Peak stress [Pa]	Capillary number	Str* Simulation	Str* Model
20:1	20	0.5	115	0.0005	0.82	5.65
20:1	20	2	155	0.0021	1.11	6.26
20:1	20	5	185	0.0054	1.32	7.04
20:1	100	0.5	80	0.0005	0.57	8.07
20:1	100	2	135	0.0022	0.97	8.69
20:1	100	5	145	0.0054	1.04	9.47
10:1	20	0.5	85	0.0003	0.61	5.53
10:1	20	2	125	0.0014	0.89	6.00
10:1	20	5	160	0.0034	1.14	6.60
10:1	100	0.5	60	0.0003	0.43	7.96
10:1	100	2	95	0.0014	0.68	8.43
10:1	100	5	140	0.0034	1.00	9.02

Looking at the last two columns it can be clearly seen how the values of the simulated samples are lower than the predicted ones, which are based on the model evaluated from the experimental data. This said, their respective behaviour has the same trend as the one of the experimental data, with a smooth increase in their value with the increase of the capillary number. Indeed, when $Ca \cong 10^{-3}$ it had been observed experimentally how the values of dimensionless peak stress start increasing, and the simulation is able to capture this behaviour. Furthermore, the values of Str^* obtained from the simulation are of the same order of magnitude as the experimental ones, which indicates how the simulation design has a strong theoretical basis. A more suitable tuning of the deposition and relaxation phases should be performed to improve the quality of the results.

The DEM simulation has proved to be a strong and effective tool for the representation of wet granular materials. The simulation design required a long trial and error procedure, but the final set-up has given encouraging results. The main problems observed were related to the effect of the magnitude of the consolidation stresses, which are larger than the commonly used ones, and their effects on the particles packing. Observing the particles behaviour indeed it can be seen how the rearrangement effects are not as evident as it was during the experimental testing, and it could be assumed that most of the energy impressed gets accumulated as elastic potential energy. For this reason, a further tuning should be focused on these phases to grant a suitable relaxation time, while the overall structure of the simulation is solid enough to be used for further analysis. It should also be considered the possibility of carrying out simulations with more particles, to limit even more the effects of local irregularities.

Conclusions

The main objectives defined at the beginning of the study were:

- ✓ To design and validate a new sample preparation and testing procedure;
- ✓ To uniaxially and diametrically test wet granular materials, developing two suitable models for the description of their behaviour;
- ✓ To develop a DEM simulation for the uniaxial testing.

The initial powder characterisation was achieved by performing a wide set of experimental analysis through the QicPic machine, the optical microscope and the scanning electron microscope. The particle size and shape of each material was evaluated through the calculation of the average diameter, of the aspect ratio and of the circularity of the particles. Their values were then used for the modelling phase, and allowed to better understand the behaviour of the wet granular materials. It was indeed noticed how the particles with the more irregular shapes gave a wet granular sample more resistant to deformation than the regular ones, due to the effects of particle interlocking. This effect was introduced in the final model for the uniaxial testing as a power law of the aspect ratio, and proved to be highly accurate for the materials considered. The images captured with the optical microscope and the SEM confirmed the results of the QicPic analysis, and provided interesting information on the complex shape of both MCC Celphere™ and PMMA Elvacite® 3001. These information came in handy for the evaluation of the contact angle between the powders and the liquid binder, as they allowed to understand the irregular behaviour of PMMA particles.

As regards the sample preparation phase, a new mixing methodology was then designed and validated. A Turbula® mixer was chosen, and a specific set of mixing speed and preparation time were fixed. The mixing quality was then assessed both by eye and through an uniaxial testing, to further verify the homogeneity of the procedure.

Once the material properties had been determined and the preparation methodology had been validated, the uniaxial compression tests could be performed. Over 200 different samples were tested, with different combinations of powders and binders. The deformation speed and the consolidation stresses were changed, too, and the effect of each parameter on the uniaxial unconfined yield stress was captured graphically. It was found that an increase in consolidation stress and/or deformation velocity and/or binder viscosity cause an increase in the value of uUYS, while an increase in particle size provides a decrease in its values. The whole behaviour was expressed in dimensionless terms using the definitions of dimensionless peak stress (Str^*) and capillary number (Ca). A new dimensionless number, the dimensionless consolidation stress (C_s), was defined and implemented in the design of a possible empirical model. Five different models were designed starting from the experimental observations, and supported from the theoretical results of previous works. Each model was fitted on the experimental datasets and its quality was determined on the base of the values of R-square. The model also allowed to predict the shape of the flow function of the wet granular materials once the value of Ca was fixed, and it highlighted how different testing conditions could cause it to assume different shapes. The interaction between sample strength and sample flowability was fully discussed and justified, while the model proved to be extremely efficient at predicting the flow functions of the 8 different powder-binder combinations.

A similar behaviour was observed for the diametrical testing, and the correlations between the peak stress and the material and testing parameters were represented graphically. Nonetheless, the limitations of the equipment did not allow to capture a range of capillary numbers as wide as for the uniaxial testing, while the larger instrumental errors caused more uncertainty on the results of the peak stresses. The analysis was still switched to the dimensionless numbers used for the uniaxial compression, and similar models were fitted on the experimental datasets. This time no satisfying fitting was achieved for any of the models, and two new parameters, the fracture energy E_d and the dimensionless toughness T_d, were evaluated while looking for any correlation. The most interesting result was related to the shape of the stress-strain curve of the sample, which was found out to be dependent on the strain rate used for the test.

The DEM simulation was then designed and carried out for two different scaling of the sample, focusing on the MCC Cp-102+500 cSt silicone oil combination. The final simulation was divided into 5 phases and was performed for a $10:1$ and a $20:1$ scale, with the setup of the consolidation and relaxation phases being particularly complex and requiring a long tuning phase for the relaxation times of the particles. The final results had the same order of magnitude as the experimental ones but were still far from the actual value, indicating how the simulation structure is effective but still needs substantial improvements.

On the basis of these results, the following future works are suggested:

- To extend the analysis considering different powders and binders, focusing on highly irregular particles and high viscosity binders.
- To perform uniaxial and diametrical tests with equipment able to work at higher deformation speeds, thus broadening the range of capillary numbers used.
- To improve the design of the simulation until the results agree with the experimental values, and then extend the analysis to more powders/binders combinations.

List of figures

List of tables

Symbols

$\dot{A}_{drop}$	Rate of generation of drop projected area	[m^2/s]
$\dot{A}_p$	Rate of passage of solid surface	[m^2/s]
A_p	Particle projected area	[m^2]
Ca	Capillary number	[-]
Ca_d	Diametrical capillary number	[-]
c_h	Cohesivity	[Pa]
C_s	Dimensionless consolidation stress	[-]
d_{die}	Die diameter	[m]
d_p	Particle diameter	[m]
d_{min}	Smallest diameter of the particle projected area	[m]
d_{max}	Largest diameter of the particle projected area	[m]
d_{50}	Median diameter of the distribution	[m]
d_{90}	Diameter above which 10% of the particle in the distribution can be found	[m]
d_{10}	Diameter below which 10% of the particle in the distribution can be found	[m]
ΔP_{cap}	Capillary suction pressure	[Pa]
E_d	Fracture energy	[Pa]
F_{cap}	Capillary force	[N]
F_d	Peak failure load in diametrical compression tests	[N]
ff	Flow factor	[-]
g	Gravity acceleration	[m/s^2]
H	Sample height	[m]
m_{punch}	Mass of the top punch of the die	[kg]
P_p	Particle perimeter	[m]
r_i	Curvature of the bridge surface	[m]
S	Liquid pore saturation	[-]
S_θ	Rupture distance	[m]
St_{def},	Stokes deformation number	[-]
Str^*	Dimensionless peak stress	[-]

Str_d^*	Diametrical dimensionless peak stress	[-]
T_d	Dimensionless toughness	[-]
U	Average relative granule collision velocity	[m/s]
W_d	Pellet width	[m]
Y	Granule dynamic yield strength	[N]
y	Capillary bridge profile	[-]

Greek letters

Ψ_a	Spray flux number	[-]
γ	Liquid surface tension	[N/m]
$\dot{\varepsilon}$	Strain rate	[s^{-1}]
ε_{gr}	Granule porosity	[-]
μ	Binder viscosity	[Pa*s]
μ_f	Coefficient of internal friction	[-]
ρ	Density	[kg/m^3]
σ_c	Peak failure stress	[Pa]
σ_d	Peak failure stress in diametrical compression tests	[Pa]
σ_n	Loading normal stress	[Pa]
σ_p	Granule tensile strength	[Pa]
σ_1	Consolidation stress	[Pa]
φ_c	Circularity	[-]
φ_D	Distribution span	[-]
φ_0	Half filling angle	[rad]
θ	Liquid-solid contact angle	[rad]
τ_f	Shear stress at failure	[Pa]
τ_p	Dimensionless drop penetration time	[-]
v_p	Relative velocity of the moving impact	[m/s]
v	Failure velocity	[m/s]

Acronyms

AR	Aspect ratio	
AUPT	Advanced uniaxial powder tester	
DEM	Discrete element method	
FF	Flow function	
H/D	Height to diameter ratio	
MCC	Micro-crystalline cellulose	
PMMA	Poly(methyl-methacrylate)	
PSD	Particle size distribution	
SEM	Scanning electron microscope	
uUYS	Uniaxial unconfined yield stress	[Pa]

Acknowledgments

Prof. Chuan-Yu Wu

For the support and the helpful suggestions during my stay at the University of Surrey.

Prof. Lian Liu

For the daily assistance and the priceless advices on the DEM simulations.

Prof. Andrea Claudio Santomaso

For the help and the assistance during the writing of this dissertation

All the PhDs, researchers and professors I worked with: Prof Hare, Prof. Taylor, Azza, Busayo, Ana, Silvia, Xin, David, Bill, Tom, Hao, Nicolin and many others

For baby-sitting me during the first weeks in the Lab, providing useful advices and sharing your knowledge on the granular materials. All of you helped making this project possible.

My housemates: Raluca and Veronica

For sharing our daily lives and helping me survive in the UK, making even the toughest moments a bit easier to withstand. You are both amazing.

Giovanni and Lorenzo

For sharing so many British moments, meals, evenings, weekends and adventures. Your advices and support during these months have been so valuable and important.

All the people I met in Guildford: Matilde, Susana, Cecilia, Ruxanda, Jules, Kieran, Tim, Ash, Max and many others

For making this experience even more unique and memorable, for spending so much time together at the university, in the gym, in Guildford and in other adventures.

Gaia, Riccardo, Rossana, Serena

For all the time we spent together during these years, the projects, the team works, the determination in keeping me awake at 8 a.m. and many, many other reasons. You're the best friends and classmates I could ask for, and helped me so much achieving this goal.

All my friends and relatives that are sharing this moment

For helping and supporting me throughout all these years, in so many different ways. Each of you had a role in this achievement.

Mom, Dad and Gloria

For allowing me to choose this university course and being so patient and encouraging for so many years. For supporting me at any exam and celebrating regardless of its results. Thank you.

Monica

For you wholehearted support, for understanding and encouraging me throughout the most difficult moments, for pushing me to give my best and be the best version of myself every day. Thank you so much.

Appendix

Appendix 1: Particle Size Distribution

Cumulative distribution

MCC Cp-102		MCC Cp-203		MCC Cp-305		PMMA	
Size $[\mu m]$	%	Size $[\mu m]$	%	Size $[\mu m]$	%	Size $[\mu m]$	%
6.21	0	6.21	0	6.21	0	6.21	0
6.25	0	6.25	0	6.25	0	6.25	0
8.05	0	8.05	0	8.05	0	8.05	0
10.38	0	10.38	0	10.38	0	10.38	0
13.39	0	13.39	0	13.39	0	13.39	0
17.26	0	17.26	0	17.26	0	17.26	0
22.26	0	22.26	0	22.26	0	22.26	0
28.7	0	28.7	0	28.7	0	28.7	0
37	0	37	0	37	0	37	0
47.71	0.01	47.71	0	47.71	0	47.71	0.01
61.51	0.03	61.51	0	61.51	0	61.51	0.03
79.31	0.13	79.31	0	79.31	0	79.31	0.13
102.26	0.45	102.26	0	102.26	0	102.26	0.45
131.85	1.51	131.85	0	131.85	0	131.85	1.51
170	7.87	170	0.01	170	0	170	7.87
219.2	33.29	219.2	2.42	219.2	0	219.2	33.29
282.63	76.75	282.63	73.61	282.63	0	282.63	76.75
364.41	91.38	364.41	98.87	364.41	6.68	364.41	91.38
469.86	95.13	469.86	100	469.86	74.6	469.86	95.13
605.83	97.72	605.83	100	605.83	99.19	605.83	97.72
781.14	100	781.14	100	781.14	100	781.14	100
1007.17	100	1007.17	100	1007.17	100	1007.17	100

Distribution density

MCC Cp-102		MCC Cp-203		MCC Cp-305		PMMA	
Size $[\mu m]$	%	Size $[\mu m]$	%	Size $[\mu m]$	%	Size $[\mu m]$	%
4.39	0	4.39	0	4.39	0	4.39	0
6.23	0	6.23	0	6.23	0	6.23	0
7.09	0	7.09	0	7.09	0	7.09	0
9.14	0	9.14	0	9.14	0	9.14	0
11.79	0	11.79	0	11.79	0	11.79	0
15.2	0	15.2	0	15.2	0	15.2	0
19.6	0.001	19.6	0	19.6	0	19.6	0
25.27	0.002	25.27	0	25.27	0	25.27	0
32.58	0.003	32.58	0	32.58	0	32.58	0
42.01	0.006	42.01	0	42.01	0	42.01	0
54.17	0.007	54.17	0	54.17	0	54.17	0.002
69.85	0.005	69.85	0	69.85	0	69.85	0.01
90.06	0.002	90.06	0	90.06	0	90.06	0.029
116.12	0.11	116.12	0	116.12	0	116.12	0.096
149.72	2.678	149.72	0.001	149.72	0	149.72	0.576
193.04	5.297	193.04	0.218	193.04	0	193.04	2.302
248.9	0.934	248.9	6.45	248.9	0	248.9	3.937
320.93	0.015	320.93	2.289	320.93	0.605	320.93	1.326
413.79	0	413.79	0.102	413.79	6.153	413.79	0.34
533.53	0	533.53	0	533.53	2.228	533.53	0.235
687.92	0	687.92	0	687.92	0.074	687.92	0.206
886.98	0	886.98	0	886.98	0	886.98	0

Appendix 2: Aspect Ratio Distribution

MCC Cp-102		MCC Cp-203		MCC Cp-305		PMMA	
Size [μm]	%	Size [μm]	%	Size [μm]	%	Size [μm]	%
4.39	0.707	4.39	0.707	4.39	0.707	4.39	0.707
6.23	/	6.23	/	6.23	/	6.23	/
7.09	0.447	7.09	0.447	7.09	0.447	7.09	0.447
9.14	0.508	9.14	0.505	9.14	0.52	9.14	0.561
11.79	0.521	11.79	0.543	11.79	0.566	11.79	0.553
15.2	0.543	15.2	0.613	15.2	0.614	15.2	0.581
19.6	0.586	19.6	0.684	19.6	0.633	19.6	0.602
25.27	0.658	25.27	0.722	25.27	0.681	25.27	0.712
32.58	0.703	32.58	0.742	32.58	0.713	32.58	0.725
42.01	0.694	42.01	0.736	42.01	0.739	42.01	0.793
54.17	0.638	54.17	0.612	54.17	0.688	54.17	0.871
69.85	0.613	69.85	0.693	69.85	/	69.85	0.889
90.06	0.625	90.06	0.708	90.06	/	90.06	0.887
116.12	0.845	116.12	/	116.12	/	116.12	0.889
149.72	0.855	149.72	0.782	149.72	/	149.72	0.902
193.04	0.826	193.04	0.823	193.04	/	193.04	0.894
248.9	0.77	248.9	0.853	248.9	0.843	248.9	0.854
320.93	0.598	320.93	0.786	320.93	0.847	320.93	0.793
413.79	/	413.79	0.65	413.79	0.851	413.79	0.806
533.53	/	533.53	/	533.53	0.783	533.53	0.9
687.92	/	687.92	/	687.92	0.644	687.92	0.949

Appendix 3: Circularity Distribution

MCC Cp-102		MCC Cp-203		MCC Cp-305		PMMA	
Size $[\mu m]$	%	Size $[\mu m]$	%	Size $[\mu m]$	%	Size $[\mu m]$	%
4.39	0.886	4.39	0.886	4.39	0.886	4.39	0.886
6.23	/	6.23	/	6.23	/	6.23	/
7.09	0.899	7.09	0.899	7.09	0.899	7.09	0.899
9.14	0.848	9.14	0.854	9.14	0.853	9.14	0.863
11.79	0.815	11.79	0.805	11.79	0.813	11.79	0.816
15.2	0.79	15.2	0.814	15.2	0.818	15.2	0.827
19.6	0.773	19.6	0.782	15.2	0.818	15.2	0.827
25.27	0.758	25.27	0.791	19.6	0.764	19.6	0.729
32.58	0.741	32.58	0.745	25.27	0.756	25.27	0.709
42.01	0.743	42.01	0.771	32.58	0.787	32.58	0.736
54.17	0.73	54.17	0.721	42.01	0.744	42.01	0.787
69.85	0.726	69.85	0.594	54.17	0.697	54.17	0.873
90.06	0.743	90.06	0.81	54.17	0.697	54.17	0.873
116.12	0.92	116.12	/	69.85	/	69.85	0.885
149.72	0.92	149.72	0.91	90.06	/	90.06	0.898
193.04	0.914	193.04	0.915	116.12	/	116.12	0.895
248.9	0.894	248.9	0.917	149.72	/	149.72	0.903
320.93	0.755	320.93	0.902	193.04	/	193.04	0.903
193.04	/	413.79	0.809	193.04	/	193.04	0.903
248.9	/	248.9	/	248.9	0.926	248.9	0.891
320.93	/	320.93	/	320.93	0.919	320.93	0.867
413.79	/	413.79	/	413.79	0.918	413.79	0.862
533.53	/	533.53	/	533.53	0.904	533.53	0.891
687.92	/	687.92	/	687.92	0.798	687.92	0.902

Appendix 4: Mixing parameters and results

AUPT tests results for the mixing quality assessment: MCC Cp-102 + 500 cSt silicone oil

	Consolidation stress [kPa]	Pre-consolidation stress [kPa]	Failure stress [kPa]	Failure speed [mm/s]	Sample compression [mm]	Strain rate [1/s]	Poured bulk density [g/m^3]	Final density [g/m^3]
Upper layer	20	5	0.79	5	13.2	0.1144	0.79	0.93
	20	5	0.83	5	13.9	0.1163	0.73	0.92
	20	5	0.84	5	14.2	0.1171	0.71	0.86
Lower layer	20	5	0.81	5	12.9	0.1136	0.70	0.86
	20	5	0.78	5	13.8	0.1160	0.74	0.84
	20	5	0.82	5	14.0	0.1165	0.72	0.84

AUPT tests results for the mixing quality assessment: MCC Cp-102 + 30000 cSt silicone oil

	Consolidation stress [kPa]	Pre-consolidation stress [kPa]	Failure stress [kPa]	Failure speed [mm/s]	Sample compression [mm]	Strain rate [1/s]	Poured bulk density [g/m^3]	Final density [g/m^3]
Upper layer	20	5	1.26	5	13.6	0.1178	0.79	0.89
	20	5	1.41	5	14.2	0.1195	0.75	0.91
	20	5	1.36	5	13.9	0.1186	0.73	0.88
Lower layer	20	5	1.32	5	13.2	0.1167	0.78	0.93
	20	5	1.40	5	14.1	0.1192	0.76	0.97
	20	5	1.38	5	13.8	0.1183	0.77	0.89

Appendix 5: AUPT results

AUPT tests results for MCC Cp-102+500 cSt silicone oil.

Consolidation stress [kPa]	Failure stress [kPa]	Failure speed [mm/s]	Sample compression [mm]	Strain rate [1/s]	Poured bulk density [g/m^3]	Final density [g/m^3]	Ca	Str*
20	0.63	0.1	11.3	0.0022	0.71	0.86	8.08E-06	4.60
20	0.82	4.9	11.3	0.1095	0.7	0.86	3.96E-04	5.99
20	0.65	0.08	18.3	0.0014	0.63	0.84	5.10E-06	4.75
20	0.6	0.03	20.3	0.0005	0.62	0.84	1.98E-06	4.38
20	0.64	0.05	17.2	0.0009	0.64	0.86	3.13E-06	4.68
20	0.64	0.2	24.1	0.0039	0.57	0.83	1.42E-05	4.68
20	0.68	0.2	9.0	0.0043	0.74	0.86	1.54E-05	4.97
20	0.71	1.6	8.1	0.0334	0.76	0.87	1.21E-04	5.19
20	0.68	3.5	9.9	0.0758	0.72	0.86	2.74E-04	4.97
20	0.8	2.5	13.5	0.0588	0.66	0.88	2.13E-04	5.85
20	0.79	4.2	10.3	0.0918	0.72	0.86	3.32E-04	5.77
20	0.69	4.7	11.0	0.1043	0.7	0.86	3.77E-04	5.04
20	0.68	3.8	11.7	0.0857	0.69	0.85	3.10E-04	4.97
20	0.69	2.8	11.8	0.0633	0.69	0.86	2.29E-04	5.04
20	0.69	2	9.3	0.0428	0.72	0.86	1.55E-04	5.04
20	0.62	1.8	11.4	0.0403	0.69	0.87	1.46E-04	4.53
20	0.63	1.4	9.9	0.0303	0.7	0.86	1.10E-04	4.60
20	0.62	1	10.2	0.0218	0.7	0.86	7.89E-05	4.53
20	0.7	0.8	12.0	0.0182	0.69	0.86	6.57E-05	5.12
40	0.79	2.5	12	0.0568	0.68	0.87	2.05E-04	5.77
40	0.81	2.5	11.7	0.0564	0.71	0.89	2.04E-04	5.92
40	0.88	4.9	10.7	0.1080	0.75	0.91	3.91E-04	6.43
40	0.88	1.6	12.9	0.0371	0.69	0.89	1.34E-04	6.43
40	0.89	3.5	10.9	0.0775	0.72	0.9	2.80E-04	6.50
40	0.81	0.2	17.4	0.0035	0.65	0.88	1.26E-05	5.92
40	0.81	0.2	17.4	0.0035	0.65	0.88	1.26E-05	5.92
40	0.69	0.05	19.7	0.0009	0.64	0.05	3.27E-06	5.04
40	0.77	0.03	22.9	0.0006	0.61	0.87	2.08E-06	5.63
40	0.8	0.08	19.1	0.0014	0.62	0.85	5.18E-06	5.85
40	0.85	4.2	13	0.0976	0.69	0.89	3.53E-04	6.21
40	0.78	4.7	12.2	0.1072	0.7	0.89	3.88E-04	5.70
40	0.79	3.8	12.6	0.0875	0.69	0.89	3.16E-04	5.77
40	0.81	2.8	12.8	0.0647	0.69	0.89	2.34E-04	5.92
40	0.86	2	13.2	0.0467	0.68	0.89	1.69E-04	6.28
40	0.85	0.01	11.3	0.0002	0.72	0.89	8.08E-07	6.21
40	0.79	1.8	12.3	0.0411	0.69	0.89	1.49E-04	5.77
40	0.75	1.4	12.3	0.0320	0.7	0.88	1.16E-04	5.48

40	0.8	1	11.6	0.0225	0.7	0.88	8.14E-05	5.85
40	0.82	0.8	12.3	0.0183	0.7	0.9	6.61E-05	5.99
40	0.87	0.1	12.7	0.0023	0.68	0.89	8.34E-06	6.36
60	1.02	0.2	12.5	0.0046	0.71	0.92	1.66E-05	7.45
60	0.98	0.01	19.9	0.0002	0.63	0.89	6.56E-07	7.16
60	0.92	0.08	18.8	0.0014	0.64	0.88	5.15E-06	6.72
60	0.94	0.5	19.8	0.0091	0.63	0.88	3.28E-05	6.87
60	0.92	2	19.5	0.0360	0.64	0.89	1.30E-04	6.72
60	0.99	4.9	21.4	0.0914	0.64	0.9	3.31E-04	7.23
60	1.02	0.2	12.5	0.0046	0.71	0.92	1.66E-05	7.45
80	0.98	0.08	19.7	0.0014	0.64	0.9	5.23E-06	7.16
80	1.01	0.5	20.8	0.0092	0.63	0.91	3.34E-05	7.38
80	0.99	2	20	0.0364	0.64	0.9	1.32E-04	7.23
80	0.97	0.01	19.5	0.0002	0.63	0.9	6.52E-07	7.09
80	1.02	4.9	22.6	0.0935	0.62	0.9	3.38E-04	7.45
100	1.11	0.8	12	0.0182	0.73	0.93	6.57E-05	8.11
100	1.24	1.6	11.7	0.0361	0.74	0.92	1.31E-04	9.06
100	1.06	4.2	9.9	0.0910	0.76	0.91	3.29E-04	7.75
100	1.15	0.2	22	0.0038	0.54	0.91	1.37E-05	8.40
100	1.11	0.05	23.8	0.0010	0.62	0.91	3.53E-06	8.11
100	1.16	0.03	23.4	0.0006	0.65	0.91	2.10E-06	8.48
100	1.18	0.08	20.8	0.0015	0.65	0.91	5.34E-06	8.62
100	1.1	0.1	14	0.0024	0.69	0.92	8.60E-06	8.04
100	1.1	0.2	13.9	0.0047	0.69	0.92	1.72E-05	8.04
100	1.08	2.5	13.7	0.0590	0.7	0.92	2.14E-04	7.89
100	1.13	4.9	15.4	0.1205	0.67	0.92	4.36E-04	8.26
100	1.16	3.8	13.1	0.0885	0.71	0.92	3.20E-04	8.48
100	1.09	2.8	12.1	0.0637	0.73	0.93	2.30E-04	7.97
100	1.18	0.01	10.9	0.0002	0.75	0.92	8.01E-07	8.62
100	1.2	1.8	14.6	0.0434	0.68	0.91	1.57E-04	8.77
100	1.24	1.2	12.3	0.0274	0.72	0.92	9.92E-05	9.06
100	1.18	1	12.5	0.0230	0.72	0.92	8.31E-05	8.62
100	1.12	3.5	15.2	0.0857	0.7	0.92	3.10E-04	8.18

AUPT tests results for MCC Cp-102+30000 cSt silicone oil.

Consolidation stress [kPa]	Failure stress [kPa]	Failure speed [mm/s]	Sample compression [mm]	Strain rate [1/s]	Poured bulk density [g/m^3]	Final density [g/m^3]	Ca	Str*
20	0.31	0.2	11.3	0.0031	0.79	0.93	6.81E-04	2.27
20	1.26	4.9	14.9	0.0815	0.73	0.92	1.77E-02	9.21
20	0.88	0.5	12.2	0.0080	0.78	0.92	1.73E-03	6.43
20	0.88	0.05	13.2	0.0008	0.78	0.94	1.76E-04	6.43
20	0.91	0.1	11.9	0.0016	0.78	0.92	3.44E-04	6.65
20	0.91	2	15	0.0333	0.72	0.91	7.23E-03	6.65
20	0.89	1	13.8	0.0163	0.72	0.91	3.55E-03	6.50
20	1.41	4.9	20.1	0.0893	0.69	0.94	1.94E-02	10.30
20	1.36	4.9	16.1	0.0832	0.72	0.94	1.81E-02	9.94
20	1.32	4.9	15.7	0.0826	0.74	0.94	1.79E-02	9.65
20	0.95	2	15.3	0.0335	0.74	0.91	7.27E-03	6.94
40	1.31	4.9	15.1	0.0818	0.71	0.91	1.78E-02	9.57
40	0.85	0.1	18.5	0.0018	0.71	0.94	3.84E-04	6.21
40	0.84	0.05	18.1	0.0009	0.75	0.94	1.91E-04	6.14
40	0.89	0.5	17.1	0.0086	0.73	0.93	1.87E-03	6.50
40	1.01	2	14.9	0.0333	0.7	0.92	7.22E-03	7.38
40	0.75	1	11.9	0.0158	0.8	0.94	3.44E-03	5.48
40	1.28	3	16.3	0.0511	0.73	0.94	1.11E-02	9.35
60	1.35	4.9	3.4	0.0684	0.91	0.95	1.49E-02	9.87
60	1.05	0.5	17.8	0.0087	0.73	0.94	1.90E-03	7.67
60	0.97	0.05	17.5	0.0009	0.73	0.96	1.89E-04	7.09
60	0.99	0.1	17	0.0017	0.74	0.94	3.74E-04	7.23
60	1.08	2	15.8	0.0338	0.74	0.96	7.33E-03	7.89
60	1.35	4.9	15.6	0.0825	0.76	0.96	1.79E-02	9.87
60	1.31	3	16.9	0.0516	0.71	0.93	1.12E-02	9.57
80	1.52	4.9	11.5	0.0772	0.8	0.94	1.67E-02	11.11
80	1.03	0.05	11.8	0.0008	0.79	0.92	1.72E-04	7.53
80	1.05	0.1	17	0.0017	0.74	0.94	3.74E-04	7.67
80	1.15	0.5	13.9	0.0082	0.77	0.94	1.78E-03	8.40
80	1.32	2	15.5	0.0336	0.75	0.96	7.30E-03	9.65
80	1.64	4.9	17.2	0.0848	0.73	0.96	1.84E-02	11.98
80	1.27	3	18.9	0.0535	0.7	0.94	1.16E-02	9.28
100	1.1	0.5	18.8	0.0089	0.7	0.94	1.93E-03	8.04
100	1.08	0.05	18.2	0.0009	0.73	0.96	1.91E-04	7.89
100	1.15	0.1	17.3	0.0017	0.74	0.95	3.76E-04	8.40
100	1.34	4.9	13.8	0.0801	0.75	0.94	1.74E-02	9.79
100	1.35	4.9	5.5	0.0705	0.88	0.95	1.53E-02	9.87
100	1.39	2	25.7	0.0406	0.63	0.95	8.80E-03	10.16
100	1.66	4.9	16.3	0.0835	0.73	0.96	1.81E-02	12.13

100	1.7	4.9	18.5	0.0867	0.71	0.96	1.88E-02	12.42
100	1.3	3	17.8	0.0524	0.72	0.94	1.14E-02	9.50
100	1.33	3	13.1	0.0485	0.78	0.93	1.05E-02	9.72

AUPT tests results for MCC Cp-203+500 cSt silicone oil.

Consolidation stress [kPa]	Failure stress [kPa]	Failure speed [mm/s]	Sample compression [mm]	Strain rate [1/s]	Poured bulk density [g/m^3]	Final density [g/m^3]	Ca	Str*
20	0.50	0.05	11.3	0.0011	0.71	0.86	5.56E-06	5.03
20	0.52	1	11.3	0.0223	0.70	0.86	1.11E-04	5.23
20	0.52	2	18.3	0.0353	0.63	0.84	1.76E-04	5.23
20	0.54	4.9	20.3	0.0896	0.62	0.84	4.46E-04	5.43
40	0.60	0.05	12.0	0.0011	0.68	0.87	5.65E-06	6.04
40	0.60	1	11.6	0.0225	0.70	0.88	1.12E-04	6.04
40	0.61	2	12.3	0.0457	0.70	0.90	2.28E-04	6.14
40	0.66	4.9	12.7	0.1130	0.68	0.89	5.63E-04	6.64
60	0.73	0.05	18.8	0.0009	0.64	0.88	4.43E-06	7.34
60	0.67	1	19.8	0.0181	0.63	0.88	9.02E-05	6.74
60	0.72	2	19.5	0.0360	0.64	0.89	1.79E-04	7.24
60	0.82	4.9	21.4	0.0914	0.64	0.90	4.55E-04	8.25
80	0.81	0.05	20.0	0.0009	0.64	0.90	4.53E-06	8.15
80	0.77	1	19.5	0.0180	0.63	0.90	8.97E-05	7.75
80	0.77	2	19.5	0.0360	0.63	0.90	1.79E-04	7.75
80	0.83	4.9	22.6	0.0935	0.62	0.90	4.66E-04	8.35
100	0.86	0.05	12.0	0.0011	0.73	0.93	5.65E-06	8.65
100	0.94	1	11.7	0.0225	0.74	0.92	1.12E-04	9.46
100	0.87	2	9.9	0.0433	0.76	0.91	2.16E-04	8.75
100	0.88	4.9	22.0	0.0925	0.54	0.91	4.60E-04	8.85

AUPT tests results for MCC Cp-203+30000 cSt silicone oil.

Consolidation stress [kPa]	Failure stress [kPa]	Failure speed [mm/s]	Sample compression [mm]	Strain rate [1/s]	Poured bulk density [g/m^3]	Final density [g/m^3]	Ca	Str*
20	0.55	0.05	11.3	0.0008	0.79	0.93	2.35E-04	5.53
20	0.65	1	14.9	0.0166	0.73	0.92	4.97E-03	6.54
20	0.72	2	12.2	0.0318	0.78	0.92	9.52E-03	7.24
20	0.89	4.9	15.3	0.0821	0.74	0.91	2.45E-02	8.95
40	0.61	0.05	15.1	0.0008	0.71	0.91	2.49E-04	6.14
40	0.74	1	18.5	0.0177	0.71	0.94	5.29E-03	7.45

40	0.82	2	17.1	0.0345	0.73	0.93	1.03E-02	8.25
40	0.96	4.9	14.9	0.0815	0.70	0.92	2.44E-02	9.66
60	0.73	0.05	17.0	0.0009	0.74	0.94	2.58E-04	7.34
60	0.90	1	15.8	0.0169	0.74	0.96	5.05E-03	9.06
60	0.90	2	15.6	0.0337	0.76	0.96	1.01E-02	9.06
60	1.06	4.9	16.9	0.0843	0.71	0.93	2.52E-02	10.67
80	0.79	0.05	13.9	0.0008	0.77	0.94	2.45E-04	7.95
80	0.90	1	15.5	0.0168	0.75	0.96	5.02E-03	9.06
80	0.99	2	17.2	0.0346	0.73	0.96	1.03E-02	9.96
80	1.13	4.9	18.9	0.0873	0.70	0.94	2.61E-02	11.37
100	0.87	0.05	16.3	0.0009	0.73	0.96	2.55E-04	8.75
100	1.02	1	18.5	0.0177	0.71	0.96	5.29E-03	10.26
100	1.07	2	17.8	0.0350	0.72	0.94	1.04E-02	10.77
100	1.57	4.9	13.1	0.0792	0.78	0.93	2.37E-02	15.80

AUPT tests results for MCC Cp-305+500 cSt silicone oil.

Consolidation stress [kPa]	Failure stress [kPa]	Failure speed [mm/s]	Sample compression [mm]	Strain rate [1/s]	Poured bulk density [g/m^3]	Final density [g/m^3]	Ca	Str*
20	0.36	0.05	16.5	0.0009	0.71	0.86	7.02E-06	5.98
20	0.36	1	16.0	0.0169	0.70	0.86	1.39E-04	5.98
20	0.36	2	18.3	0.0353	0.63	0.84	2.90E-04	5.98
20	0.42	4.9	20.3	0.0896	0.62	0.84	7.36E-04	6.97
40	0.44	0.05	16.5	0.0009	0.68	0.87	7.02E-06	7.31
40	0.42	1	14.0	0.0164	0.70	0.88	1.35E-04	6.97
40	0.46	2	15.3	0.0335	0.70	0.90	2.75E-04	7.64
40	0.47	4.9	18.1	0.0861	0.68	0.89	7.08E-04	7.80
60	0.50	0.05	18.8	0.0009	0.64	0.88	7.31E-06	8.30
60	0.52	1	19.8	0.0181	0.63	0.88	1.49E-04	8.63
60	0.54	2	19.5	0.0360	0.64	0.89	2.96E-04	8.97
60	0.62	4.9	21.4	0.0914	0.64	0.90	7.51E-04	10.29
80	0.59	0.05	20.0	0.0009	0.64	0.90	7.47E-06	9.80
80	0.62	1	19.5	0.0180	0.63	0.90	1.48E-04	10.29
80	0.58	2	19.5	0.0360	0.63	0.90	2.96E-04	9.63
80	0.63	4.9	22.6	0.0935	0.62	0.90	7.69E-04	10.46
100	0.70	0.05	19.2	0.0009	0.73	0.93	7.36E-06	11.62
100	0.76	1	18.6	0.0177	0.74	0.92	1.46E-04	12.62
100	0.70	2	21.9	0.0377	0.76	0.91	3.10E-04	11.62
100	0.75	4.9	22.0	0.0925	0.54	0.91	7.60E-04	12.45

AUPT tests results for MCC Cp-305+30000 cSt silicone oil.

Consolidation stress [kPa]	Failure stress [kPa]	Failure speed [mm/s]	Sample compression [mm]	Strain rate [1/s]	Poured bulk density [g/m^3]	Final density [g/m^3]	Ca	Str*
20	0.38	0.05	14.2	0.0008	0.79	0.93	4.06E-04	6.31
20	0.49	1	14.9	0.0166	0.73	0.92	8.20E-03	8.14
20	0.53	2	15.9	0.0338	0.78	0.92	1.67E-02	8.80
20	0.68	4.9	16.5	0.0838	0.74	0.91	4.13E-02	11.29
40	0.46	0.05	15.1	0.0008	0.71	0.91	4.12E-04	7.64
40	0.60	1	18.5	0.0177	0.71	0.94	8.73E-03	9.96
40	0.62	2	17.1	0.0345	0.73	0.93	1.70E-02	10.29
40	0.78	4.9	14.9	0.0815	0.70	0.92	4.02E-02	12.95
60	0.51	0.05	17.0	0.0009	0.74	0.94	4.25E-04	8.47
60	0.62	1	15.8	0.0169	0.74	0.96	8.33E-03	10.29
60	0.72	2	15.6	0.0337	0.76	0.96	1.66E-02	11.95
60	0.87	4.9	16.9	0.0843	0.71	0.93	4.16E-02	14.44
80	0.66	0.05	13.9	0.0008	0.77	0.94	4.04E-04	10.96
80	0.71	1	15.5	0.0168	0.75	0.96	8.29E-03	11.79
80	0.83	2	17.2	0.0346	0.73	0.96	1.71E-02	13.78
80	0.89	4.9	18.9	0.0873	0.70	0.94	4.31E-02	14.78
100	0.69	0.05	16.3	0.0009	0.73	0.96	4.20E-04	11.46
100	0.82	1	18.5	0.0177	0.71	0.96	8.73E-03	13.61
100	0.90	2	17.8	0.0350	0.72	0.94	1.72E-02	14.94
100	1.02	4.9	13.1	0.0792	0.78	0.93	3.90E-02	16.93

AUPT tests results for PMMA+500 cSt silicone oil.

Consolidation stress [kPa]	Failure stress [kPa]	Failure speed [mm/s]	Sample compression [mm]	Strain rate [1/s]	Poured bulk density [g/m^3]	Final density [g/m^3]	Ca	Str*
20	0.35	4.9	15.5	0.0824	0.55	0.71	3.81E-04	3.27
20	0.34	2	16.3	0.0341	0.56	0.71	1.58E-04	3.18
20	0.35	0.5	17.2	0.0087	0.55	0.71	4.00E-05	3.27
20	0.33	0.05	15.1	0.0008	0.55	0.68	3.86E-06	3.08
20	0.35	1	14.8	0.0166	0.53	0.72	7.68E-05	3.27
20	0.34	0.08	14.9	0.0013	0.55	0.68	6.16E-06	3.18
40	0.42	4.9	15.7	0.0826	0.55	0.71	3.82E-04	3.93
40	0.37	2	11.0	0.0313	0.61	0.71	1.45E-04	3.46
40	0.38	4.9	14.0	0.0803	0.58	0.71	3.72E-04	3.55
40	0.35	0.5	11.8	0.0079	0.60	0.71	3.66E-05	3.27
40	0.4	0.08	15.9	0.0014	0.56	0.72	6.26E-06	3.74

60	0.43	4.9	15.7	0.0826	0.55	0.72	3.82E-04	4.02
60	0.37	4.9	15.4	0.0822	0.57	0.71	3.80E-04	3.46
60	0.38	2	13.7	0.0326	0.59	0.72	1.51E-04	3.55
60	0.36	0.5	10.3	0.0077	0.62	0.72	3.58E-05	3.36
60	0.36	0.08	15.7	0.0013	0.57	0.72	6.24E-06	3.36
60	0.34	0.01	9.7	0.0002	0.63	0.72	7.08E-07	3.18
80	0.44	4.9	17.0	0.0845	0.55	0.72	3.91E-04	4.11
80	0.3	0.08	13.7	0.0013	0.59	0.72	6.04E-06	2.80
80	0.36	0.5	14.5	0.0083	0.59	0.72	3.82E-05	3.36
80	0.4	2	13.0	0.0323	0.61	0.73	1.49E-04	3.74
80	0.34	4.9	11.9	0.0777	0.61	0.73	3.59E-04	3.18
100	0.44	4.9	16.5	0.0838	0.56	0.73	3.88E-04	4.11
100	0.36	0.08	12.4	0.0013	0.61	0.73	5.91E-06	3.36
100	0.35	0.5	9.8	0.0077	0.64	0.73	3.55E-05	3.27
100	0.38	2	9.7	0.0306	0.64	0.73	1.42E-04	3.55
100	0.38	2	11.7	0.0316	0.62	0.73	1.46E-04	3.55

AUPT tests results for PMMA+30000 cSt silicone oil.

Consolidation stress [kPa]	Failure stress [kPa]	Failure speed [mm/s]	Sample compression [mm]	Strain rate [1/s]	Poured bulk density [g/m^3]	Final density [g/m^3]	Ca	Str*
20	0.32	0.2	12.7	0.0032	0.61	0.73	8.91E-04	2.99
20	0.54	0.5	11.9	0.0079	0.64	0.75	2.20E-03	5.05
20	0.64	1	12.2	0.0159	0.63	0.74	4.42E-03	5.98
20	0.49	0.05	12.5	0.0008	0.63	0.75	2.22E-04	4.58
20	1.03	4	14.1	0.0657	0.62	0.76	1.82E-02	9.63
20	0.43	0.2	12.9	0.0032	0.63	0.76	8.94E-04	4.02
20	0.9	4.9	13.4	0.0795	0.62	0.76	2.21E-02	8.41
20	0.7	2	12.4	0.0319	0.63	0.76	8.87E-03	6.54
20	0.5	0.5	13.4	0.0081	0.62	0.76	2.25E-03	4.67
40	0.59	0.5	18.0	0.0088	0.58	0.77	2.43E-03	5.51
40	0.55	0.05	17.8	0.0009	0.59	0.79	2.43E-04	5.14
40	1.25	4	18.0	0.0702	0.58	0.76	1.95E-02	11.68
40	0.74	1	17.4	0.0174	0.59	0.76	4.82E-03	6.92
40	0.59	0.5	14.1	0.0082	0.61	0.75	2.28E-03	5.51
40	0.84	2	17.1	0.0345	0.59	0.77	9.59E-03	7.85
40	1.15	4.9	13.5	0.0797	0.61	0.76	2.21E-02	10.75
60	1.14	4.9	16.3	0.0835	0.60	0.77	2.32E-02	10.65
60	0.57	0.05	16.8	0.0009	0.65	0.79	2.38E-04	5.33
60	0.58	0.5	14.0	0.0082	0.62	0.76	2.28E-03	5.42
60	0.72	1	16.4	0.0171	0.60	0.76	4.74E-03	6.73

60	1.23	4	14.5	0.0661	0.62	0.77	1.84E-02	11.50
60	0.87	2	16.8	0.0344	0.60	0.77	9.54E-03	8.13
60	0.63	0.5	15.7	0.0084	0.61	0.77	2.34E-03	5.89
80	0.67	0.5	16.8	0.0086	0.60	0.78	2.38E-03	6.26
80	1.25	4	14.5	0.0661	0.63	0.77	1.84E-02	11.68
80	0.58	0.05	14.1	0.0008	0.65	0.79	2.28E-04	5.42
80	0.8	1	18.0	0.0175	0.59	0.77	4.87E-03	7.48
80	0.6	0.5	15.4	0.0084	0.61	0.76	2.33E-03	5.61
80	0.92	2	15.2	0.0334	0.62	0.78	9.28E-03	8.60
80	1.35	4.9	22.7	0.0937	0.54	0.77	2.60E-02	12.62
100	1.69	4.9	17.8	0.0857	0.58	0.79	2.38E-02	15.80
100	0.52	0.05	17.9	0.0009	0.60	0.78	2.43E-04	4.86
100	0.64	0.5	18.6	0.0089	0.58	0.77	2.46E-03	5.98
100	0.86	1	18.6	0.0177	0.58	0.77	4.92E-03	8.04
100	1.35	4	17.9	0.0701	0.60	0.77	1.94E-02	12.62
100	1.04	2	17.0	0.0345	0.61	0.78	9.57E-03	9.72
100	0.75	0.5	16.0	0.0085	0.62	0.77	2.35E-03	7.01

Appendix 6: Instron results

Instron tests results for MCC Cp-102+500 cSt silicone oil.

Consol. stress [MPa]	Failure load [kN]	Failure speed [mm/s]	Sample compr. [mm]	Strain rate [1/s]	Engineering tensile stress [kPa]	Fracture energy [N*m]	Cad [-]	Str*d [-]	Thoug-ness [-]
75	0.0033	0.005	0.25	3.92E-04	10.96	50	1.42E-06	80.1	0.365
75	0.0036	0.01	0.31	7.88E-04	12.24	137	2.85E-06	89.5	0.998
75	0.0034	0.05	0.21	3.91E-03	11.48	97	1.41E-05	83.9	0.707
75	0.0038	0.3	0.30	2.36E-02	12.88	140	8.54E-05	94.1	1.024
75	0.0038	0.5	0.20	3.91E-02	13.39	122	1.41E-04	97.8	0.889
75	0.0035	0.8	0.18	6.24E-02	12.47	137	2.26E-04	91.1	1.000
75	0.0041	1	0.38	7.92E-02	14.92	207	2.87E-04	109.0	1.514
75	0.0028	0.005	0.20	3.91E-04	9.92	/	1.41E-06	72.5	/
75	0.0028	0.01	0.45	7.97E-04	11.62	/	2.88E-06	84.9	/
75	0.0035	0.05	0.32	3.94E-03	14.31	/	1.43E-05	104.6	/
75	0.0038	0.1	0.30	7.87E-03	16.07	/	2.85E-05	117.4	/
75	0.0033	0.5	0.20	3.91E-02	13.67	/	1.41E-04	99.9	/
75	0.0038	1	0.65	8.13E-02	17.59	/	2.94E-04	128.5	/
75	0.0037	1	0.40	7.94E-02	17.56	/	2.87E-04	128.3	/
75	0.0033	0.3	0.10	2.33E-02	11.38	50	8.41E-05	83.2	0.365
150	0.0035	0.01	0.38	7.92E-04	13.97	154	2.87E-06	102.1	1.123
150	0.0058	0.1	0.20	7.81E-03	21.20	221	2.83E-05	154.9	1.611
150	0.0041	0.005	0.19	3.90E-04	15.61	111	1.41E-06	114.1	0.808
150	0.0042	0.05	0.18	3.90E-03	16.68	149	1.41E-05	121.9	1.091
150	0.0060	0.5	0.35	3.95E-02	21.61	290	1.43E-04	157.9	2.121
150	0.0064	0.8	0.22	6.26E-02	23.76	333	2.26E-04	173.6	2.432
150	0.0056	1	0.15	7.78E-02	20.70	128	2.82E-04	151.3	0.938
225	0.0070	0.005	0.20	3.91E-04	28.73	137	1.41E-06	209.9	1.000
225	0.0061	0.05	0.19	3.90E-03	22.41	120	1.41E-05	163.8	0.878
225	0.0054	0.1	0.30	7.87E-03	21.78	152	2.85E-05	159.2	1.113
225	0.0081	0.3	0.37	2.38E-02	32.54	170	8.59E-05	237.8	1.243
225	0.0079	0.5	0.20	3.91E-02	29.37	286	1.41E-04	214.6	2.093
225	0.0087	0.8	0.30	6.30E-02	33.17	402	2.28E-04	242.4	2.940
225	0.0083	1	0.27	7.86E-02	32.75	396	2.84E-04	239.3	2.896
225	0.0070	0.005	0.20	3.91E-04	28.73	137	1.41E-06	209.9	1.000

Instron tests results for MCC Cp-102+30000 cSt silicone oil.

Consol. stress [MPa]	Failure load [kN]	Failure speed [mm/s]	Sample compr. [mm]	Strain rate [1/s]	Engineering tensile stress [kPa]	Fracture energy [N*m]	Cad [-]	Str*d [-]	Thoug-ness [-]
75	0.0022	0.005	0.10	3.88E-04	7.53	19	8.41E-05	55.1	0.140
75	0.0024	0.01	0.19	7.81E-04	7.96	44	1.69E-04	58.2	0.323
75	0.0026	0.05	0.16	3.89E-03	9.19	49	8.45E-04	67.2	0.360
75	0.0034	0.1	0.16	7.79E-03	11.86	33	1.69E-03	86.7	0.239
75	0.0039	0.3	0.24	2.35E-02	13.29	167	5.10E-03	97.1	1.219
75	0.0038	0.5	0.18	3.90E-02	13.11	/	8.46E-03	95.8	/
75	0.0049	0.8	0.48	6.39E-02	15.74	347	1.39E-02	115.0	2.534
75	0.0050	1	0.37	7.92E-02	17.76	244	1.72E-02	129.8	1.785
75	0.0020	0.005	0.20	3.91E-04	7.53	/	8.48E-05	55.1	/
75	0.0033	0.01	0.12	7.76E-04	11.22	/	1.69E-04	82.0	/
75	0.0020	0.05	0.32	3.94E-03	7.13	/	8.56E-04	52.1	/
75	0.0028	0.1	0.22	7.82E-03	9.64	/	1.70E-03	70.4	/
75	0.0032	0.3	0.21	2.35E-02	10.30	/	5.09E-03	75.3	/
75	0.0037	0.5	0.35	3.95E-02	12.81	/	8.58E-03	93.6	/
75	0.0068	0.8	0.45	6.37E-02	22.35	/	1.38E-02	163.3	/
75	0.0072	1	0.32	7.89E-02	23.63	19	1.71E-02	172.7	0.140
150	0.0022	0.005	0.10	3.88E-04	8.34	30	8.41E-05	61.0	0.216
150	0.0046	0.05	0.32	3.94E-03	17.40	138	8.56E-04	127.1	1.006
150	0.0070	0.3	0.30	2.36E-02	26.38	279	5.13E-03	192.8	2.042
150	0.0050	0.5	0.35	3.95E-02	18.34	202	8.58E-03	134.0	1.476
150	0.0105	0.8	0.30	6.30E-02	39.16	511	1.37E-02	286.1	3.734
150	0.0082	1	0.27	7.86E-02	30.31	513	1.70E-02	221.5	3.748
150	0.0035	0.005	0.22	3.91E-04	12.91	/	8.49E-05	94.3	/
150	0.0036	0.01	0.04	7.72E-04	13.05	/	1.67E-04	95.4	/
150	0.0045	0.05	0.18	3.90E-03	17.31	/	8.46E-04	126.5	/
150	0.0088	0.1	0.21	7.82E-03	31.18	/	1.70E-03	227.9	/
150	0.0102	0.3	0.23	2.35E-02	40.12	/	5.10E-03	293.2	/
150	0.0100	0.5	0.31	3.94E-02	38.23	/	8.55E-03	279.4	/
150	0.0100	0.8	0.51	6.41E-02	36.55	/	1.39E-02	267.1	/
150	0.0102	1	0.19	7.81E-02	38.81	30	1.69E-02	283.6	0.216
225	0.0041	0.005	0.20	3.91E-04	15.76	94	8.48E-05	115.2	0.686
225	0.0046	0.05	0.30	3.94E-03	16.97	167	8.54E-04	124.0	1.217
225	0.0058	0.1	0.25	7.84E-03	22.19	160	1.70E-03	162.2	1.169
225	0.0085	0.3	0.33	2.37E-02	30.91	312	5.14E-03	225.9	2.282
225	0.0100	0.5	0.34	3.95E-02	35.25	375	8.57E-03	257.6	2.743
225	0.0135	0.8	0.30	6.30E-02	51.45	550	1.37E-02	376.0	4.019
225	0.0156	1	0.27	7.86E-02	55.30	710	1.70E-02	404.1	5.188

Instron tests results for MCC Cp-305+500 cSt silicone oil.

Consol. stress [MPa]	Failure load [kN]	Failure speed [mm/s]	Sample compr. [mm]	Strain rate [1/s]	Engineering tensile stress [kPa]	Fracture energy [N*m]	Cad [-]	Str*d [-]	Thoug-ness [-]
75	0.0015	0.005	0.30	3.94E-04	5.03	42	3.24E-06	83.6	0.698
75	0.0016	0.05	0.22	3.91E-06	5.48	98	3.22E-08	91.0	1.628
75	0.0017	0.3	0.28	2.36E-05	5.78	143	1.94E-07	96.1	2.376
75	0.0015	0.8	0.20	6.25E-05	5.28	133	5.14E-07	87.8	2.210
75	0.0021	1	0.35	7.91E-05	7.45	221	6.50E-07	123.8	3.672
150	0.0019	0.005	0.22	3.91E-07	7.10	130	3.22E-09	118.0	2.160
150	0.0018	0.05	0.17	3.90E-06	6.89	155	3.21E-08	114.4	2.575
150	0.0027	0.3	0.35	2.37E-05	9.94	292	1.95E-07	165.2	4.852
150	0.0026	0.8	0.24	6.27E-05	9.50	380	5.16E-07	157.9	6.314
150	0.0029	1	0.18	7.80E-05	10.84	425	6.42E-07	180.1	7.062
225	0.0031	0.005	0.22	3.92E-07	7.10	142	3.22E-09	208.5	2.359
225	0.0028	0.05	0.20	3.94E-06	7.81	128	3.21E-08	171.3	2.127
225	0.0034	0.3	0.35	2.37E-05	13.16	186	1.95E-07	216.1	3.090
225	0.004	0.8	0.31	6.29E-05	23.52	390	5.18E-07	252.3	6.480
225	0.0041	1	0.30	7.91E-05	23.96	440	6.48E-07	264.8	7.311

Instron tests results for MCC Cp-305+30000 cSt silicone oil.

Consol. stress [MPa]	Failure load [kN]	Failure speed [mm/s]	Sample compr. [mm]	Strain rate [1/s]	Engineering tensile stress [kPa]	Fracture energy [N*m]	Cad [-]	Str*d [-]	Thoug-ness [-]
75	0.001	0.005	0.12	3.88E-07	3.47	32	1.92E-07	57.7	0.532
75	0.0013	0.05	0.18	3.90E-06	4.55	56	1.92E-06	75.6	0.930
75	0.002	0.3	0.26	2.35E-05	6.90	180	1.16E-05	114.6	2.991
75	0.0023	0.8	0.46	6.38E-05	7.46	350	3.15E-05	123.9	5.815
75	0.0022	1	0.35	7.91E-05	7.81	398	3.90E-05	129.7	6.613
150	0.0011	0.005	0.12	3.88E-07	4.14	30	1.92E-07	68.9	0.498
150	0.0018	0.05	0.33	3.95E-06	6.78	140	1.95E-06	112.7	2.326
150	0.0031	0.3	0.31	2.36E-05	11.86	260	1.17E-05	197.1	4.320
150	0.0048	0.8	0.31	6.30E-05	17.54	480	3.11E-05	291.5	7.975
150	0.0044	1	0.30	7.87E-05	16.20	530	3.89E-05	269.2	8.806
225	0.0019	0.005	0.24	3.92E-07	7.10	100	1.93E-07	118.0	1.662
225	0.0022	0.05	0.32	3.94E-06	7.81	175	1.95E-06	129.7	2.908
225	0.0036	0.3	0.34	2.37E-05	13.16	322	1.17E-05	218.6	5.350
225	0.0061	0.8	0.28	6.29E-05	23.52	470	3.10E-05	390.8	7.809
225	0.0068	1	0.36	7.91E-05	23.96	620	3.90E-05	398.1	10.302

Appendix 7: DEM code of the 10:1 sample

Generation phase

```
start 0.02 0.02 0.02 8000 10000 50 log

*glass %particle sizes

dia 0.00018 1
dia 0.00019 2
dia 0.00020 3

* elastic module
ymd 25.0e9 1
ymd 210.0e9 2

* possion ratio
prat 0.25 1
prat 0.30 2

* density
dens 1.5e3 1
dens 7.9e3 2

* friction coefficients
fric 0.05 1
fric 0.30 2
*
* large limit - elastic
yie 7e30 1
yie 7e30 2
*
* 5% b-b & 10% b-w damping
damp 0.05 0.5 1 0 1
damp 0.10 0.5 1 0 0

* gravity acceleration
grav 0.0 0.0 -9.81

drm 20 0.01 0.01 0.001 0.00205 0.014  mat 2 %generates the cylinder

dwa fpl(0.01305 0.00695 0.001 0.01305 0.01305 0.001 0.00695 0.01305 0.001 0.00695 0.00695
0.001) mat 2 %generate the base plane

agg cyl 1 z 0.001 0.012 0.01 0.01 0.004 0.00205 %creates the volume for the generation

* random generation

rge 2000 3 1 1
rge 5200 2 1 1
rge 2000 1 1 1

* time fraction
frac 0.5
pri inf
plo wal bal
sav stg0
stop
```

Deposition phase

```
res stg0

* switch on the animation

anim on 10000

plot wal ball
cyc 20000
cyc 20000
cyc 20000
cyc 20000
cyc 20000
pri inf
vtp wal bal con

*repeated 16 times
save dep05

stop
```

Consolidation phase

```
res DEP05
* switch on the animation
anim on 10000

dwa fpl(0.01305 0.00695 0.0055 0.01305 0.01305 0.0055 0.00695 0.01305 0.0055
0.00695 0.00695 0.0055) mat 2 %create the consolidation wall

plot wal ball

* input liquid binder
liq 0.01 0.03 30 0.3

awa 22 v 0 0 -0.05 %start the consolidation

vtp wal bal con
pri inf str wal
cyc 20000
vtp wal bal con
pri inf str wal
cyc 20000
vtp wal bal con
pri inf str wal
cyc 20000
vtp wal bal con
pri inf str wal
sav comp01
cyc 20000
vtp wal bal con
pri inf str wal
9000
vtp wal bal con
pri inf str wal

save comp03
stop
```

Relaxation phase

```
res COMP03
* switch on the animation
anim on 10000

awa 22 v 0 0 0
plot wal ball


cyc 20000
cyc 20000
cyc 20000
cyc 20000
cyc 20000
pri inf
vtp wal bal con %repeat until satisfying relaxation is achieved
sav rex
```

Failure phase

```
res rex
* switch on the animation
anim on 4000

fra 1
lay 2

* remove container
awa 1 fpl 0 0 0 0 0 0 0 0 0 0 0 0
awa 2 fpl 0 0 0 0 0 0 0 0 0 0 0 0
awa 3 fpl 0 0 0 0 0 0 0 0 0 0 0 0
awa 4 fpl 0 0 0 0 0 0 0 0 0 0 0 0
awa 5 fpl 0 0 0 0 0 0 0 0 0 0 0 0

awa 6 fpl 0 0 0 0 0 0 0 0 0 0 0 0
awa 7 fpl 0 0 0 0 0 0 0 0 0 0 0 0
awa 8 fpl 0 0 0 0 0 0 0 0 0 0 0 0
awa 9 fpl 0 0 0 0 0 0 0 0 0 0 0 0
awa 10 fpl 0 0 0 0 0 0 0 0 0 0 0 0

awa 11 fpl 0 0 0 0 0 0 0 0 0 0 0 0
awa 12 fpl 0 0 0 0 0 0 0 0 0 0 0 0
awa 13 fpl 0 0 0 0 0 0 0 0 0 0 0 0
awa 14 fpl 0 0 0 0 0 0 0 0 0 0 0 0
awa 15 fpl 0 0 0 0 0 0 0 0 0 0 0 0

awa 16 fpl 0 0 0 0 0 0 0 0 0 0 0 0
awa 17 fpl 0 0 0 0 0 0 0 0 0 0 0 0
awa 18 fpl 0 0 0 0 0 0 0 0 0 0 0 0
awa 19 fpl 0 0 0 0 0 0 0 0 0 0 0 0
awa 20 fpl 0 0 0 0 0 0 0 0 0 0 0 0

awal 22 v 0.0 0.0 -0.005 %start the failure compression at 5 mm/s

plot wal ball vel
vtp wal bal con
pri inf str wal

cyc 4000
pri inf str wal
vtp wal bal con %repeat until satisfying deformation is achieved

sav uni10

stop
```

References

[1]. A. Salman, G. Reynolds, H. Tan (2007). Breakage in granulation, in: J. Williams, T. Allen (Eds.), *Handb. Powder Technology, Granulation*, vol. 11, 2007, Elsevier Science, Amsterdam, pp.979-1040.

[2]. J. D. Litster, B. J. Ennis (2003). The Science and Engineering of Granulation Process, Kluwer Academic Publishers, Dordrecht.

[3]. S. M. Iveson, N. W. Page, J. D. Lister (2003). The importance of wet-powder dynamic mechanical properties in understanding granulation. *Powder Technology*, **130**, 97-101.

[4]. R.H. Perry, D.W. Green (2008). Perry's chemical engineers' handbook, "Solis-solid operations and processing", 8th edition, McGraw-Hill, London, pp. 21.1-21.147.

[5]. R.H. Perry, D.W. Green (2008). Perry's chemical engineers' handbook, "Solis-solid operations and processing", 8th edition, McGraw-Hill, London, pp. 20.59.

[6]. K. P. Hapgood, J. D. Litster, R. M. Smith (2004). Nucleation regime map for liquid bound granules, *AIChE Journal,* **49**, 350-361.

[7]. M. Rhodes (2008). Introduction to Particle Technology, 2nd Edition, John Wiley & Sons, Chichester, UK.

[8]. R.M. Smith (2008). Wet granule breakage in high shear mixer granulators, Ph.D. Thesis, Department of Chemical Engineering, The University of Queensland, Brisbane, Australia.

[9]. S. M. Iveson, J. D. Litster, K. Hapgood, B. J. Ennis (2001). Nucleation, growth and breakage phenomena in agitated wet granulation processes: a review, *Powder Technology*, **117**, 3-39.

[10]. J. D. Litster, K. P. Hapgood, J. N. Michaels, A. Sims, M. Roberts, S. K. Kameneni, T. Hsu (2001). Liquid distribution in wet granulation: dimensionless spray flux, *Powder Technology*, **114**, 29-32.

[11]. J. Litster (2016). Design and Processing of Particulate Products, "Wet granulation", 1st edition, Cambridge University Press.

[12]. G. I. Tardos, M.I. Khan, P. R. Mort (1997). Critical parameters and limiting conditions in binder granulation of fine powders, *Powder Technology*, **94**, 245-258.

[13]. S. M. Iveson, P. A. L. Wauters, S. Forrest, J. D. Litster, G. M. H. Meesters, B. Scarlett (2001). Growth regime map for liquid-bound granules: further development and experimental validation, *Powder Technology*, **117**, 83-97.

[14]. S. M. Iveson, J. D. Lister (1998). Growth regime map for liquid-bound granules, *AIChE Journal,* **44**, 1510-1528.

[15]. C. Thornton, Z. Ning (1998). A theoretical model for the stick/bounce behaviour of adhesive, elastic-plastic spheres, *Powder Technology*, **99**, 154-162.

[16]. L. X. Liu, J.D. Litster, S. M. Iveson, B. J. Ennis (2000). Coalescence of deformable granules in wet granulation processes, *AIChE Journal*, **46**, 529-539.

[17]. S. M. Iveson, P. A. L. Wauters, S. Forrest, J. D. Litster, G. M. H. Meesters, B. Scarlett (2001). Growth regime map for liquid-bound granules: further development and experimental validation, *Powder Technology,* **117**, 83-97.

[18]. S.M. Iveson, J.D. Litster (2002). Fundamental studies of granule consolidation, Part 2: quantifying the effects of particle and binder properties, *Powder Technology*, **99**, 243-250.

[19]. S. M. Iveson, J.A. Beathe, N.W. Page (2002). The dynamic strength of partially saturated powder compacts: the effect of liquid properties, *Powder Technology*, **127**, 149-161.

[20]. K. Hotta, K. Takeda, K. Iinoya (1974). The capillary binding force of a liquid bridge, *Powder Technology*, **10**, 231-242.

[21]. G. Lian, C. Thornton, M.J. Adams (1993). A theoretical study of the liquid bridge forces between two spherical bodies, *Journal of Colloid Interface Science*, **161**, 138-147.

[22]. H. Rumpf (1962). The strength of granules and agglomerates, in: W.A. Knepper (Ed.), AIME, Agglomeration, Interscience, pp.379-413, New York.

[23]. K. Van der Dries, H. Vromans (2002). Relationship between inhomogeneity phenomena and granule growth mechanisms in a high-shear mixer, *International Journal of Pharmaceutics*, **247**, 167-77.

[24]. L.X. Liu, R. Smith, J.D. Litster (2009). Wet granule breakage in a breakage only high-shear mixer: effect of formulation properties on breakage behavior, *Powder Technology*, **189**, 158-164.

[25]. H. Shubert, W. Hermann, H. Rumpf (1975). Deformation behaviour of agglomerates under tensile stress, *Powder Technology*, **44**, 227-238.

[26]. D.N. Mazzone, G.I. Tardos, R. Pfeffer (1987). The behaviour of liquid bridges between two relatively moving particles, *Powder Technology*, **51**, 71-83.

[27]. G. Lian, C. Thornton, M.J. Adams (1998). Discrete particle simulation of agglomerate impact coalescence, *Chemical Engineering Science*, **53**, 3381-3391.

[28]. S.M. Iveson, J.D. Litster (1998). Liquid-bound granule impact deformation and coefficient of restitution, *Powder Technology*, **99**, 234-242.

[29]. S.M. Iveson, J.D. Litster, B.J. Ennis (1996). Fundamental studies of granule consolidation, Part 1: effects of binder content and binder viscosity, *Powder Technology*, **88**, 15-20.

[30]. S.M. Iveson, N.W. Page (2005). Dynamic strength of liquid-bound granular materials: the effect of particle size and shape, *Powder Technology*, **152**, 79-89.

[31]. M.L. Sweat, A.S. Parker, S.P. Beaudoin (2016). Compressive behaviour of high-viscosity granular systems: effects of viscosity and strain rate, *Powder Technology*, **302**, 480-487.

[32]. R.M. Smith, J.D. Litster (2012). Examining the failure modes of wet granular materials using dynamic diametrical compression, *Powder Technology*, **224**, 189-195.

[33]. H. Eliasen, T. Schæfer, H.G. Kristensen (1998). Effects of binder rheology on melt agglomeration in a high shear mixer, *International Journal of Pharmaceutics*, **176**, 73-83.

[34]. K. Van Den Dries, O.M. De Vegt, V. Girard, H. Vromans (2003). Granule breakage phenomena in a high shear mixer; influence of process and formulation variables and consequences on granule homogeneity, *Powder Technology*, **133**, 228-236.

[35]. J. Seville, C.-Y. Wu (2016). Particle Technology and Engineering: An Engineer's guide to Particles and Powders: Fundamentals and Computational Approaches, Butterworth-Heinemann.

[36]. W. Yu, B.C. Hancock (2008). Evaluation of dynamic image analysis for characterizing pharmaceutical excipient particles, *International Journal of Pharmaceutic*, **361**, 150-157.

[37]. I. Cavarretta, C. O'Sullivan, E. Ibraim, M. Lings, S. Hamlin, D.M. Wood (2012). Characterization of artificial spherical particles for DEM validation studies, *Particuology*, **10**, 209-220.

[38]. Series of QicPic SYMPATEC® machine, https://www.sympatec.com/, last access: 12/06/19.

[39]. J. Wiącek, M. Molenda (2014). Microstructure and micromechanics of polydisperse granular materials: effect of the shape of particle size distribution, *Powder Technology*, **268**, 237-243.

[40]. P. C. Wright, J. A. Raper (1998). Role of liquid bridge forces in cohesive fluidization, *Chemical Engineering Research and Design,* **76(A6)**, 753-760.

[41]. X. Y. Ong, S. E. Taylor, M. Ramaioli (2017). The effect of interfacial properties and liquid flow on the stability of powder islands, *EPJ Web of Conferences, Powders & Grains 2017*, **140**, 09006.

[42]. C. Mayer-Laigle, C. Gatumel, H. Berthiaux (2015). Mixing dynamics for easy flowing powders in a lab scale Turbula® mixer, *Chemical research and Design*, **95**, 248-261.

[43]. K. P. Hapgood, J. D. Litster, S. R. Biggs, T. Howes (2002). Drop penetration into porous powder beds, *Journal of Colloid and Interface Science*, **253**, 353-366.

[44]. Schematic of uniaxial powder testing, https://www.freemantech.co.uk/_powders/about-the-uniaxial-powder-tester, last access: 14/06/19.

[45]. A. T. Procopio, A. Zavaliangos, J. C. Cunningham (2003). Analysis of the diametrical compression test and the applicability to plastically deforming materials, *Journal of Materials Science*, **38**, 3629-3639.

[46]. H. Hughes, M. M. Leane, M. Tobyn, J. F. Gamble, S. Munoz, P. Musembi (2014). Development of a material sparing bulk density test comparable to a standard USP method for use in early development of API's, *AAPS PharmSciTech,* **16(1)**, 165-170.

[47]. R.S. Hebbar, A.M. Isloor, A.F. Ismail (2017). Contact Angle Measurements. In: *Membrane Characterization* (Elsevier, Ed.), London (UK).

[48]. A. A. Griffith, The phenomena of rupture and flow in solids (1921). Philosophical transactions of the Royal Society of London. Series A **221**: 163-198.

[49]. G. Lian, J. Seville, The capillary bridge between two spheres: New closed-form equation in a two century old problem (2016). *Advances in Colloid and Interface Science* **227**, 53-62.

[50]. C. Thornton, Interparticle sliding in the presence of adhesion (1991), *Journal of Physics D: Applied Physics.* **24**, 1942-1946.

[51]. C. Thornton, Z. Ning, A theoretical model for the stick/bounce behaviour of adhesive, elastic-plastic spheres (1998), *Powder Technology,* **99**, 154-162.